Degradation of Materials under Space Conditions - Extrapolation of Short Term Laboratory Results on Long Term Space Mission Effects

Vom Fachbereich Produktionstechnik

der

UNIVERSITÄT BREMEN

zur Erlangung des Grades
Doktor-Ingenieur
genehmigte

Dissertation

von

Dr. rer. nat. Maciej Sznajder

Gutachter:

Prof. Dr. rer. nat. H.J. Dittus
Fachbereich Produktionstechnik,
Universität Bremen

Prof. Dr. Claus Braxmaier
Zentrum für angewandte Raumfahrttechnologie
und Mikrogravitation,
Universität Bremen

Tag der mündlichen Prüfung: 29. April 2016

Contents

Abstract

Degradation processes of materials under space conditions are subject of this thesis. Metals are commonly used in space technology. Their behavior in the interplanetary medium is still not fully explored subject. Here I present the first approach of that problematic, i.e. aging of metals caused by low energy proton bombardment.

The thesis focuses on one process of the so-called Hydrogen embrittlement i.e. formation of Hydrogen molecular bubbles on metallic surfaces. The process originates from recombination of solar protons with the free electrons of metals into neutral Hydrogen atoms. For solar protons three processes lead the recombination: the Auger-, the resonant-, and the Oppenheimer-Brinkman-Kramers (OBK) -process. A detail mathematical description of these processes is presented.

I have used the DLR's Complex Irradiation Facility (CIF) to study the bubble growth mechanism on metals. The properties of its linear proton accelerator allow to scale the proton flux to that present in the interplanetary medium. However, the bubble formation mechanism will be fully explored when the probes will be carefully examined after simultaneous exposure to the proton flux and electromagnetic radiation, especially to that below 400 nm (UV range). That is a subject of my future studies. Photoionization and photodissociation caused by UV radiation can change the dynamics of bubble growth. High energetic photons can penetrate the thin bubble caps and dissociate the H_2 gas. Therefore, the H atoms can diffuse through the caps out and effectively reduce bubble sizes. That hypothesis will be experimentally examined by use of the so-called Vacuum-UV simulator. I took part in the calibration procedure of the simulator, one of the light sources of the CIF.

I developed a thermodynamic model of bubble growth. The model is based on the assumption that the process is quasistatic. This means that the growth of bubbles proceed much slower than the Hydrogen recombination and that a thermodynamic equilibrium is maintained when H_2 molecules migrate into bubbles. As a result of that process, the irradiated metal is covered with hemispherical bubbles. A quantitative relation between the reflectivity of metal and the bubbles surface density and radii is derived. Additionally, I have proven both theoretically and experimentally that bubble formation leads to surface reflectivity decrease, which leads to changes of the thermo-optical properties of irradiated metal surfaces. I have considered different proton fluxes. The irradiation tests are performed with proton fluxes similar to that in space, $f_{\mathrm{lab}}^{\mathrm{p}^+} \approx f_{\mathrm{S}}^{\mathrm{p}^+}$, but also with fluxes up to 7 $f_{\mathrm{S}}^{\mathrm{p}^+}$ (at 2.25 AU). In both cases the results are comparable. Choice of high proton fluxes is necessary to extrapolate of short term laboratory results on long term space missions effects.

Results of the performed laboratory irradiation experiments are compared with the presented model of bubble growth. The results of the model calculations coincide very well with observations of bubble growth made in laboratory. I have proven that the conditions in the near vicinity of the Sun (from 1.75 to 2.85 AU) are favorable for the bubble growth process. Therefore, the model presented in this thesis provides a useful tool for well-founded forecasts of degradation effects under space conditions.

Zusammenfassung

Gegenstand dieser Dissertation ist die Materialdegradation unter Weltraumbedingungen. Metalle werden häufig in der Raumfahrttechnologie verwendet. Ihr Verhalten im interplanetaren Raum ist immer noch nicht vollständig untersucht und verstanden. Mit dieser Dissertation präsentiere ich einen ersten Versuch, die Alterung von Metallen durch das Bombardement mit niederenergetischen Protonen zu modellieren und das Modell experimentell zu verifizieren.

Die Dissertation konzentriert sich auf den Prozess der sogenannten Wasserstoffversprödung, d.h. auf die Bildung von Blasen aus molekularem Wasserstoff auf der Matalloberfläche. Dieser Prozess beruht auf der Rekombination der solaren Protonen mit den freien Metallelektronen zu neutralen Wasserstoffatomen. Im Fall solarer Protonen führen drei Prozesse zur Rekombination: der Auger-, der resonante und der Oppenheimer-Brinkman-Kramers (OBK)-Prozess. Es wird eine detaillierte mathematische Beschreibung dieser Prozesse gegeben.

Um das Blasenwachstum auf Metallen zu untersuchen, habe ich die Komplexe Bestrahlungseinrichtung (KOBE) des DLR genutzt. Die Parameter des Linear-Protonenbeschleunigers gestatten es, den Protonenfluss mit dem im interplanetaren Raum zu skalieren. Der Blasenbildungsmechanismus wird aber erst vollständig verstanden, wenn die Metalle gleichzeitig mit Protonen auch der elektromagnetischen Strahlung, insbesondere der kurzwelligen unter 400 nm (UV-Bereich), ausgesetzt sind. Das wird Gegenstand meiner zukünftigen Forschungen sein. Durch UV-Strahlung verursachte Photoionisation und Photodissoziation können die Dynamik des Blasenwachstums verändern. Hochenergetische Photonen können die dünne Blasenoberfläche durchdringen und das H_2-Gas dissozierieren. Infolgedessen können die H-Atome aus der Blase diffundieren und die Größe der Blase effektiv reduzieren. Diese Hypothese wird überprüft. Deshalb wird in dieser Dissertation auch die aufwändige Validation der zu KOBE gehörigen Vakuum-UV-Simulators dargestellt, an welcher ich mitgearbeitet habe.

Ich habe ein thermodynamisches Modell des Blasenwachstums entwickelt. Dieses Modell basiert auf der Annahme, dass dieser Prozess quasistatisch verläuft. Das heisst, dass das Blasenwachstum deutlich langsamer erfolgt als die Wasserstoffrekombination und dass ein thermodynamisches Gleichgewicht existiert wenn die H_2-Moleküle in die Blasen wandern. Infolge dieses Prozesses ist das betrahlte Metall mit halbkugelförmigen Blasen bedeckt. Es wird eine quantitative Relation zwischen der Reflektivität des Metalls, der Oberflächendichte der Blasen und ihrer Radien hergeleitet. Außerdem habe ich sowohl theoretisch als experimentell gezeigt, dass die Blasenbildung zu einer Verringerung der Reflektivität führt, was Änderungen der thermo-optischen Eigenschaften der bestrahlten Metalloberfläche verursacht. Es werden verschiedene Protonenflüsse untersucht. Die Bestrahlungstests wurden mit Flüssen durchgeführt, welche denen im Weltraum ähneln, $f_{\mathrm{lab}}^{\mathrm{p}^+} \approx f_{\mathrm{S}}^{\mathrm{p}^+}$, aber auch mit Flüssen bis zu 7 $f_{\mathrm{S}}^{\mathrm{p}+}$ (bei 2.25 AU). In beiden Fällen sind die Ergebnisse vergleichbar. Die Wahl hoher Protonenflüsse ist notwendig, um von kurzzeitigen Laborexperimenten auf Langzeitmissionen im Weltraum extrapolieren zu können.

Ich vergleiche die Ergebnisse der im Labor durchgeführten Bestrahlungstests werden mit denen des

mathematischen Modells der Blasenwachstums. Das Modell stimmt recht gut mit den experimentellen Ergebnissen überein und kann somit zur Vorhersage des realen Blasenwachstums verwendet werden. Ich zeige, dass die Bedingungen (Protonenflüsse und Temperaturen) in Sonnennähe (von 1.75 zu 2.85 AU) das Blasenwachstum ermöglichen. Deshalb ist das in dieser Dissertation entwickelte Modell ein nützliches Werkzeug, um gut fundierte Voraussagen über Degradationseffekte unter Weltraumbedingungen in diesem interplanetaren Bereich zu liefern.

Chapter 1

Introduction

The importance of degradation processes of materials used in space technology is undeniable. All of the materials planned for space applications in which they will be exposed to the radiation in space have to be evaluated for their behavior under particle and electromagnetic irradiation [1, 2]. It is known from many of these evaluation tests that particle and electromagnetic radiation can significantly degrade materials and lead to changes in their mechanical behavior or thermo-optical properties (see e.g. [3, 4, 5, 6]). These changes can cause early failures of satellite components or even failures of complete space missions [7].

The thermo-optical properties of materials are defined by a pair of parameters: the solar absorption coefficient α_{S}, and the thermal emission coefficient ϵ_{t}. According to the ECSS standard (European Cooperation for Space Standardization), α_{S} is defined as ratio of the solar radiant flux absorbed by a material (or body) to that incident upon it [8], while ϵ_{t} is the ratio of the radiant intensity of the specimen to that emitted by a black body radiator at the same temperature and under the same geometric and wavelength conditions [8].

Especially sensitive for any changes of thermo-optical properties are those materials which are exposed directly to the solar wind. For instance that is the case with solar sails. A solar sail is basically a large sheet of highly reflecting material bound to the deploying system by composite materials. The propulsion system of the sail is based on the momentum transfer made by solar photons. First concepts of sail-crafts have been made by several authors including the father of Astronautics, Konstanty Ciołkowski, also by Fridrikh Tsander and Herman Oberth [9]. Due to technological reasons the sail concept has been forgotten for more than 30 years. The idea returned to the scientific and engineering arena after the article of Richard Garwin [10] has been published. After that, a significant amount of both theoretical and practical work has been performed to establish solar sailing as a propulsion technology, considering its astrodynamics, mission applications and technological requirements [9].

The revitalization of the solar sail propulsion technology at the DLR-Institute of Space Systems is one of the motivations for the thesis presented here. Within the 3-step DLR-ESA project "GOSSAMER" [11] extensive degradation studies of solar sail materials have to be performed. It was decided to organize the project in three steps with increasing complexity and sail area. GOSSAMER-1, -2 and -3 are devoted to different orbits. Since sails will operate in different orbits, their materials will be exposed to different environmental conditions. Each sail mission requires specific investigations according to the erosion processes which may happen. Laboratory tests have proven the surface destroying effect of particle and electromagnetic irradiation. However, no samples of materials, that have been exposed to irradiation with solar protons in the interplanetary space, have ever been returned to Earth. The real process of material degradation in space is yet unexplored. Therefore, this thesis is intended to provide tools for estimates how much materials can suffer from the solar wind

under space conditions.

Degradation may be caused by charged particles, electromagnetic radiation, Atomic Oxygen (ATOX) as well as space debris and micro-meteorites. In this thesis I put special attention to effects of irradiating protons. In Low Earth Orbits (LEOs) ATOX is the main source of degradation, while in the interplanetary medium the solar wind and solar electromagnetic radiation dominate the degradation effects. Solar wind consists of charged particles, mainly protons and electrons. They originate from coronal mass ejections and solar flares. Electrons with energies from about 0.01 eV up to a few hundreds of eV come from coronal mass ejections. Flares are the sources of electrons with energies from 1 MeV up to hundreds of MeV. The solar protons carry energies from 0.2 keV to a few tens of keV in the solar wind and in coronal mass ejections. Up to a few GeV-protons are produced in solar flares [12].

The structure of the thesis is as follows. In Chapter 2 the literature review of the interaction of the incident particles with matter is presented. The main content of this section is focused on recombination processes of incident protons with the free electrons of metals. Protons penetrating metallic targets lose their energy and repeatedly bound and lose an electron. At rest all of the incident protons recombine with free electrons present in any metal. Depending on the kinetic energy of incident protons, four recombination processes can be distinguished: Auger- (Subsection 2.4.1), resonant- (Subsection 2.4.2), Oppenheimer-Brinkman-Kramers- (Subsection 2.4.3), and the Radiative Electron Capture - process. For solar protons the first three phenomenon dominate the recombination.

Chapter 3 describes the Complex Irradiation Facility (CIF) which I used to study the degradation processes presented in this thesis. I have published its technical description in a review scientific journal named *Journal of Materials Science and Engineering A* [13]. The configuration of the CIF is in detail presented in Subsection 3.1. Subsection 3.2 explains working principle of the dual beam proton/electron irradiation system of the CIF. Next, the Subsection 3.3 is devoted to two electromagnetic sources of the CIF: the solar simulator and the Deuterium lamp. The main part of the Chapter is the description of the Vacuum-UV simulator i.e. its design, performance and calibration, Subsection 3.4.1. I took part in the calibration procedure in the radiometry laboratory of the Physikalisch-Technische Bundesanstalt (PTB) at Berlin Electron Storage Ring for Synchrotron Radiation of Helmholtz Zentrum Berlin (BESSY II) in Berlin-Adlershof. The source was calibrated in the wavelength range from 40 to 410 nm. I worked the raw data from the calibration procedure provided by the PTB to estimate the source spectra. I made the spectra line identification by use of the NIST database [14]. I compared also the VUV emission lines with the solar ones. To do that, I have used the SUMER database [15]. Then, I have used the spectra to estimate the stability of the source, i.e. maximum deviation of the light intensity as a function of wavelength range. I have calculated the acceleration factors in a case of considered three gas flows as well as different wavelength ranges. My calculations together with description of the calibration procedure have been published in a review scientific journal *Advances in Space Research* [16].

Chapter 4 is devoted to degradation processes of materials under space conditions. A short literature review of the most important erosion processes is presented. The possibility to charge metallic foils by solar wind is investigated (Subsection 4.1.1). Then the sputtering, an important degradation process which describes a removal of target's atoms by incident particles, is shortly described (Subsection 4.1.2). The process leads to mass loss of irradiated materials and is important for long term space missions. Next, the effects of ATOX are discussed (Subsection 4.1.3). ATOX is highly concentrated in the LEO regions. The concentration depends on altitude as well as on the activity of the Sun. Then a few experimental facts of exposure of a collection of materials used in space technology to the electromagnetic radiation are presented in Subsection 4.1.4.

In Section 4.2 I propose a degradation process which may appear in the interplanetary medium:

a formation of molecular Hydrogen bubbles on metallic surfaces exposed to solar protons. Hydrogen is created in the sample by incident protons which recombine with its free electrons. Surfaces covered with bubbles will change its thermo-optical properties. The proposed blistering phenomenon will play a crucial role in the planned solar sail missions, since any change of the properties of its material leads to changes of the propulsion efficiency of the sail-craft or even to a failure of the entire mission. The Chapter presents also a collection of experimental facts about bubble formation. Many materials have been investigated, for instance: Aluminum, Copper, Iron, Tungsten, Palladium, Tantalum, and Vanadium, with H^+ and H_2^+ ions as incident particles.

Then I have investigated the possibility of bubble formation under space conditions, Subsection 4.2.1. Characteristic temperatures as well as proton fluxes necessary for the formation are given. However, the material located either to close or to far away to the Sun will not suffer from bubble formation.

I developed model of bubble growth mechanism. It is presented in Subsection 4.2.2. It is a thermodynamic approach. The model is based on the assumption that the bubbles grow in a quasistatic way, i.e. during each time step a small portion of H_2 molecules is merged to the bubbles and an equilibrium is rapidly re-established.

My second model describes reflectivity of Aluminum samples covered with different surface densities and different sizes of bubbles, Subsection 4.2.3. The derived relation between bubble size and their surface density to the reflectivity of irradiated materials provides a direct link to the solar sail propulsion efficiency, since the acceleration of the sail-craft is directly proportional to the reflectivity of sail material.

Chapter 5 describes experimental studies which I have performed by use of the CIF. The experiments are focused on bubble formation phenomenon on vacuum deposited Aluminum after proton bombardment. Bubble formation due to proton dose (Section 5.1), proton kinetic energy (Section 5.2), and temperature of the samples (Section 5.3) is investigated. Different proton fluxes are considered. It is necessary to extrapolate of short term laboratory results on long term space mission effects. I have proven that bubbles are formed only at specific conditions. For bubble formation the most important parameters are: the samples' temperature and the proton dose. The bubbles are formed when the temperature of the vacuum deposited Aluminum layers varies from 300 to 383 K. The minimum required proton dose to initiate the process should exceed 10^{16} p^+cm^{-2}. I have proven that such conditions are achievable in the interplanetary space. I have supplemented the results by reflectance measurements made by use of the DLR's Bruker 80v spectrometer, Subsection 5.3.1. After bubble formation the foils' reflectance decreases in comparison to the non-irradiated specimens, Subsection 5.3.2. The larger the bubble size and the larger the bubble surface density, the larger the reflectance decrease. The thermodynamic model together with its experimental validation presented within this Chapter have been published in a review scientific journal *Advances in Space Research* [17].

Finally in the Chapter 6 the Conclusions & Outlooks are presented.

Chapter 2

Interaction of the incident particles with matter

Three types of interactions of incident particles with matter can be distinguished. First, *elastic scattering* - it takes place when the kinetic energy of the collision partners is conserved. Elastic scattering is also a source of heating of metallic foils, because there is a transfer of kinetic energy from the incident particle to the ions of the target [18]. Second, *non-elastic scattering* - where the internal energy of particles is changed. It is not a creation process of new particles but a source of destruction of crystals and molecular chains [18]. This phenomenon will be considered in Chapter 4. Third, *nuclear reactions* - in the result new particles are created [19, 20]. For such reactions high energetic particles are needed. These physical processes will not be considered in this thesis due to the fact that the Sun generates mostly low energetic particles, see Fig. 4.11. Their energy is much lower to initiate nuclear reactions with target atoms.

The total and differential cross section are tools to study irradiation processes and their properties. One can estimate energy loss per unit length by ionization and excitation when thin materials are bombarded with charged particles. These physical processes are described by the Bohr formula, and will be studied in detail in the following sections.

2.1 Total and differential cross section

The thicker the irradiated metallic foil, the smaller the number of the incident particles at a constant energy that will penetrate it and leave the foil at its back side. Thus the initial particle number decreases with increasing depths.

The basic assumption of the concept of the total cross section Σ_{total} is that each target ion represents a total cross section. If an incident particle strikes such an area, it will be scattered. Otherwise it will not interact [21]. If the foil has a thickness of Δx, which is called the *penetration length parameter* measured in gcm^{-2} and n_0 is the number of lattice ions in the unit volume, the probability $P(x)$ that incident particle scatters in Δx is [21]:

$$P(x) = \frac{\Sigma_{\text{total}} n_0}{\rho} \Delta x, \tag{2.1}$$

where ρ is the density of the material. Whenever a particle scatters, number of particles $N_{\text{particles}}$ at distance x decreases by the value of $dN_{\text{particles}}$:

$$dN_{\text{particles}} = -N_{\text{particles}} P(x). \tag{2.2}$$

By use of the so-called attenuation coefficient $\mu = \frac{\Sigma_{\text{total}} n_0}{\rho}$ an integral of Eq. 2.2 returns a simple formula between an initial intensity $I_{\text{particles},0}$ and the intensity $I_{\text{particles}}$ at a given depth x. Intensity is the number of incident particles per unit time $I_{\text{particles}} = N_{\text{particles}}/t$, where $N_{\text{particles},0}$ is the number of incident particles [12, 20, 22, 23]:

$$I_{\text{particles}} = I_{\text{particles},0} e^{-\mu x}. \tag{2.3}$$

The attenuation coefficient depends on the physical properties of foils and on the energy of the incident particles [12]. Eq. 2.3 is correct under the following assumptions:

1. The decrease of the incident particle intensity is proportional to the number of collisions centers in the foil where kinetic energy can be dissipated.

2. The character of interactions does not depend on the thickness of a metallic foil [19, 20].

The total cross section is a great theoretical tool to study many physical problems. However, it will be insufficient to get the angular distribution of scattered particles. In that situation the concept of the differential cross section is used [20].

The initial path of inflowing particles is bended by metallic foil ions. The deflection angle δ is gradually different from zero. The impact parameter ξ is defined as closest distance of the incident particle with respect to the ion [18, 20, 24]. The range of deflection angles corresponds to a ring of impact parameters. The inner and outer radius is ξ and $\xi + d\xi$, respectively. The equation for the differential cross section is:

$$d\Sigma = 2\pi\xi d\xi. \tag{2.4}$$

By determining two independent relations for the change in the momentum Δq of the scattered initial particle, it is possible to find a general relation between the impact parameter ξ and the scattering angle δ [24]. δ varies from 0 to π. From the classical theory of electrodynamics the force F_{C} acting between two charges ze and Ze, being in a distance r to each other is:

$$F_{\text{C}} = \frac{zZe^2}{4\pi\epsilon_0 r^2}. \tag{2.5}$$

Now the momentum transfer Δq may be written as [24] (see Fig. 2.1):

$$\Delta q = \int_{-\infty}^{\infty} F_{\text{C}} \cos\phi dt = \frac{zZe^2}{4\pi\epsilon_0} \int_{-\frac{\pi-\delta}{2}}^{\frac{\pi-\delta}{2}} \frac{cos\phi}{\omega_0 r^2} d\phi, \tag{2.6}$$

where ω_0 is the angular frequency, ϕ is the angle between radius vector r and the bisector [24]. As seen in Fig. 2.2, the angular momentum $\boldsymbol{L} = \boldsymbol{r} \times m\boldsymbol{v}$ at points A and B is given by:

$$L_{\text{point A}} = rmv \sin\frac{\pi}{2} = m\omega_0 r^2, \tag{2.7}$$

$$L_{\text{point B}} = rmv \sin\psi = rm\xi. \tag{2.8}$$

The conservation of angular momentum in an elastic scattering process, $L_{\text{point A}} = L_{\text{point B}}$, returns for the angular frequency:

$$\omega_0 = \frac{v\xi}{r^2}, \tag{2.9}$$

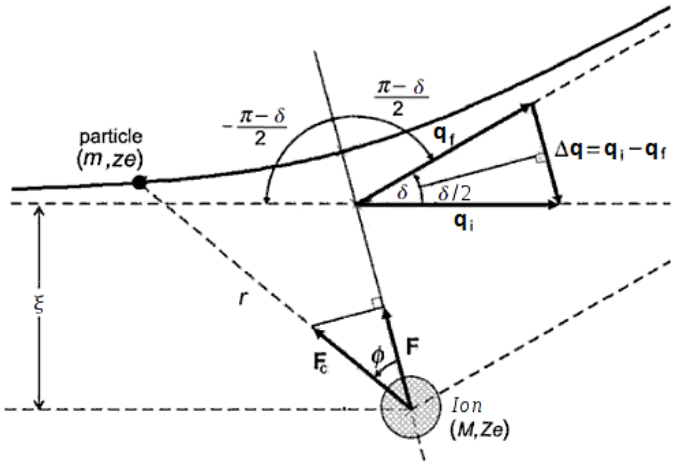

Figure 2.1: Scattering of an incident particle on a metallic foil ion, where Δq is the change in the particle momentum. The ion is located in the outer focus of the hyperbolic trajectory of the particle [24].

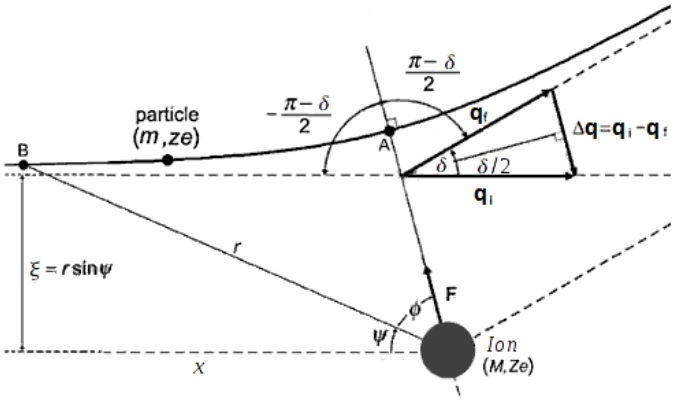

Figure 2.2: Geometry of the phenomenon. Point A is the apex of the hyperbola - trajectory of incident particle. Point B is assumed to be at large distance from the ion [24].

where m and v are the mass and velocity of the incident particle, respectively. After inserting Eq. 2.9 into Eq. 2.6 and solving the integral, the momentum transfer in the collision process is [24]:

$$\Delta q = 2\frac{zZe^2}{4\pi\epsilon_0 v\xi}\cos\frac{\delta}{2}. \tag{2.10}$$

Suggested from Fig. 2.1, if $q_\mathrm{f} = mv_\mathrm{i}$ the momentum transfer Δq may be written also as:

$$\Delta q = 2mv\ sin\frac{\delta}{2}. \tag{2.11}$$

The required relation for the impact parameter ξ is obtained after combining Eq. 2.10 and Eq. 2.11 [24]:

$$\xi = \frac{zZe^2}{8\pi\epsilon_0 E_{\mathrm{K}}} cot\frac{\delta}{2}, \tag{2.12}$$

where z and Z are the atomic numbers of an incident particle and a foil ion respectively. E_{K} is the kinetic energy of an incident particle. One can now write the Eq. 2.4 in a different form:

$$d\Sigma = 2\pi \frac{\xi}{sin\delta} sin\delta \left|\frac{d\xi}{d\delta}\right| d\delta. \tag{2.13}$$

Calculating $\frac{d\xi}{d\delta}$ and using the solid angle $d\Omega = 2\pi sin\delta\ d\delta$ one has:

$$\frac{d\Sigma}{d\Omega} = \left(\frac{zZe^2}{16\pi\epsilon_0 E_{\mathrm{K}}}\right)^2 \frac{1}{sin^4\frac{\delta}{2}}. \tag{2.14}$$

Equation 2.14 describes the differential cross section for scattered particles. It is called the Rutherford formula [20, 24]. The cross section depends on three factors:

1. If the kinetic energy of incident particles increases, then the differential cross section will decrease. Therefore, the incident particles with the lower kinetic energy will have a higher probability to be scattered off by ions of the foil.

2. For a given target foil (Ze) and given incident particle (ze, E_{K}), a large differential cross section implies a small scattering angle δ.

3. In the process of continuous irradiation of the foil with electrons and/or ions, the degree of ionization of the foil atoms (see Section 2.2) grows, hence, the degradation process may be characterized by the increase of the differential cross section.

2.2 Energy loss per unit length by ionization and excitation

Collisions with ions of the metallic foil are caused by incident particles which penetrate the material, hence ions can get additional energy. Atoms can be excited or ionized, while the incident particles lose their energies simultaneously [20]. If the energy loss per unit length per ion is known, one can calculate the energy loss per unit length of an incident particle, which penetrates the foil: $-dE/dx$. It is proved experimentally, that this quantity depends on the type and on the energy of the incident particle and on the physical properties of the metallic foil [19, 20]. The required formula is obtained by use of the principle of conservation of energy and momentum, taking into account also the geometry of the phenomenon. Only perpendicular forces act on the incident particle. Forces parallel to the line of flight are canceled out by the symmetry [18]:

$$F = \frac{zZe^2}{4\pi\epsilon_0 r^2} \sin\psi, \qquad dt = \frac{dx}{v}, \tag{2.15}$$

where dx is the path of the incident particle which moves in unit time dt and where $\sin\psi = \frac{\xi}{r}$. Now, using the geometry of the collision process (Fig. 2.2):

$$\frac{\xi}{x} = \tan\psi, \qquad r = \frac{\xi}{\sin\psi}, \qquad dx = -\frac{\xi}{\sin^2\psi} d\psi. \tag{2.16}$$

The momentum transfer Δq of the incident particle [18] is:

$$\Delta q = \int_{-\infty}^{\infty} F dt = -\frac{zZe^2}{4\pi\epsilon_0 \xi v} \int_0^{\pi} \sin\psi d\psi, \tag{2.17}$$

and the energy transfered to the metallic foil nuclei is [18]:

$$\frac{\Delta q^2}{2M} = \frac{1}{2M}\left(\frac{zZe^2}{2\pi\epsilon_0 \xi v}\right)^2. \tag{2.18}$$

The energy loss rate per unit length dx is the product of Eq. 2.18 and the number of collisions in the metallic foil with impact parameter in range ξ to $\xi + d\xi$:

$$\frac{dE}{dx} = -\int_{\xi_{min}}^{\xi_{max}} n_0 2\pi\xi d\xi \frac{1}{2M}\left(\frac{zZe^2}{2\pi\epsilon_0 \xi v}\right)^2. \tag{2.19}$$

After integration, the Eq. 2.19 is:

$$\frac{dE}{dx} = -\frac{n_0}{\pi M}\left(\frac{zZe^2}{2\epsilon_0 v}\right)^2 \ln\left(\frac{\xi_{max}}{\xi_{min}}\right), \tag{2.20}$$

where M is the mass of an ion of the metallic foil material. The energy loss per unit length depends on:

- the velocity of the incident particle $\sim v^{-2}$. The higher the kinetic energy, the lower the loss rate.
- the square of the incident and ion number, z^2 and Z^2. It means that if z increases by a factor of two, the energy loss rate per unit length will increase by a factor of four, hence, Eq. 2.20 is very sensitive for changes of the atomic numbers and ionization process.
- the logarithm of ratio of the upper and lower limits of the impact parameter, i.e. its a weak dependency.

The evaluation of ξ_{max} and ξ_{min} will be studied in next subsections for the protons as incident particles. The case of relativistic protons as the incident particles will be considered as well.

2.3 Interactions of protons with matter

The previous subsection discusses the general problem of the energy loss per unit length by an incident particle. According to the experimental data [25] protons lose energy while penetrating a target mainly by collisions with electrons. Target atoms are then ionized additionally. Therefore the relation 2.20 has to be modified. The mass of the target ion M is replaced by the mass of an electron m_e:

$$\frac{dE}{dx} = -\frac{n_0}{\pi m_\mathrm{e}}\left(\frac{zZe^2}{2\epsilon_0 v}\right)^2 \ln\left(\frac{\xi_{max}}{\xi_{min}}\right), \tag{2.21}$$

Protons with kinetic energies not larger than 1 MeV are certainly non-relativistic. Flux of solar protons having energy larger than 1 MeV is approx. 10^4 smaller than for energies in the keV range. Therefore, only the non-relativistic case is considered here. The maximum value of the impact parameter ξ_max is estimated under the assumption that the metallic foil ion can be excited or ionized.

Duration of the collision is equal or longer than a circulation time of the electrons in the ion [18, 20]. Collecting these information together one can calculate the physical quantity $\xi_{\max}$ by use of the condition that the collision time (time in which incident proton interacts with the electron) equals the circulation time of the electron in the ion:

$$\frac{2\xi_{\max}}{v} = \frac{2\pi}{\omega_0}, \tag{2.22}$$

where ω_0 is the angular velocity of an electron in an ion, v is the velocity of the incident proton.

The minimum value of the impact parameter can be estimated for two cases, using either classical or quantum physics. Firstly the classical approach is considered.

If the electrostatic potential interaction energy of the incident proton and the metallic foil electron is equal to the maximum possible energy transfer (the maximum transfer of the energy to the electron by the incident proton is possible if a perfect elastic collision is assumed, then the kinetic energy becomes $\frac{1}{2}m_{\mathrm{e}}(2v)^2 = 2m_{\mathrm{e}}v^2$), it corresponds to the minimum distance of the approach [18]:

$$\frac{ze^2}{4\pi\epsilon_0\xi_{\mathrm{min_C}}} \approx 2m_{\mathrm{e}}v^2, \qquad \xi_{\mathrm{min_C}} \equiv \xi_{\mathrm{min_{Classical}}}, \tag{2.23}$$

where v is the velocity of the incident proton in the laboratory frame.

Secondly, the quantum approach to the minimum impact parameter is applied. The maximum velocity transfer to the electron is $2v$, hence change of its momentum is $\Delta q = 2m_{\mathrm{e}}v$. In quantum physics both the position and velocity cannot be determined with infinit accuracy. It is well known fact called the Heisenberg Uncertainty Principle $\Delta x > \hbar/4m_{\mathrm{e}}v$ [18], hence:

$$\xi_{\mathrm{min_Q}} = \frac{\hbar}{4m_{\mathrm{e}}v}, \qquad \xi_{\mathrm{min_Q}} \equiv \xi_{\mathrm{min_{Quantum}}}. \tag{2.24}$$

It is important to find a criterion whether the classical or quantum approach is appropriate. This can be done by studying the ratio of the two impact parameters:

$$\frac{\xi_{\mathrm{min_Q}}}{\xi_{\mathrm{min_C}}} = \frac{2\pi\epsilon_0\hbar v}{zZe^2}. \tag{2.25}$$

The term $e^2/4\pi\epsilon_0 c\hbar$ can be replaced by the so-called fine structure constant $\alpha_{\mathrm{C}} \approx 1/137$. Therefore, Eq. 2.25 receives a much simpler form:

$$\frac{\xi_{\mathrm{min_Q}}}{\xi_{\mathrm{min_C}}} = \frac{1}{2zZ\alpha_{\mathrm{c}}}\frac{v}{c}. \tag{2.26}$$

When the Eq. 2.26 is larger than unity, the quantum approach should be used, otherwise classical one.

Finally the energy loss rate per unit length for non-relativistic energies of protons is [18]:

$$\frac{dE}{dx} = -\frac{n_0}{\pi m_{\mathrm{e}}}\left(\frac{ze^2}{2\epsilon_0 v}\right)^2 \ln\left(\frac{8\pi^2\epsilon_0 m_{\mathrm{e}}v^3}{\omega_0 ze^2}\right). \tag{2.27}$$

The corresponding formula for quantum case is:

$$\frac{dE}{dx} = -\frac{n_0}{\pi m_{\mathrm{e}}}\left(\frac{ze^2}{2\epsilon_0 v}\right)^2 \ln\left(\frac{4\pi m_{\mathrm{e}}v^2}{\hbar\omega_0}\right). \tag{2.28}$$

Equation 2.28 can be rewritten into a more simple and usable form. First step is to replace $\hbar\omega_0$ by its relation to the binding energy $\frac{1}{2}\hbar\omega_0$ of the electron in Bohr's description [18]. The binding energy is also the ionization potential I_p which should be a properly weighted mean over all states of the electrons in the metallic foil ions $\bar{I}_\mathrm{p}$ that ionization potential has to be found experimentally [18]. Term in the logarithm turns to be:

$$\ln\left(\frac{2\pi m_\mathrm{e} v^2}{\hbar\omega_0}\right) \equiv \ln\left(\frac{2m_\mathrm{e} v^2}{\bar{I}_\mathrm{p}}\right), \tag{2.29}$$

In classical approach the energy loss per unit length depends almost on the same conditions as in Eq. 2.21, because logarithm yields a relatively small correction only.

However, the exact formula of the energy loss per unit length of incident proton in the quantum approach together with relativistic corrections is known as the Bethe-Bloch formula [26]:

$$-\frac{dE}{dx} = \frac{n_0}{\pi m_\mathrm{e}}\left(\frac{ze^2}{2\epsilon_0 v}\right)^2\left[\ln\left(\frac{2\gamma^2 m_\mathrm{e} v^2}{\bar{I}_\mathrm{p}}\right) - 2\ln\gamma + \gamma^{-2} - 1\right]. \tag{2.30}$$

The second and the third terms are correction factors that are neglected for low velocities of the incident particles [26]. The Bethe - Bloch formula depends on:

- the velocity of the incident particle. The increase of that velocity decreases the energy loss per unit length.
- charge z of the incident particle (here proton). With an increase of the charges, the loss per unit length increases too.

2.4 Recombination of electrons and protons to Hydrogen

Rausch von Traubenberg and Hahn in 1922 have discovered for the very first time a proton recombination process [27]; they used thin films as targets. Basic aspects of two-electron Auger recombination of low energy ions at surfaces, originally proposed by Shekhter already in 1937, has been described extensively within a probability model by Hagstrum [28]. In 1987, Taute considered variability of Auger recombination rate as a function of an ion velocity. There have been considered small grazing angles [27, 29].

In solids four processes of recombination of incident H^+ ions (protons) with electrons to neutral Hydrogen atoms are known:

1. the Auger process,
2. the resonant process,
3. Oppenheimer-Brinkman-Kramers (OBK) process,
4. Radiative Electron Capture (REC) process.

Since the solar wind consists mainly of low ($\leq$ 100 keV) energetic protons only the first three processes will be considered in this thesis. The Auger process dominates the total cross section [30]. According to Raisbeck and Yiou [31] for protons the REC process dominates the recombination only above proton energies of about 300 MeV (for Al foil); therefore this process will be not discussed here.

For each of these recombination processes the rate Γ of capture (recombination rate) or loss (ionization rate) of an electron can be calculated. The cross section per atom for each charge exchange process is defined by [32]:

$$\Sigma = \frac{\Gamma}{n_0 v}, \tag{2.31}$$

where v is the ion speed and n_0 is the number density of material ions.

The plan of this section is as follows: first a short introduction to the Hydrogen atom in a classical and quantum approach is made. Next a description of conditions which have influence to the number of free electrons in solids is made. Finally the recombination processes are described.

The Hydrogen atom - quasi-classical approach

The classical description of the Hydrogen atom is based on two assumptions:

1. An electron with mass m_e in an atom orbits with a radius $r_e(n)$ and velocity $v_e(n)$ the proton. n is a number of the shell. The angular momentum is defined as:

$$m_e v_e(n) r_e(n) = n\hbar, \qquad n = \{1, 2, 3, ...\}. \tag{2.32}$$

2. An atom emits a photon of electromagnetic radiation when an electron jumps to lower shell. On the other hand it jumps to higher shell when it absorbs a photon. The energy difference ΔE is proportional to the frequency of the electromagnetic radiation ν:

$$\Delta E = h\nu. \tag{2.33}$$

Radius, velocity and energy of an electron at the n'th shell are calculated by use of both Bohr's assumptions and the balance of the centripetal and Coulomb forces:

$$r_e(n) = \frac{n^2\hbar^2}{m_e e^2}, \qquad v_e(n) = \frac{e^2}{n\hbar}, \qquad E(n) = -\frac{1}{n^2}\frac{m_e e^4}{2\hbar^2}. \tag{2.34}$$

For $n = 1$, the minimum radius (the Bohr radius) and the energy (the Bohr energy) for an electron are:

$$r_0 = \frac{\hbar^2}{m_e e^2} \cong 5.29 \times 10^{-9} \text{ cm}, \qquad \mathrm{E_{Bohr}} = -\frac{\mathrm{m_e e^4}}{2\hbar^2} \cong -13.6 \text{ eV}. \tag{2.35}$$

The Hydrogen atom - quantum approach

In quantum physics a state of a considered system is described by so-called *state function* or *state vector* which lives in a complex Hilbert space. In quantum description, physical quantities like position, momentum or energy are described by so-called *Hermitian operators*. To calculate physical quantities one has to solve a *state equation*. The calculated quantities are called eigenvalues. Eigenvalues are measured in physical experiments. In quantum mechanics state equation of the energy operator is called the Schroedinger equation. An introduction to quantum mechanics can be found e.g. in [21].

In quantum physics the Hamiltonian of the Hydrogen atom and the stationary Schrödinger equation are:

$$H = -\frac{\hbar^2}{2m_e}\boldsymbol{\nabla}^2 + V(r), \qquad H\psi(r,\theta,\phi) = E\psi(r,\theta,\phi), \tag{2.36}$$

where $V(r)$ is the potential energy, $V(r) = -\frac{e^2}{r}$. The state function is written in spherical coordinates as [33, 34]:

$$\psi(r,\theta,\phi) = \frac{R_{n,l}(r)}{r} Y_{l,m}(\theta,\phi), \tag{2.37}$$

while its angular part is described by spherical harmonics $Y_{l,m}(\theta,\phi)$. The radial part fulfills the following ordinary secondary differential equation [33, 34]:

$$\frac{d^2R_{n,l}(r)}{dr^2} + \left\{\frac{2m_e}{\hbar^2}\left(E(n) + \frac{e^2}{r}\right) - \frac{l(l-1)}{r^2}\right\} R_{n,l}(r) = 0, \qquad l = \{0,1,2,...\}. \tag{2.38}$$

Here l is the orbital quantum number. The energy of an electron at the n'th shell is:

$$E(n) = -\frac{1}{n^2}\frac{m_e e^4}{2\hbar^2}, \tag{2.39}$$

which is the same result obtained from classical approach (see Eq. 2.34). The radial part of the state function is:

$$\frac{R_{n,l}(r)}{r} = e^{-ik_n r} r^l L_{n+1}^{2l+1}(2k_n r), \tag{2.40}$$

where $k_n = \sqrt{-\frac{2m_e E(n)}{\hbar^2}}$ and $L_{n+1}^{2l+1}(x)$ is the Laguerre polynomial:

$$L_{n+1}^{2l+1}(x) = \frac{d^{2l+1}}{dx^{2l+1}}\left\{e^x \frac{d^{n+l}}{dx^{n+1}}\left(x^{n+l}e^{-x}\right)\right\}. \tag{2.41}$$

A detailed derivation can be found in the standard text books [33, 34, 35].

Number of free electrons in solids

Each metallic solid at given physical conditions (temperature, pressure) has an approximately constant number of free electrons. A possibility to change the number is to irradiate the target by particles.

The number of lattice ions per unit volume is:

$$n_0 = \frac{N_A \rho}{M_{\mathrm{u}}}, \tag{2.42}$$

where N_A is the Avogadro's number (6.022×10^{23} mol^{-1}), ρ the density of a given material, M_{u} is the molar mass, it is 27 g mol^{-1} for Aluminum and n_0 is 6.026×10^{22} atoms cm^{-3}.

According to [36] one can estimate a number of free electrons n_e per one lattice atom as a function of conductivity σ:

$$\frac{n_e}{n_0} = \left(\frac{3}{8\pi}\right)^{\frac{1}{2}} \frac{1}{n_0}\frac{h^{\frac{3}{2}}}{e^3}\left(\frac{\sigma}{\overline{l}}\right)^{\frac{3}{2}}, \tag{2.43}$$

Here $\bar{l}$ is the mean free path. The conductivity σ is related to the resistivity ϱ, $\sigma = 1/\varrho$ [36]. The resistivity obeys the Matthiessen's rule (not satisfied for Noble metals: Ruthenium, Rhodium, Palladium, Silver, Osmium, Iridium, Platinum and Gold) [37]:

$$\varrho_{\text{total}} = \varrho(T) + \varrho_{\text{impurities}}(x_{\text{imp}}) + \varrho_{\text{crystal imperfections}}, \tag{2.44}$$

where x_{imp} is mole fraction of an element. The first term of this formula is given by the Bloch - Grüneisen relation [37]:

$$\varrho(T) = \varrho(0) + A\left(\frac{T}{\Theta}\right)\int_0^{\frac{\Theta}{T}} \frac{x_{\text{imp}}^{n_{\text{i}}}}{(e^{x_{\text{imp}}}-1)(1-e^{-x_{\text{imp}}})}dx_{\text{imp}}. \tag{2.45}$$

Here A is a constant number that depends on a velocity of the electrons at the Fermi surface and the Debye radius and a density of electrons in the metal. Θ is the Debye temperature, n_{i} is an integer, where [37, 38]:

- $n_{\text{i}} = 2$ means that resistivity is determined by electron - electron interactions,
- $n_{\text{i}} = 5$ means that resistivity is determined by scattering of electrons by phonons.

If the target contains a mole fraction x_{imp} of an element and $1 - x_{\text{imp}}$ of an another element, the relation $\varrho(x_{\text{imp}})$ can be described by Nordheim's rule [37]:

$$\varrho(x_{\text{imp}}) \sim x_{\text{imp}}(1 - x_{\text{imp}}). \tag{2.46}$$

The rule has been checked experimentally, see Fig. 2.3. One can see the quadratic relation between the resistivity and the percentage of an impurity.

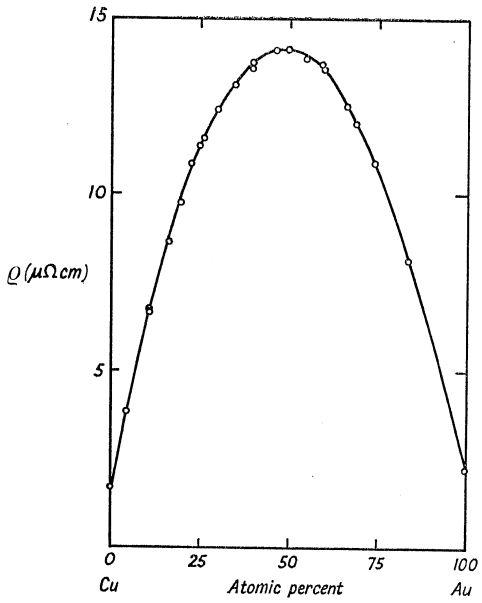

Figure 2.3: Nordheim's rule: resistivity as a function of the percentage of impurities [37]. The open cycles represent measurements; solid curve: the relation $\varrho(x_{\text{imp}}) \sim x_{\text{imp}}(1 - x_{\text{imp}})$.

The third component of the Eq. 2.44 describes the contribution to the resistivity from dislocations:

$$\varrho_{\rm D} \sim 2.3 \times 10^{-19} N_{\rm D} \quad [\Omega{\rm cm}], \tag{2.47}$$

where $N_{\rm D}$ is the number of dislocations [37].

2.4.1 Auger recombination

According to [30, 32, 39, 40, 41, 42, 43] in the Auger process, an electron is captured (or lost) by the incident ion to (or from) a bound state with incident ion assisted by a third body, an electron-hole pair. A scheme of the electron-hole Auger process (electron capture) is shown in the Fig. 2.4.

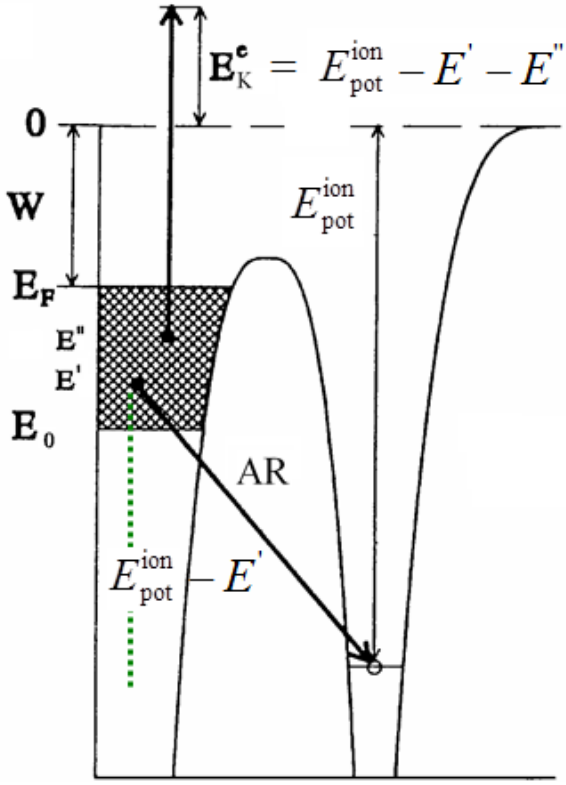

Figure 2.4: Energetic representation of the Auger process. Electrons in the conduction band have energies between E_0 and the Fermi's energy $E_{\rm F}$. W denotes the work function, $E_{\rm pot}^{\rm ion}$ is the potential energy of the incident ion, and $E_{\rm K}^{e}$ is the kinetic energy of the Auger electron.

According to Fig. 2.4 the energy conservation of the process can be written as:

$$E_{\rm initial} = E_{\rm ion} + E', \tag{2.48}$$

$$E_{\rm final} = E_{\rm neutral} + E_{\rm K}^{\rm e}, \qquad E_{\rm K}^{\rm e} = E_{\rm pot}^{\rm ion} - E' - E''. \tag{2.49}$$

Here, $E_{\rm initial}$ is the energy of the initial configuration of the system. At the initial state the incident ion is penetrating the target having the total energy of $E_{\rm ion}$. To recombine it needs an electron from the conduction band. The electron has the energy of E'. On the other hand, $E_{\rm final}$ is the energy of the final configuration of the system, which is a neutral atom with an energy $E_{\rm neutral}$ and an ejected electron (an Auger electron) with the kinetic energy of $E_{\rm K}^{\rm e}$.

The plan of the section is as follows: first the Hamiltonian, eigenfunctions and eigenvalues of the Auger process are presented. The probability per unit time of the Auger capture and loss process is calculated by use of a semiclassical approach. Then the probability per unit time will be used to calculate the cross section of the process.

Atomic units are used i.e. $e^2 = \hbar = m_e = 1$, the Bohr radius, r_0, is the unit of length. The energy is measured in Hartrees, $1E_h$ is 27.211 eV. Vector variables are denoted by use of a bold font. The Hamiltonian of the system is:

$$H = H_0 + H_I + \sum_j \left(\frac{1}{|\mathbf{r}_j - \mathbf{r}_e|} - \frac{Z}{|\mathbf{r}_j - \mathbf{R}_I|} \right), \tag{2.50}$$

where H_0 is the Hamiltonian of the electron gas, $\mathbf{r}_j$ denotes the vector components of the j^{th} electron of the gas; $\mathbf{R}_I$ are the vector components of the ion, and $\mathbf{r}_e$ denotes the vector components of the electron in the ion-electron composite [44]. The schematic representation of the system is shown in the Fig. 2.5.

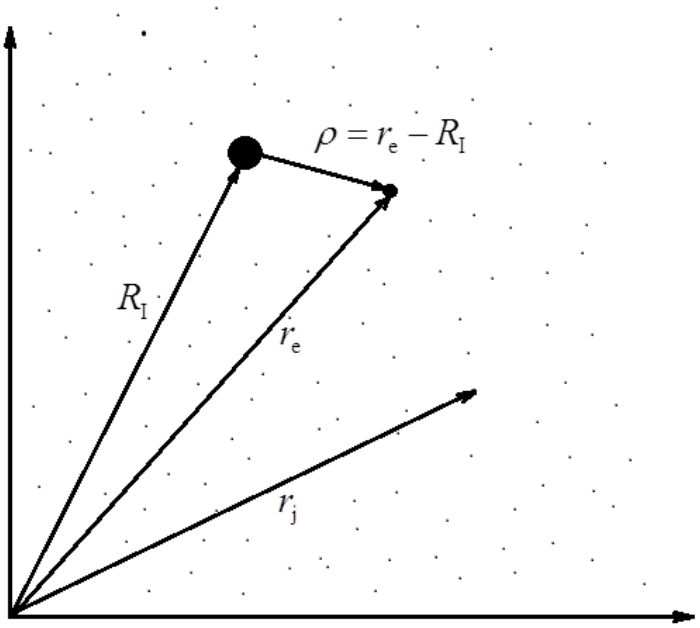

Figure 2.5: Graphical 2-D projection of the 3-D system: ion-electron and electron gas, $\mathbf{R}_I$ is the position of the incident ion, $\mathbf{r}_e$ the position of the captured electron, $\mathbf{r}_j$ the position of the j^{th} electron in the gas, and $\boldsymbol{\rho}$ is the distance between the ion and the electron.

H_I is the Hamiltonian of the ion-electron composite:

$$H_I = -\frac{1}{2M}\boldsymbol{\nabla}^2_{\mathbf{R}_I} - \frac{1}{2}\boldsymbol{\nabla}^2_{\mathbf{r}_e} - \frac{Z}{|\mathbf{R}_I - \mathbf{r}_e|}. \tag{2.51}$$

In Eq. 2.50 the term

$$\sum_j \left(\frac{1}{|\mathbf{r}_j - \mathbf{r}_e|} - \frac{Z}{|\mathbf{r}_j - \mathbf{R}_I|} \right), \tag{2.52}$$

describes the interaction between the electron gas and the ion-electron pair [44]. The eigenfunctions of H_{I} are given by:

$$\mid i\rangle = e^{i\mathbf{k}_0\cdot\mathbf{R}}u_0(\boldsymbol{\rho}), \tag{2.53}$$

with the stationary Schroedinger equation:

$$H_{\mathrm{I}} \mid i\rangle = E_{\mathrm{I}} \mid i\rangle, \tag{2.54}$$

and the eigenvalues:

$$E_{\mathrm{I}} = \frac{k_0^2}{2(M+1)} + \omega_0, \tag{2.55}$$

where

$$\mathbf{R} = \frac{\mathbf{r}_{\mathrm{e}} + M\mathbf{R}_{\mathrm{I}}}{1+M}, \tag{2.56}$$

represents the coordinates of the center of mass, $\mathbf{k}_0$ the total momentum of the composite, and $u_0(\boldsymbol{\rho})$ the wave function describing the relative motion of the electron in the composite with respect to the ion, i.e., $\boldsymbol{\rho} = \mathbf{r}_{\mathrm{e}} - \mathbf{R}_{\mathrm{I}}$ with the binding energy of ω_0 [44].

The physical description begins with the Poisson's equation for the scalar electric potential $\phi(\mathbf{r},t)$ generated at position $\mathbf{r}$ and time t by the charge density $\varrho_{\mathrm{c}}(\mathbf{r},t)$ in a medium, that is characterized by a causal dielectric constant ϵ [44]:

$$\epsilon\boldsymbol{\nabla}^2\phi = -4\pi\varrho_{\mathrm{c}}(\mathbf{r},t). \tag{2.57}$$

An incident particle with charge Z may be considered to give rise to a charge density $\varrho_{\mathrm{c}}(\mathbf{r},t) = Z\delta(\mathbf{r}-\mathbf{v}t)$ [44]. To write the equation in the momentum space, one has to use the Fourier transformation:

$$f(\mathbf{q},\omega) = \int \frac{d^3q}{(2\pi)^3}\int_{-\infty}^{\infty} d\omega\ e^{-i(\mathbf{q}\cdot\mathbf{r}-\omega t)}f_{\mathbf{r},t}, \tag{2.58}$$

where $\mathbf{q}$ is the momentum and ω the energy. Thus the density is $\varrho_{\mathbf{q},\omega} = 2\pi Z\delta(\omega - \mathbf{q}\cdot\mathbf{v})$. By use of Eqs. 2.57 and 2.58 the scalar potential is calculated:

$$\phi_{\mathbf{q},\omega} = \frac{4\pi\varrho_{\mathrm{c}}(\mathbf{q},\omega)}{q^2\epsilon(\mathbf{q},\omega)}. \tag{2.59}$$

An incident particle moving through the target with velocity $\mathbf{v}$ induces an electric field whose scalar potential is given by [39]:

$$\phi^{\mathrm{ind}}_{\mathbf{q},\omega} = \frac{8\pi^2 Z}{q^2}\delta(\omega - \mathbf{q}\cdot\mathbf{v})\left(\frac{1}{\epsilon(\mathbf{q},\omega)} - 1\right). \tag{2.60}$$

When an incident particle is passing through matter, the induced potential around the moving ion deviates from the spherical symmetry. For a charge at rest this potential is spherically symmetric, but as its velocity increases the potential loses this symmetry. A strong modification of this type should create an important effect to the state of the electron which is bound to the ion [40].

The rate of energy loss per unit time of the incident particle $\frac{dE}{dt}$ is obtained from the induced electric field $\mathbf{E}^{\mathrm{ind}} = -\boldsymbol{\nabla}\phi^{\mathrm{ind}}$ [44]:

$$\frac{dE}{dt} = -Z\mathbf{v}\cdot\mathbf{E}^{\mathrm{ind}}(\mathbf{r},t). \tag{2.61}$$

According to [44] the energy loss may be written as:

$$\frac{dE}{dt} = \int \frac{d^3q}{(2\pi)^3}\int_0^\infty \frac{d\omega}{2\pi}\, 2\omega Z\mathrm{Im}(-\phi^{\mathrm{ind}}_{\mathbf{q},\omega}) \tag{2.62}$$

It is taken only the imaginary part of the potential, i.e. imaginary part of the dielectric function: $\mathrm{Im}\left(-\frac{1}{\epsilon(\mathbf{q},\omega)}\right)$. According to Jackson [45] the imaginary part of ϵ represents the energy dissipation of an electromagnetic wave in the medium. If $\mathrm{Im}(\epsilon) < 0$ then energy is transfered from the media to the wave. $\frac{dE}{dt}$ can also be written in much more suitable form [44]:

$$\frac{dE}{dt} = \int dx\ \omega\Gamma(\mathbf{q},\omega), \qquad \int dx \equiv \int \frac{d^3q}{(2\pi)^3}\int_0^\infty \frac{d\omega}{2\pi}, \tag{2.63}$$

where $\Gamma(\mathbf{q},\omega)$ is the probability per unit time that the initial ion loses energy ω and momentum $\mathbf{q}$ [44] ($\mathbf{q}$ and ω represent the momentum and energy transferred to the solid by an incident particle [42]):

$$\Gamma(\mathbf{q},\omega) = 2Z\mathrm{Im}(-\phi^{\mathrm{ind}}_{\mathbf{q},\omega}) = \frac{16\pi^2\mathrm{Z}^2}{\mathrm{q}^2}\mathrm{Im}\left(-\frac{1}{\epsilon(\mathbf{q},\omega)}\right)\delta(\omega-\mathbf{q}\cdot\mathbf{v}). \tag{2.64}$$

Note that the energy loss per unit length dx can be written immediately by use of the Eq. 2.63:

$$\frac{dE}{dx} = \frac{1}{v}\int dx\ \omega\Gamma(\mathbf{q},\omega). \tag{2.65}$$

To adopt the result of Eq. 2.64 to the Auger process a few corrections have to be taken into account:

1. When an incident particle captures an electron that lies inside the Fermi sphere $\mid \mathbf{k}+\mathbf{v} \mid < k_{\mathrm{F}}$, where $\mathbf{k}$ is the momentum of the electron, k_{F} is the Fermi's wave number [46]. On the other hand when the particle loses an electron, an electron-hole pair is created, and $\mid \mathbf{k}+\mathbf{v} \mid > k_{\mathrm{F}}$. One can clearly imagine this situation considering the Fig. 2.4. Thus the first multiplicative correction factor to Eq. 2.64 is:

   $$\Theta(\pm k_{\mathrm{F}} \mp \mid \mathbf{k}+\mathbf{v} \mid), \tag{2.66}$$

   where $\Theta(x)$ is the step function, $\Theta(x) = 1$ when $x \geq 0$, and $\Theta(x) = 0$ when $x < 0$. Upper signs $(+/-)$ denote capture of an electron by incident ion, while lower signs $(-/+)$ loss of the electron.

2. If one looks carefully to the energy conservation of the process, Eqs. 2.48 and 2.49, it is obvious that in each single process the energy of the ejected Auger electron could be different, it mainly depends on the energy of the incident ions. Also the energy of the bound to the incident ion-electron could be different because it is inside the Fermi sphere having an energy varying in the range of E_0 to E_{F}.

   The recombination will proceed more rapidly if the coupling between the initial and final states is stronger. This coupling term is traditionally called the *matrix element*: $\langle f \mid \hat{A} \mid i\rangle$. The matrix element can be placed in the form of an integral, where the interaction which causes

the process is expressed as an operator $\hat{A}$ which acts on the initial state wavefunction. The recombination probability is proportional to the square of the integral. This kind of approach using the wavefunctions is of the same general form as that used to find the *expectation value* of any physical variable in quantum mechanics [47]. Here the initial eigenstate $|i\rangle$ is described by use of the $u_0(\boldsymbol{\rho})$ wave function; final eigenstate $\langle f|$ by use of OPW (Orthogonal Plane Wave) function $\mid \mathbf{k}_{\mathrm{OPW}}\rangle = \mid e^{i\mathbf{k}\cdot\boldsymbol{\rho}}\rangle - \langle u_0(\boldsymbol{\rho}) \mid e^{i\mathbf{k}\cdot\boldsymbol{\rho}}\rangle \mid u_0(\boldsymbol{\rho})\rangle$ [44]. An OPW is defined as a plane wave which has been made orthogonal to Bloch waves (see [46]) by use of the Schmidt process [48, 49, 50]. OPW describes the state of an electron in the conduction band in solids [44]; the method was proposed by Herring in 1940 [50]. In the literature one can find also the method proposed by Wigner and Seitz [51] which gives good results for lower states of the valence electron band of a metal, but the extension of this method to states of higher energy becomes rapidly more unreliable as the energy increases [44]. Here $\hat{A}$ is an operator for the physical interaction which couples the initial and final states of the system; $\hat{A}$ is here $e^{\pm\mathbf{k}\cdot\boldsymbol{\rho}}$. Thus the second multiplicative correction factor is:

$$\mid \langle \mathbf{k}_{\mathrm{OPW}} \mid e^{\pm\mathbf{k}\cdot\boldsymbol{\rho}} \mid u_0(\boldsymbol{\rho})\rangle \mid^2 . \tag{2.67}$$

Upper sign (+) denotes capture of an electron by the incident ion, while lower sign (−) loss of the electron.

3. Also the δ function has to be modified. The correction takes into a account capture or ejection of an electron [44]:

$$\delta(\omega - \mathbf{q}\cdot\mathbf{v} \mp \frac{k^2}{2} \pm \omega_0) \tag{2.68}$$

Upper signs (−/+) denotes capture of an electron by the incident ion, while lower signs (+/−) loss of the electron.

Thus the probability per unit time of electron capture or loss in the Auger process is [30, 39, 41, 42, 43]:

$$\begin{aligned} \Gamma_{\mathrm{A}}^{\mathrm{C,L}} \;=\; & \int \frac{d^3q}{(2\pi)^3} \int_0^\infty \frac{d\omega}{2\pi} \int \frac{d^3k}{(2\pi)^3}\, \Theta(\pm k_{\mathrm{F}} \mp \mid \mathbf{k}+\mathbf{v} \mid) \\ & \frac{16\pi^2 Z^2}{q^2} \mathrm{Im}\left(-\frac{1}{\epsilon(\mathbf{q},\omega)}\right) \delta(\omega - \mathbf{q}\cdot\mathbf{v} \mp \frac{\mathrm{k}^2}{2} \pm \omega_0) \\ & \mid \langle \mathbf{k}_{\mathrm{OPW}} \mid e^{\pm\mathbf{k}\cdot\boldsymbol{\rho}} \mid u_0(\boldsymbol{\rho})\rangle \mid^2 . \end{aligned} \tag{2.69}$$

By use of both Eqs. 2.31 and 2.69 the cross section of the Auger process, both for losing and capturing of an electron can be calculated.

According to [40, 44] the bound state wave function (the wave function describing the relative motion of the electron in the composite with respect to the ion) is assumed to be of the form:

$$u_0(\boldsymbol{\rho}) = \left(\frac{a^3}{\pi}\right)^{\frac{1}{2}} \exp(-a\boldsymbol{\rho}). \tag{2.70}$$

Guinea et al. [40] have calculated the wave functions and the binding energies, of the first and second electron bound to H atom. Results are presented in the Table 2.1.

E	First Electron		Second Electron	
keV	a	ω [a.u.]	a	ω [a.u.]
0	0.90	-0.106	0.76	-0.046
1.0	0.88	-0.096	0.072	-0.036
4.0	0.86	-0.075	0.76	-0.012
9.0	0.80	-0.048	0.54	-0.004
16.0	0.72	-0.027	0.52	-0.009
25.0	0.74	-0.027	0.58	0.010
36.0	0.82	-0.041	0.70	0.011
49.0	0.86	-0.063	0.74	0.011
64.0	0.90	-0.096	0.74	0.006
81.0	0.92	-0.125	0.72	0.005
100.0	0.94	-0.184	0.72	0.001

Table 2.1: Binding energies (ω in a.u.) and values of the parameter a defining the wave function for proton (left) and H atom (right) as a function of the energy, E, of the incidence ion. Binding energies are referred to the bottom of the conduction band [44].

The probability amplitude is calculated by use of the formula $\Pi \sim \mid u_0(\boldsymbol{\rho}) \mid^2$. Here Π predicts the position where the bound (to the incident ion) state is most probable. Results are presented in Fig. 2.6 where the incident particle is a proton. The left plot shows the situation where the first electron is bound to the proton; while in the right plot the second electron is bound to the H atom. The amplitude $\mid u_0(\boldsymbol{\rho}) \mid^2$ is plotted as a function of the distance (Y axis, in a.u.) from the incident proton or H atom and of the energy of the incident proton or H atom (X axis, in keV).

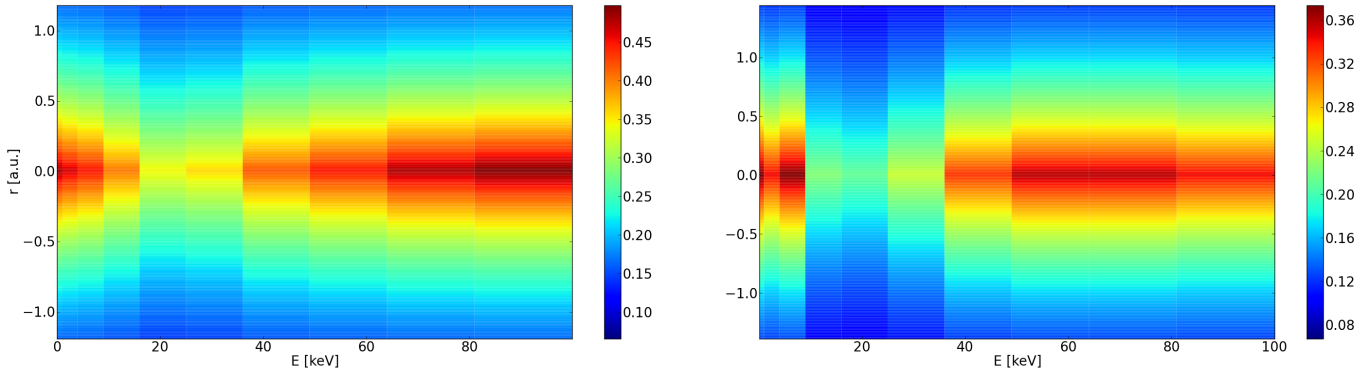

Figure 2.6: Left: first electron is bound to the H^+. Right: second electron is bound to the H atom. The density of probability is plotted as a function of the distance (Y axis, in a.u.) and the kinetic energy E of the incident ion (X axis, in keV). The amplitude is color-coded.

It is obvious that the smaller the distance to the incident proton or H atom, the higher is the probability of a recombination event.

2.4.2 Resonant recombination

In case of resonant recombination, the incident ion is recombined with an electron which is tunneled to the metastable state [28], see Fig 2.7. The inverse process is also possible. An electron which is

in a metastable state with respect to the metallic ion can populate one of the free electron states of the metal only if it becomes free (the Pauli exclusion principle). The shift of the energy levels is due to the electric field.

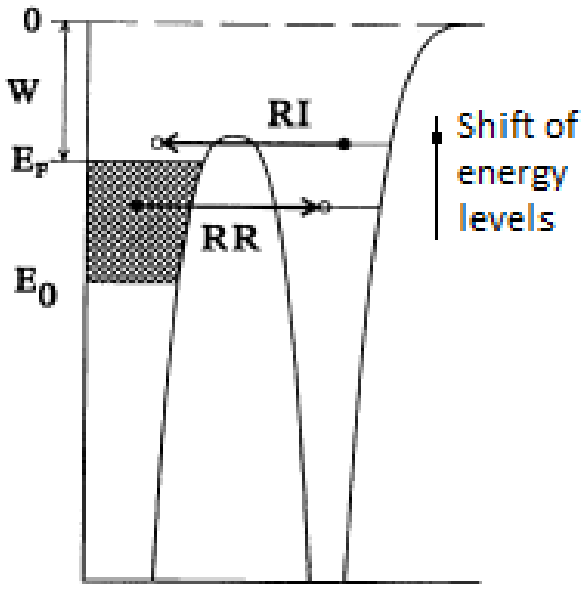

Figure 2.7: Energetic representation of resonant recombination. Electrons from the conduction band have energies between E_0 and the Fermi energy E_F. W is the work function, RR denotes the resonant recombination and RI inverse ionization process.

This effect comes from the crystal structure itself. The resonant processes are due to the potential seen by the moving ion i.e. they are described in a frame where the incident ion is at rest [43]. From the point of view of the ion, there appears a moving periodic potential which gives rise to transitions between bound states of the composite and free electron states [44]. The potential seen by the ion can be written as follows:

$$V(\mathbf{r},t) = \sum_{\mathbf{G}} V(\mathbf{G}) e^{i\mathbf{G}(\mathbf{r}\mp\mathbf{v}t)}, \tag{2.71}$$

here $\mathbf{G}$ is the reciprocal lattice vector [52], and $V(\mathbf{G})$ is assumed to be the Hartree potential created by all the charges of the crystal, the $\mp$ sign denotes that the periodic potential recedes $(+)$ from or approaches $(-)$ to the ion [43]. The idea of the Hartree approximation and potential is presented in Appendix A. By use of the Fourier transformation the Eq. 2.71 also could be written as [30]:

$$V(\mathbf{r},\omega) = 2\pi \sum_{\mathbf{G}} V(\mathbf{G}) e^{i\mathbf{G}\cdot\mathbf{r}} \delta(\omega \pm \mathbf{G}\cdot\mathbf{v}), \tag{2.72}$$

The potential $V(\mathbf{r},\omega)$ is seen by the ion as a frequency - dependent perturbation which contributes to the capture and loss processes. The perturbation induces transitions between the atomic bound state and the free-electron levels of the metal [30]. As in the Auger recombination process one has to consider a few corrections to get the formula of the probability per unit time of the process.

1. The probability per unit time is proportional to the square root of the *matrix element* $\langle f \mid \hat{A} \mid i\rangle$ of the process. Here the initial state of the system $|i\rangle$ is described by use of the $u_0(\boldsymbol{\rho})$

wavefunction. An electron bound to the incident ion is considered as the initial state. The valence electron state is described by an OPW wave function $|\mathbf{k}_{\rm OPW}\rangle$. In the rest frame of the ion, the momentum $\mathbf{k}_{\rm e}$ of the valence electron is given by $\mathbf{k}' - \mathbf{v}$, where $\mathbf{k}'$ is the momentum in the laboratory frame. First the correct form of the operator $\hat{A}$ is given by:

$$\begin{aligned} \langle u_0(\boldsymbol{\rho}) \mid 2\pi \sum_{\mathbf{G}} V(\mathbf{G}) e^{i\mathbf{G}\cdot\boldsymbol{\rho}} \delta(\omega + \mathbf{G}\cdot\mathbf{v}) \mid \mathbf{k}_{\rm OPW}\rangle \;\; &= \\ 2\pi \sum_{\mathbf{G}} \langle u_0(\boldsymbol{\rho}) \mid V(\mathbf{G}) e^{i\mathbf{G}\cdot\boldsymbol{\rho}} \mid \mathbf{k}_{\rm OPW}\rangle \; \delta(\omega + \mathbf{G}\cdot\mathbf{v}). & \end{aligned} \tag{2.73}$$

The probability per unit time of the process is proportional to the square root of the *matrix element*:

$$\Gamma_{\rm R}^{\rm L} \;\sim\; 2\pi \sum_{\mathbf{G}} \mid V(\mathbf{G}) \mid^2 \mid \langle u_0(\boldsymbol{\rho}) \mid e^{i\mathbf{G}\cdot\boldsymbol{\rho}} \mid \mathbf{k}_{\rm OPW}\rangle \mid^2 \delta(\omega + \mathbf{G}\cdot\mathbf{v}). \tag{2.74}$$

The matrix element describes the electron loss only.

2. The δ function in Eq. 2.74 has to be modified. The correction should take into account whether an electron is captured or ejected [39]:

$$\delta(\omega - \frac{1}{2}\mathbf{k}_{\rm e}^2 \mp \mathbf{G}\cdot\mathbf{v}). \tag{2.75}$$

Upper sign $(-)$ denotes the capture of an electron by the incident ion, while lower sign $(+)$ corresponds to the loss of an electron.

3. When an incident particle loses an electron, an electron-hole pair is created, thus $\mid \mathbf{k}_{\rm e} + \mathbf{v} \mid > k_{\rm F}$. On the other hand, when an incident particle captures an electron it lies inside the Fermi sphere, $\mid \mathbf{k}_{\rm e} + \mathbf{v} \mid \leq k_{\rm F}$. As in the Auger recombination process the step function $\Theta(x)$ is used:

$$\Theta(\pm k_{\rm F} \mp \mid \mathbf{k}_{\rm e} + \mathbf{v} \mid). \tag{2.76}$$

Upper signs $(+/-)$ denote capture of an electron by incident ion, while lower signs $(-/+)$ loss of the electron.

Collecting all these information together, the probability per unit time of the resonant recombination process is [30, 32, 39, 42, 43, 44]:

$$\begin{aligned} \Gamma_{\rm R}^{\rm C,L} \;\; = \;\; & 2\pi \int \frac{d^3k}{(2\pi)^3} \; \Theta(\pm k_{\rm F} \mp \mid \mathbf{k}_{\rm e} + \mathbf{v} \mid) \; \delta(\omega_0 - \frac{1}{2}\mathbf{k}_{\rm e}^2 \mp \mathbf{G}\cdot\mathbf{v}) \\ & \sum_{\mathbf{G}} \mid V(\mathbf{G}) \mid^2 \mid \langle u_0(\boldsymbol{\rho}) \mid e^{i\mathbf{G}\cdot\boldsymbol{\rho}} \mid \mathbf{k}_{\rm OPW}\rangle \mid^2 . \end{aligned} \tag{2.77}$$

The cross section of this process as well as a comparison with other recombination processes is presented in the Section 2.4.4.

2.4.3 Oppenheimer - Brinkman - Kramers (OBK) Process

The OBK process is a capture process, where an inner or outer shell electron of a target atom is transferred to the moving ion [43]. In the literature there are many physical approaches [53, 54, 55, 56, 57, 58, 59, 60, 61, 62, 63, 64]. Different results may be obtained depending on the approximation applied to the wave functions and the energy levels involved in the process [39].

This thesis presents one of them, the so-called *model-potential OBK* approximation (MPOBK), the $1s$-$1s$ capture. The transition electron caught by the incident proton is considered as the active electron. The other electrons are considered to be the passive ones [39]. In the OBK process the outer-shell electrons of the metal ions experience a strong Coulomb field of the incident ion. The electronic wave function of the electrons is distorted [65, 66]. For the inner-shell capture, the screening effect of the outer-shell electrons of the metallic ions reduces the capture probability of an active electron by the incident proton [65, 67, 68]. The geometry of the process is shown in the Fig. 2.8. Note that the vectors: $\mathbf{r}$, $\mathbf{r}_1$, $\mathbf{r}_2$ and $\mathbf{R}$ are parallel shifted. This is done to show clearly the position of each single vector.

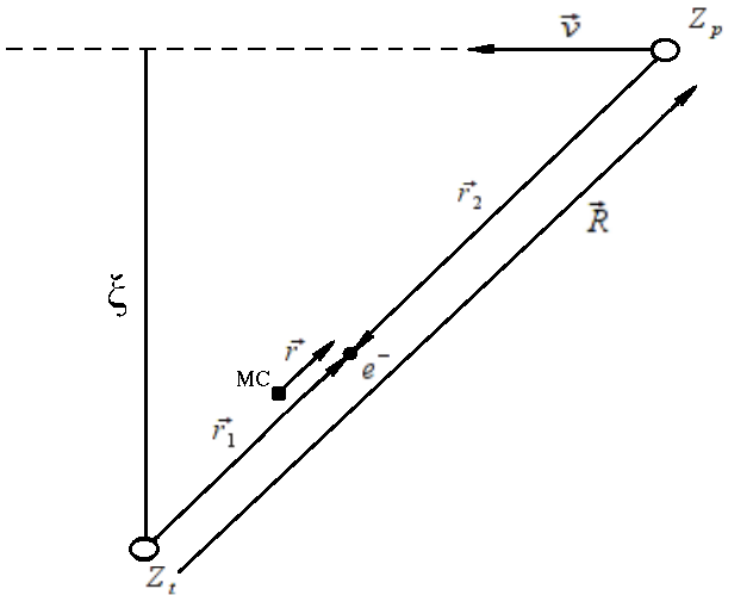

Figure 2.8: Z_p is the charge of the incident ion, Z_t is the charge of the target atom, ξ is the impact parameter, $\mathbf{v}$ is the velocity of the incident proton, $\mathbf{r}_1$ is the position of the active electron relative to the target atom and $\mathbf{r}_2$ is the position of the electron relative to the incident ion, $\mathbf{r}$ is the position vector of the electron relative to the mass center of the target atom and the incident ion, $\mathbf{R}$ is the position vector of the incident ion relative to the target atom, MC is the position of the center of mass.

The best choice of an effective potential, which is felt by the active electron, should be an experimentally found ionization potential [58]. For the multielectron targets it is a standard procedure to work with hydrogenic wave functions corresponding to an effective target charge [58]. The effective potential is given by:

$$V_\mathrm{S} = -\frac{1}{r_1} - \frac{(Z_\mathrm{t}-1)}{r_1}\exp(-Cr_1). \tag{2.78}$$

C is wavenumber tabulated specific for each element. The *model-potential* approximation neglects the core-core interaction. Atomic units are used again. In the initial state, the active electron is in the $1s$ orbital, the electronic wave function is:

$$\phi_{\mathrm{i}}(\mathbf{r}_1) = \pi^{-\frac{1}{2}}\alpha^{\frac{3}{2}}\exp(-\alpha\mathbf{r}_1), \tag{2.79}$$

where α is the variation parameter which, in fact, contains the screening effect of the passive electrons [65]. The Hamiltonian of the active electron is:

$$H = -\frac{1}{2}\boldsymbol{\nabla}^2 - \frac{1}{r_1} - \frac{(Z_{\mathrm{t}}-1)}{r_1}\exp(-Cr_1). \tag{2.80}$$

By use of the concept of the average energy $E(\alpha, C) = \langle\phi_{\mathrm{i}}(\mathbf{r}_1) \mid H \mid \phi_{\mathrm{i}}(\mathbf{r}_1)\rangle$ the experimental ionization potential I_{K} of the K shell is calculated. The detailed derivation is given in Appendix B. The potential is:

$$E(\alpha, C) = -I_{\mathrm{K}} = \frac{1}{2}\alpha^2 - \alpha - 4(Z_{\mathrm{t}}-1)\frac{\alpha^3}{(C+2\alpha)^2}. \tag{2.81}$$

The model can be compared with data which are available in the literature [69, 70]. In Fig. 2.9 the ionization energy of an electron in the *1s* state is shown as a function of atomic number Z of the target atom. For metals, e.g. Al(13) ($\pm$ 0.023 keV), Fe(26) ($\pm$ 0.028 keV) or Cu(29) ($\pm$ 0.045 keV), the here derived MPOBK result fit very well to the experimental data.

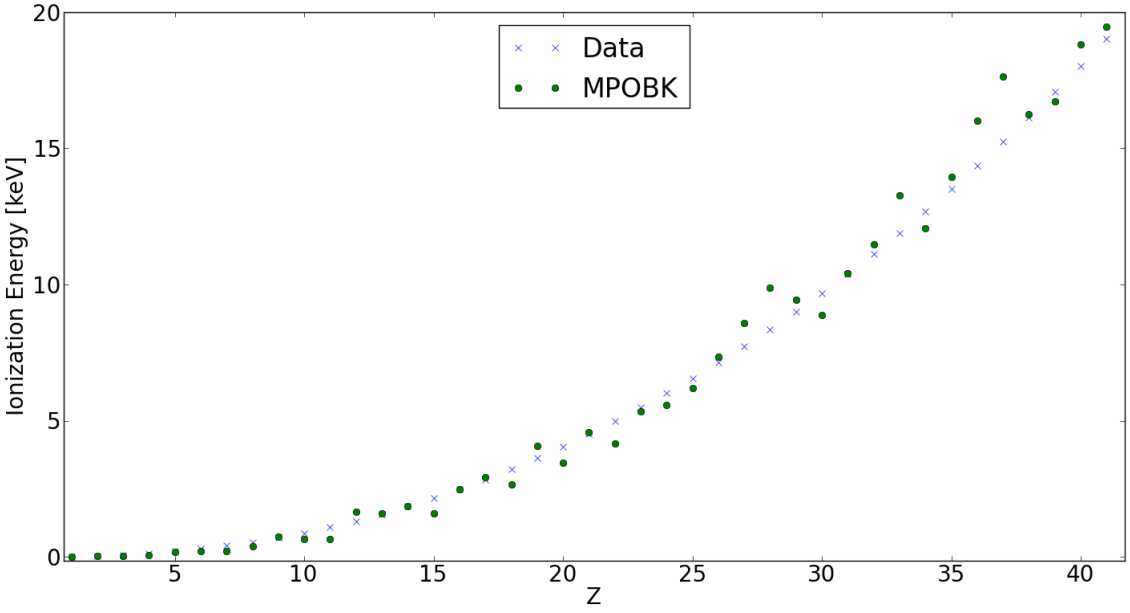

Figure 2.9: Measured (x) and calculated (o) ionization energies of electron in *1s* state as a function of target atomic number Z [69, 70].

The procedure to get the model values looks as follows: for each nucleus a pair α and C has to be found, so that the value of the Eq. 2.81 is comparable to the experimental one.

After the recombination, the electron is in the $1s$ orbital of the incident proton, the wave function of the electron then is:

$$\phi_{\mathrm{f}}(\mathbf{r}_2) = \pi^{-\frac{1}{2}} Z_{\mathrm{p}}^{\frac{3}{2}} \exp(-Z_{\mathrm{p}}\mathbf{r}_2). \tag{2.82}$$

After a transformation into the center of mass frame the initial and final state functions are:

$$\psi_{\mathrm{i}}(\mathbf{r}_1, t) = \phi_{\mathrm{i}}(\mathbf{r}_1) \exp\left(-ip\mathbf{v}\cdot\mathbf{r} - i\frac{1}{2}p^2v^2t\right), \tag{2.83}$$

$$\psi_{\mathrm{f}}(\mathbf{r}_2, t) = \phi_2(\mathbf{r}_2) \exp\left[i(1-p)\mathbf{v}\cdot\mathbf{r} - i\frac{1}{2}(1-p)^2v^2t\right]. \tag{2.84}$$

Here $\mathbf{r}$ is the position of the electron relative to the center of mass, $\mathbf{v}$ is the velocity vector of the incident ion in the laboratory frame, and $p = m_{\mathrm{p}}/(m_{\mathrm{p}} - m_{\mathrm{t}})$. It is assumed that the incident ion moves along the path with the impact parameter ξ [65]. The relation between the position vectors of the electron are: $\mathbf{r}_1 = \mathbf{r} + p\mathbf{R}$, $\mathbf{r}_2 = \mathbf{r} - (1-p)\mathbf{R}$, where $\mathbf{R}$ is the position vector of the incident ion to the target atom, $\mathbf{R} = \boldsymbol{\xi} + \mathbf{v}t$.

By use of the scattering amplitude A [65] which is related to the effective potential V_{S} (Eq. 2.78) the cross section of the process is calculated [58]:

$$A(b) = \frac{1}{i}\int_{-\infty}^{\infty} dt\ \langle\psi_{\mathrm{f}} \mid V_{\mathrm{s}} \mid \psi_{\mathrm{i}}\rangle, \tag{2.85}$$

$$\Sigma \sim \int_0^{\infty} db\ \mid A(b) \mid^2 b \sim v^{-12}. \tag{2.86}$$

The cross section depends strongly on the velocity of the incident proton. However, for too low kinetic energies of the incident proton the active electron at $1s$ state is screened by a cloud of electrons, and the incident proton has not enough energy to pass through a potential barrier. It is then neutralized by another recombination process, e.g. Auger recombination. Also when the kinetic energy of the incident proton is too high, the proton passes the electron cloud of the metal ion without a recombination event; the velocity of proton is so large that it has no time to catch an electron.

2.4.4 Summary

To compare all of the capture (Auger, resonant and OBK) and loss (Auger, resonant) processes a simple experiment can be performed. Protons with the initial energy of E_{p} are generated by a proton gun and shoot to a thin metallic foil. A detector which is located behind the foil collects the ions: H^+, H^- and neutral Hydrogen atoms H. To separate beams, the magnetic field $\mathbf{B}$ can be applied. The scheme of the experiment is shown in Fig. 2.10.

The selection of ions and neutral Hydrogen atoms is collected by the detector corresponding to the capture and loss processes that appear in the foil. The state of the charge fractions of the three components of the beam after penetrating the foil, negative ions (H^-) neutral atoms (H) and protons (H^+), can be described in terms of electron -capture an -loss rates Γ (probabilities per unit time) [32]. The fractions are given by [32]:

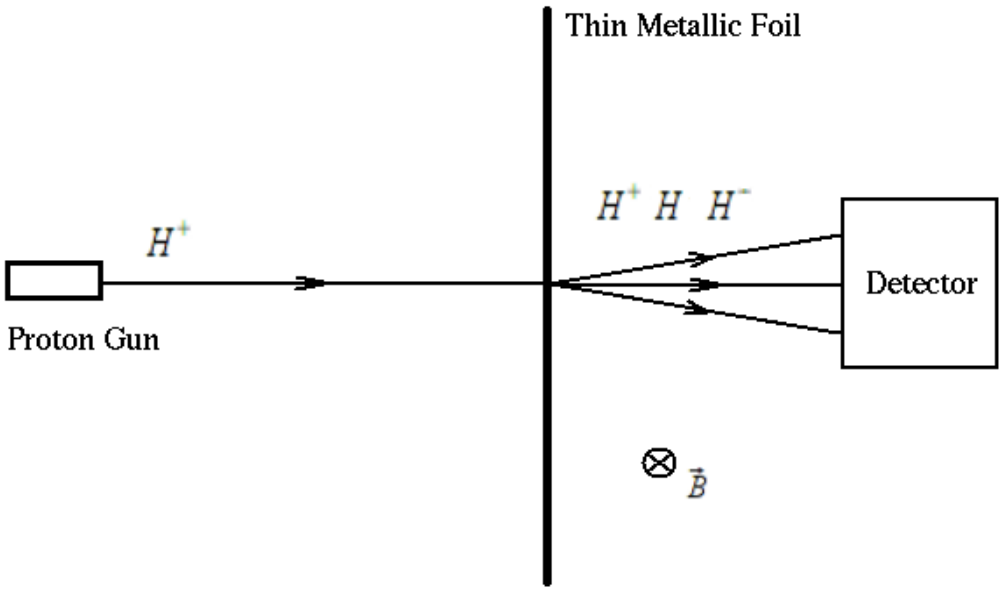

Figure 2.10: Thin metallic foil is irradiated by protons. Capture and loss processes take place inside the foil. Ions and neutral Hydrogen atoms are registered by the detector. Beams are deflected by the magnetic field **B**.

$$\begin{aligned} \phi^+ &= \Gamma^{\mathrm{L}}(H)\Gamma^{\mathrm{L}}(H^-)D^{-1}, \\ \phi^0 &= \Gamma^{\mathrm{L}}(H^-)\Gamma^{\mathrm{C}}(H^+)D^{-1}, \\ \phi^- &= \Gamma^{\mathrm{C}}(H^+)\Gamma^{\mathrm{C}}(H^0)D^{-1}, \end{aligned} \tag{2.87}$$

where:

$$D = \Gamma^{\mathrm{L}}(H)\Gamma^{\mathrm{L}}(H^-) + \Gamma^{\mathrm{L}}(H^-)\Gamma^{\mathrm{C}}(H^+) + \Gamma^{\mathrm{C}}(H^+)\Gamma^{\mathrm{C}}(H). \tag{2.88}$$

The dynamics of capturing and loosing electrons during the incident proton penetrate of foil is described in terms of rates $\Gamma^{\mathrm{L,C}}$. Here $\Gamma^{\mathrm{L}}(H)$ and $\Gamma^{\mathrm{L}}(H^-)$ are the probabilities per unit time for the first and second electron loss, while $\Gamma^{\mathrm{C}}(H^+)$ and $\Gamma^{\mathrm{C}}(H)$ are the probabilities per unit time for the first and second electron capture, respectively [32].

Now, by use of Eqs. 2.31 and 2.87, theory and experiment can be compared: left hand side of the set of Eq. 2.87 comes from experiment, while right hand side from theoretical models. From experiments the fractions of protons, neutral Hydrogen atoms, and negative ions are obtained. Then by use of Eq. 2.87 the corresponding rates are calculated. Having the rates and knowing the velocity of incident protons the corresponding cross sections can be calculated form Eq. 2.31.

Two plots in the Fig. 2.11 show the different cross sections both for capture and loss when Aluminum is irradiated with protons H^+/Al as a function of proton kinetic energy given in keV [30]. One can see that for a capture of an electron (upper plot) the Auger process Σ_{A} is a dominant one. The resonant process has negligible contribution to the total cross section. The OBK process (in the

literature it is often called the "shell process") gives the main contribution to the total cross section beyond 128 keV, depending on the material used as a target [31].

There is also one capture process which was not described in the thesis, it is called the Radiative Electron Capture (REC). For Aluminum it predicts to be the dominant cross section above a proton energy of ~ 300 MeV and e.g. for Mylar above ~ 125 MeV [31]. In this energy range a flux of solar protons at ~ 1 AU is very small.

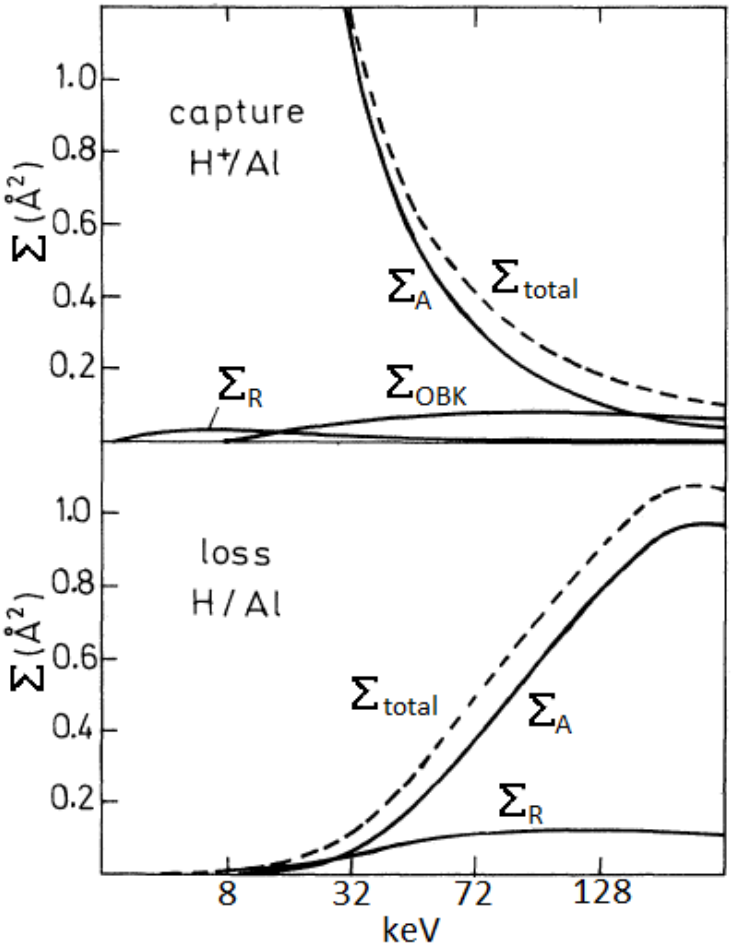

Figure 2.11: Top plot: cross sections for capture processes of H^+ ion (Auger (Σ_A), resonant (Σ_R) and OBK process (Σ_{OBK})). Lower plot: cross sections for loss processes of Hydrogen atom. The dashed line represents the total cross section Σ_{total} of all processes.

The theory presented in the previous subsections was tested by many scientific groups e.g. [31, 32, 39, 42, 43, 44]. Experimental facts clearly show that considered capture and loss processes adequately describe the nature of charge fluctuation phenomena which appear inside bombarded material. For majority of the solar protons for which the kinetic energy is lower than 100 keV, the Auger process leads the recombination. The maximum contribution of the OBK capture process to the total cross section is located in a kinetic energy range exceeding 150 keV, where solar proton flux is already much smaller than below 100 keV.

Chapter 3

The Complex Irradiation Facility

I have published the here presented technical description of the Complex Irradiation Facility in a review scientific journal named *Journal of Materials Science and Engineering A* [13].

The Complex Irradiation Facility (CIF) was designed and commissioned with the aim to perform material investigations under radiation conditions as prevalent in space environment. The idea is to combine multiple radiation sources at a vacuum irradiation chamber. A driving motivation to establish the CIF at the DLR Institute of Space Systems was its participation in the DLR-ESA GOSSAMER solar sail project [11]. However, the CIF can be used for a large variety of material studies. Besides of thin metallic foils, also thin sections of meteorites or organic substances can be exposed to a well-defined irradiation with protons, electrons, and electromagnetic waves. A great effort has been expended to simulate the conditions prevalent in the interplanetary space as realistic as possible. It concerns especially the dimensioning of the electron and proton accelerator with respect to energy and intensity range. Both cover the bulk of the corresponding solar wind parameters. It concerns as well the quality of the vacuum which can be achieved in the CIF. To attain a high vacuum special effort was made. The quality of the vacuum is an important aspect to detect material degradation because molecules of the rest gas can interact with the radiation and degrade the surface of the sample. This would distort the results of degradation studies which are actually designed for conditions of the interplanetary space. Therefore the complete facility has been manufactured in UHV-technology with metal sealings and without organic compounds (rubber vacuum sealings, pump oil) to avoid self-contamination which could affect the results of the experiment.

It is known from many evaluation tests [1, 2] that particle and UV radiation can significantly degrade materials and, e.g., lead to changes in their mechanical behavior or thermo-optical properties [71]. That was taken into account for the determination of the required parameters of the CIF.

An important number that characterizes the performance of the CIF is the acceleration factor. It is defined as the ratio of the intensity of the degrading radiation applied to a material during a laboratory test to the intensity of the same degrading parameter in space environment [2]. The spectra of the light sources are shown in comparison to the extraterrestrial solar spectrum [72, 73] in Sections 3.3 and 3.4.1. The spectral distribution of the accelerating factor of the complete electromagnetic radiation provided by all light sources is presented in the Conclusion 3.5.

Another aspect, beside the irradiation performance, is the measurement engineering to detect the changes of material properties caused by irradiation. For this purpose the CIF is equipped with a mass spectrometer at the irradiation chamber to qualify the outgassing behavior of the sample. Furthermore, our department has commissioned an optical measurement system, consisting of a FTIR spectrometer and Ulbricht spheres. It captures the changes of thermo-optical properties by measuring reflectivity and emissivity. This can be done presently only ex-situ, i.e. the sample has

to leave the vacuum and the influence of the atmosphere cannot be avoided. Another possibility to qualify optical properties is the measurement of the light pressure [74] before and after an irradiation test. Light pressure measurements return a kind of integral information about the state of degradation of irradiated metallic foils. Such a light pressure measurement facility will be placed outside the CIF.

In order to study the effects of degradation on to the elastic properties of the degraded materials, a tensile testing facility will be established at the CIF. Clearly, such studies can be performed only ex-situ.

The experimental studies of degradation effects have to be accompanied by theoretical efforts. This is necessary not only to get an idea about the physical processes that cause degradation. It is also necessary for profound predictions of changes in the material properties on long-term space missions, where a simple scaling by use of the acceleration factors provided by the CIF will fail, see Section 4.

3.1 Configuration of the system

3.1.1 Geometry and technical parameters

The CIF consists of a vacuum irradiation chamber (400mm in diameter) which is connected to a lock chamber for the placement of the sample into the vacuum environment of the facility (see Fig. 3.1). The irradiation chamber has got four tubes with flanges for the connection with the radiation sources. They are arranged at an angle of 30 degrees to the neighboring one in the same level for the accelerator beam line, the solar simulator, and the argon-VUV-source. The deuterium-UV-source is located above the solar simulator at an angle of 30 degrees between their axes. The axes of all radiation sources are crossing in the center of the irradiation chamber where the target station is mounted. The geometry of that arrangement, the target mounting, and the radiation sources itself are dimensioned in a way, that a square area of 80mm can be irradiated simultaneously with all sources.

The sample mounted in a holder will be inserted into the lock chamber and transferred after vacuuming by a magnetic manipulator into the sample station of the irradiation chamber. Additionally, there are magnetic manipulators installed in cross direction at the lock chamber. They can bring the sample holder in front of the Ulbricht spheres of the planned in-situ measurement system to measure the reflectivity before and after the irradiation without leaving the vacuum environment.

The vacuum system at the irradiation- and the lock chamber consists of a turbo molecular pump, an ion getter pump and a cryogenic pump to reach a pressure in the UHV-range. This will allow measurements with the quadrupole mass spectrometer which is installed at the irradiation chamber.

3.1.2 Target mounting

The target mounting (see Fig. 3.2) can be rotated about 30° into two directions. Thereby, either the VUV-radiation or the particle beam line can be perpendicularly oriented with respect to the sample surface. In the normal transfer position the sample surface is oriented perpendicular to the axis of the solar simulator.

The sample station is vertically adjustable, so that the sample holder can be inserted at the upper or the lower position at the station. The upper position provides a heating compartment from the backside of the sample. This can be used e.g. to simulate ambient conditions closer to the Sun, which

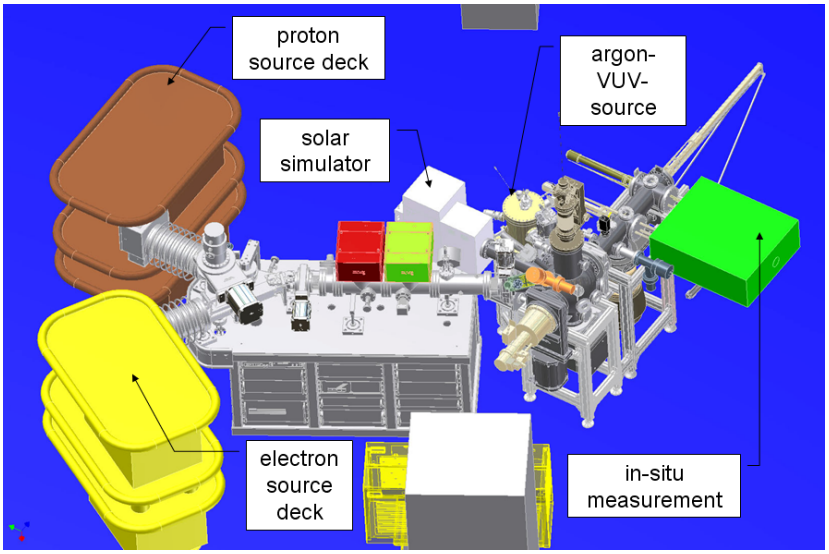

Figure 3.1: The CIF, electron and proton source deck is located on the left, solar simulator is in the center of the snap, argon-VUV-source is located behind the chamber and the in-situ measurement on the right side of the chamber.

Table 3.1: Technical parameters of the CIF.

vacuum test chamber	
volume	ca. 33.5 l (diameter: 400 mm)
irradiated target area	80 mm in diameter
vacuum pressure	up to 10^{-10} mbar in the empty chamber
thermal conditioning of the targets	
heating	halogen spotlights (600 W, max. 450°C)
cooling	liquid nitrogen (IN_2: 80 K)
proton / electron dual beam	
energy range	1 - 10 keV, 10 - 100 keV
current range	1 - 100 nA, 0.1 - 100 μA
light sources	
solar simulator	250 - 2500 nm (5000 Wm^{-2})
deuterium-UV-source	112 - 410 nm (1.65 Wm^{-2})
argon-VUV-simulator	40 - 410 nm (50 mWm^{-2})
measurement instrumentation	
ex-situ-measurements	solar absorption, emissivity and reflectance
quadrupole mass spectrometer	range: $0 - 512$ amu
sensors	radiation, temperature and pressure

cannot be supplied by the solar simulator. Furthermore the sample can be cooled to liquid nitrogen level to simulate ambient conditions of the deep space.

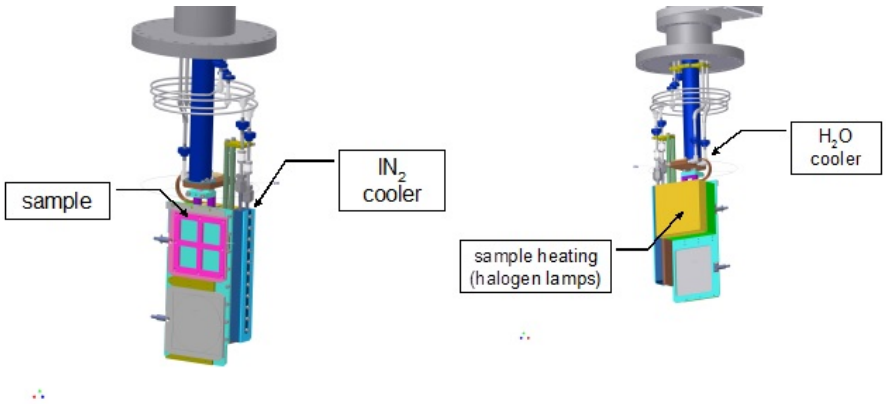

Figure 3.2: Sample station in the center of the irradiation chamber (front and back side).

3.2 The 100 keV Proton / Electron dual beam irradiation system

The Dual Beam Irradiation System is designed to irradiate samples with protons or electrons independently or with both particle species simultaneously. The selected beam(s) can be scanned over the samples. All relevant parameters can be adjusted remotely via the computer control system. Figure 3.3 illustrates the configuration of the beam line with its main items in view from top.

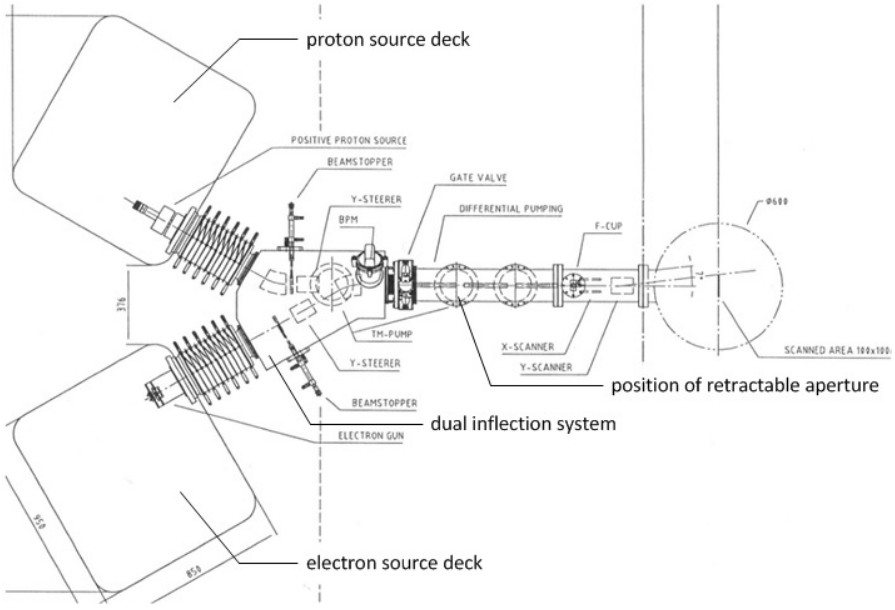

Figure 3.3: Layout of the dual beam irradiation system.

The vacuum system of the beam line consists of the acceleration tubes (one for each particle species), the dual inflection system, and the differential pumping segment. The dual inflection system is equipped with a turbomolecular pump and the differential pumping segment with two ion getter pumps.

The protons are produced by ionization of Hydrogen, which is stored in a lecture bottle inside the source deck. After pressure reducing the Hydrogen is guided through a thermo-mechanical gas inlet valve with remote control to the ion source. The ionization takes place inside the glass bulb of the source by excitation with a radio frequency, which is capacitive coupled to the bulb. The plasma is confined and positioned by an axial permanent magnetic field. The source output is optimized by control of the source gas pressure and oscillator loading. There are not only positive ions H^+ (1 atomic mass unit) generated with Hydrogen gas, but also the molecule ions H_2^+ (2 atomic mass units) and H_3^+ (3 atomic mass units). This makes a mass selector necessary, which is installed in the dual inflection system.

The electrons are generated by a lanthanum hexaboride (LaB_6) cathode, which is a high performance, resistively heated, thermionic electron source. A heater current and Wehnelt voltage control the electron current.

Both particle species are accelerated in appropriate tubes by a high voltage, which corresponds to the required energy. The acceleration tubes are manufactured as a metal to ceramic brazed assembly with no organic compounds. After the acceleration the beam(s) are deflected onto a common axis in the dual inflection system. This is realized by inflection magnets. The proton inflection magnet works additionally as a mass selector for the different ion species (elemental and molecular Hydrogen ions). The electron beam is magnetically shielded from the comparatively strong magnetic fields that are applied in the proton inflection line. Both the vertical and the horizontal position of each beam are adjusted by separate magnetic steerer, which are used to compensate the influence of the electron inflection magnet to the proton beam too. The negative influence of the magnetic components of the proton beam and/or the Earth magnetic field to the electron beam is corrected with special magnetic shielding techniques, compensating magnetic fields by correction coils and advanced software tools. A separate beam stopper for each particle species can be inserted pneumatically to block the beam while the other source is running. This is useful to tune each source separately.

The Beam Profile Monitor (BPM), see Fig. 3.3, is used to analyze the horizontal and vertical beam size and position as well as its intensity distribution separately for each particle species. For that purpose, either the proton or the electron beam has to be blocked. The BPM is located behind the inflection segment at the beam line.

A retractable aperture can be inserted pneumatically into the beam at the differential pumping segment. It is used to reduce the current. If the current is adjusted it can be measured with the retractable Faraday cup (F-cup, see Fig. 3.3). It can be inserted pneumatically in front of the scanning section. This must be done separately for each particle species, i.e. again one beam must be blocked.

The electrostatic scanning segment contains two sets of deflection plates, which deflect the beam in two directions perpendicular to each other. The triangular voltages for these plates and its crystal locked frequencies are carefully chosen to eliminate the possibility of synchronization caused dose non-uniformity. The amplitude of the deflection voltages is adjusted by use of the Faraday cups, which are mounted at the corners of the sample station. They detect if the sample area is scanned completely.

3.3 The solar simulator and the deuterium-UV source

The solar simulator is used to simulate the electromagnetic spectrum of the Sun in the wavelength range from 250 nm to 2500 nm. It consists of a Xenon lamp with 1600 W electrical power, an optical mirror and lens system to concentrate and homogenize the light spot. An air mass zero filter is

mounted to eliminate the Xenon peaks and to fit the spectral distribution to the extraterrestrial one defined in the ASTM E-490 [72]. Figure 3.4 illustrates the spectral irradiance of the solar simulator as measured at DLR-Berlin with the minimum, and the maximum settings of electrical power.

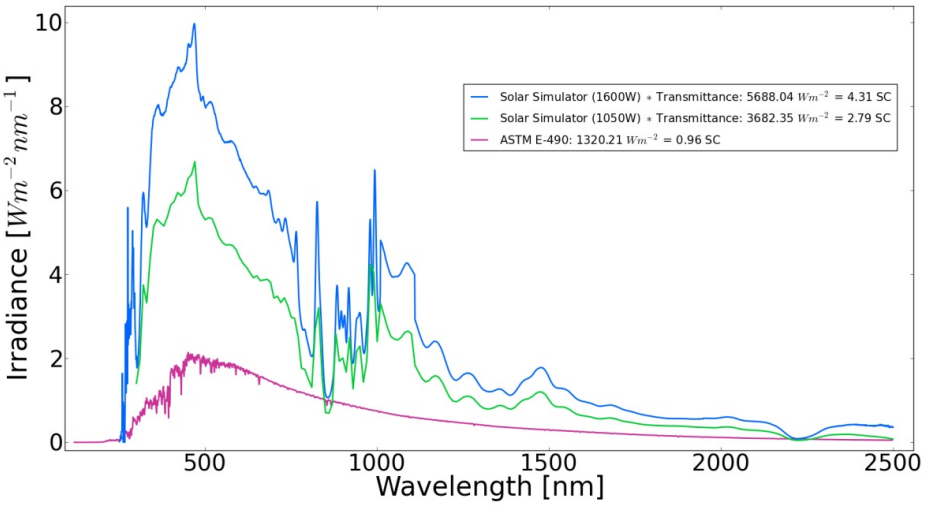

Figure 3.4: Spectral irradiance of the solar simulator with the minimum and maximum setting of electrical power in comparison to ASTM E-490 standard [72].

The measured values are corrected with the transmittance of the quartz glass window at the irradiation chamber. Presently there are ongoing activities to enhance the intensity in the UV range below 250 nm (see Section 3.5).

The deuterium-UV-source is a modified standard solution which is intended to be used as an excitation source in research and development. The modifications are the MgF_2-window that allows a transmission down to 112 nm, and an indium sealing between window and vacuum flange to avoid contamination.

The working principle of the source is the electrode excited gas discharge. The construction consists of a glass bulb, which is filled with deuterium, a cooling water jacket, and a vacuum flange (DN40CF). The electrical leads from the socket of the housing to the interior of the bulb are melt-sealed and vacuum tight. The glass bulb contains the thermionic cathode, which is heated by means of direct or alternating current, the ring-shaped anode, and an aperture of 1 mm diameter, where the discharge arc between cathode and anode is guided through. The light intensity can be controlled by the anode current between 0.8 A and 1.9 A. That corresponds to 120 W and 200 W electric power. The spectral irradiance, both at minimum and maximum setting, was calibrated by Physikalisch Technische Bundesanstalt (PTB) in Berlin (see Fig. 3.5).

The stability of the source can be observed by shifting a monitoring sensor, mounted on a linear manipulator, onto the axis between source and sample.

3.4 Design and performance of Vacuum-UV simulator

The section describes the construction and performance of a VUV-simulator that has been designed to study degradation of materials under space conditions. It is part of the CIF. Presently available

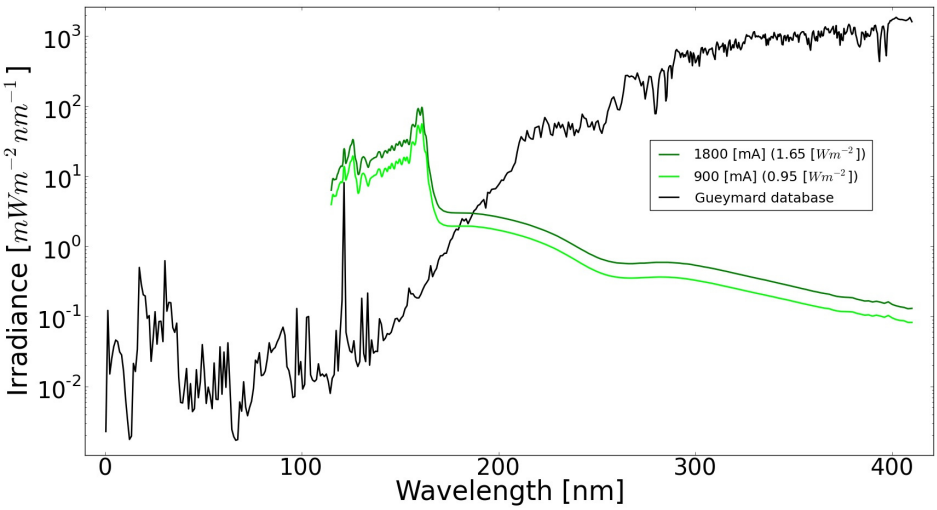

Figure 3.5: Spectral irradiance of the deuterium UV source with the minimum and maximum setting of electric power in comparison to Gueymard database [73].

UV-sources used for material tests do not allow the irradiation with wavelengths smaller than about 115 nm where common Deuterium lamps show an intensive cut-off. The VUV-simulator generates radiation by excitation of a gas-flow with an electron beam. The intensity of the radiation can be varied by manipulating the gas-flow and/or the electron beam.

The VUV simulator has been calibrated at three different gas-flow settings in the range from 40 nm to 410 nm. I took part in the calibration procedure of the VUV-source at PTB in Berlin. After the calibration PTB provides raw data which I have worked to get the source spectra. I made the spectra line identification by use of the NIST database [14]. I compared also the VUV emission lines with the solar ones. For this purpose I have used the SUMER database [15]. Then I have used the spectra to calculate the acceleration factors as well as stability of the source, i.e. maximum deviation of the light intensity as a function of wavelength range. My calculations together with description of the calibration procedure have been published in a review scientific journal *Advances in Space Research* [16]. The measured spectra show total irradiance intensities from 24 to 58 mWm^{-2} (see Table 3.3) in the VUV-range, i.e. for wavelengths smaller than 200 nm. They exhibit a large number of spectral lines generated either by the gas-flow constituents or by metal atoms in the residual gas which come from metals used in the source construction. In the range from 40 nm to 120 nm where Deuterium lamps are not usable, acceleration factors of 3 to 26.3 Solar Constants are reached depending on the gas-flow setting. The VUV-simulator allows studies of general degradation effects caused by photoionization and photodissociation as well as accelerated degradation tests by use of intensities that are significantly higher compared to that of the Sun at 1 AU.

The solar UV radiation is generally defined as the solar radiation with wavelengths from 10 nm to 400 nm [1]. The range between 200 nm and 400 nm is named Near-UV (NUV) range. The other part of the solar UV radiation from 10 nm to 200 nm is denoted as the Vacuum-UV (VUV) range. Extraterrestrial intensity spectra of both ranges show that the contribution of the VUV radiation to the total intensity of solar UV irradiation is almost negligible (Fig. 3.6). The VUV-irradiation amounts to only 0.1% of the NUV irradiation intensity. However, the VUV radiation can noticeably contribute to the degradation of materials despite of its small amount of total intensity. The energy

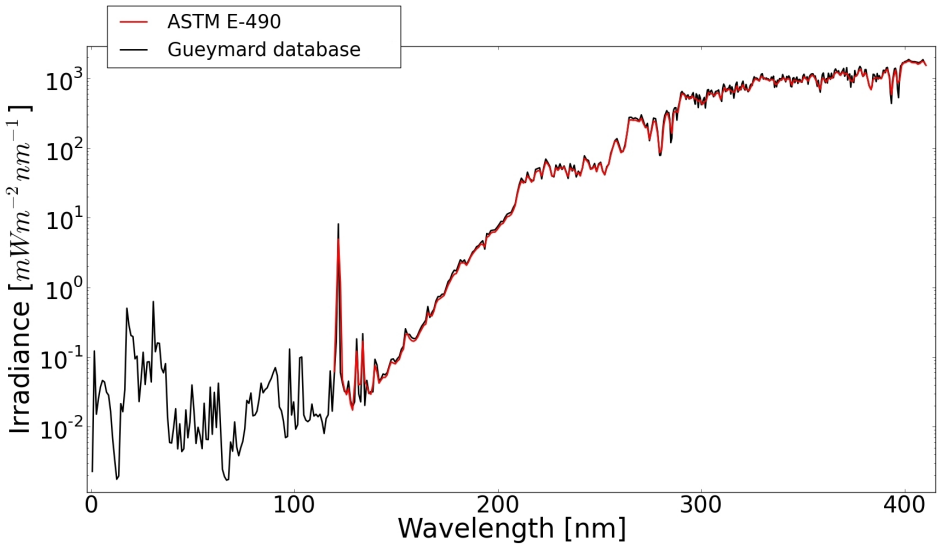

Figure 3.6: Extraterrestrial spectral solar UV-irradiance at 1 AU (astronomic unit). The red line shows data from ASTM E-490 [72]. This standard provides data only down to 119.5 nm. The black line exhibits spectral data from Gueymard [73]. This data are representative for average solar activity conditions. They are in very good accordance to the ASTM E-490 spectrum between 120 nm and 400 nm.

of a single photon in the VUV range is considerably higher compared to a photon in the NUV range. VUV-photon energies vary from 6 eV to 124 eV whereas NUV-photon energies range only from 3 eV to 6 eV. Therefore, VUV radiation can generate photoionization and photodissociation effects that cannot be caused by the significantly lower photon energies in the NUV range. Thus, degradation effects that would not occur under NUV irradiation even at very high intensities may be expected if the material is exposed to VUV irradiation for longer periods of time.

To get the most reliable information on UV degradation of materials in space by ground material tests, the UV-spectrum of the Sun should be simulated as close as possible. The NUV spectral region can be simulated by using commercial short arc Xenon lamps [75]. The VUV spectral range is simulated with Deuterium lamps in almost all material tests [76]. These lamps, however, feature a lower wavelength cut-off at approx. 115 nm due to internal MgF_2- or LiF_2-windows which exhibit a strong decrease in transmission at this wavelength. This leads to the fact that the residual VUV wavelength range between 10 nm and 115 nm is generally not covered in up-to-date material tests although especially this range shows a strong increase of photon energies from 10 eV to 124 eV.

The lack in the VUV simulation of the solar spectrum by currently available radiation sources necessitated the construction of a VUV simulator that covers the range from 10 nm to at least 115 nm. Beside a good approximation to the real solar spectrum this simulator has to achieve several other requirements to make it useful for material testing: It has to exceed the radiation intensity of the Sun (at 1 AU) at the sample area of the CIF in order to accelerate the degradation of the tested materials and to allow the simulation of long-term effects. Furthermore, the simulator has to generate radiation that is emitted under a relatively large solid angle into the test chamber to permit the simultaneous irradiation of several samples with a homogeneous intensity distribution. It must, moreover, be capable of working continuously during a sufficiently long period of time. The construction must take into account that the VUV simulator has to be connected to the test chamber

without any window as no window material is known that completely transmits radiation in the concerned spectral range. Therefore, the design has to ensure that no significant amount of particles of the medium necessary to generate the radiation can migrate inside the test chamber.

Below it is described in detail the design and performance of a VUV simulator that has been built with regard to the given requirements above. It bases on a design of a VUV gas-jet simulator that was constructed 15 years ago by the Institute of Low Temperature Physics and Engineering in Kharkov, Ukraine, in collaboration with the DLR [77]. The calibration of the VUV simulator has been carried out in the range from 40 nm to 410 nm by the Physikalisch Technische Bundesanstalt (PTB) in Berlin, Germany. The calibration method and procedure is briefly explained in Section 3.4.2. The spectral distribution of radiation as well as the irradiance, the derived acceleration factors as well as the stability of the source are discussed and summarized in the next sections.

3.4.1 Design and principle of operation of the VUV-Source

The design of the VUV simulator is based on the semi-cryogenic version of the previous simulators which are described in [77]. The radiation is produced by the transition of electrons belonging to excited gas atoms into their ground state. The gas atoms are excited by electron bombardment of a spatially limited supersonic gas jet which flows into a vacuum chamber. The vacuum is maintained by a combination of cryogenic and mechanical pumps (semi-cryogenic design). A pressure of about 1 mbar inside the jet is sufficient for an effective excitation. Beyond the jet close to its boundary the gas pressure is several orders less (10^{-4} mbar) caused by the supersonic directional motion of the jet. This is the premise to locate an electron source in the close vicinity of the gas jet. This method generates electromagnetic radiation in a broad spectral range (soft X-rays, VUV, NUV) with relatively high intensities at lower wavelengths (< 115 nm) and permits a design without windows, which would disable the transmission in this range. The spectral intensity distribution of the radiation depends on the gas mixture, the flow rate of the jet, the electron current (on the alignment between beam and jet, and the focus of the electron beam).

Fig. 3.7 illustrates the arrangement of the electron source and the gas jet inside the vacuum chamber of the simulator. The outlet of the generated VUV-light is realized behind the spot perpendicular to the figure's plane. The electrons which pass through the gas jet are caught by the collector at the opposite side of the source. The components of the vacuum system are better visible in Fig. 3.8, whose plane is perpendicular to the plane of Fig. 3.7.

The gas jet is injected by a nozzle from top of the VUV-chamber into the vacuum. The flow rate is stabilized by a flow controller and is adjustable by software in the range between 0 and 5000 sccm (standard cubic centimeter per minute). The bulk of the gas load is pumped out through an intake port at the bottom of the chamber by a screw pump. The rest, which is a small fraction of about 3% is removed by cryogenic condensation at two baffles. Each of them is connected to one of the both stages of the cold head of a commercial cryogenic pump (Helium cooling machine). The 2^{nd} stage reaches a bottom temperature of 15 K without gas load. It increases to about 20 K under gas load by formation of ice, which decreases the pumping power gradually and limits the operating time. The temperature is logged permanently as an indicator when a regeneration is necessary to remove the ice. During this process the cryogenic pump is turned off while the mechanical pumps continue their operation. The temperature inside the chamber increases and the residual gas, which is frozen on the cold baffles, is pumped out. The gas nozzle is thermally connected to a water circuit for tempering it to avoid a freeze. The combination of both pumping procedures is possible due to the effect that the gas inside the intake port banks itself. Thereby, a reverse flow from the pipeline is impeded and the pressure regions are separated by 10^{-4} mbar around the gas jet (inside the chamber) and more

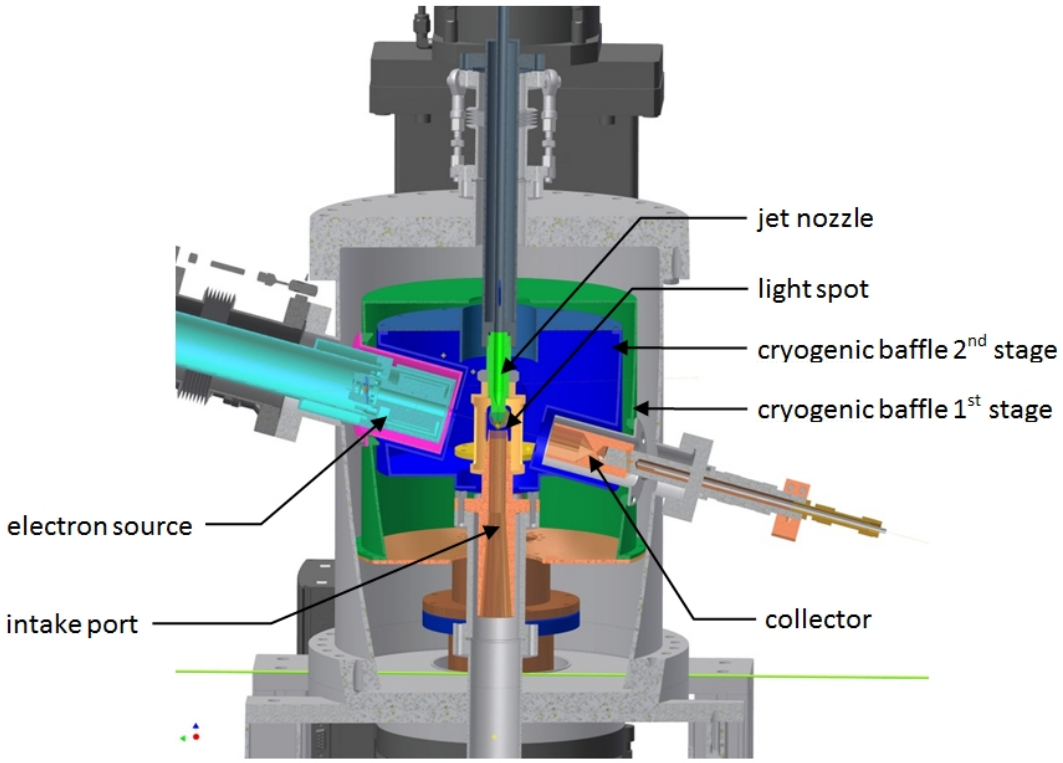

Figure 3.7: Sectioning of the VUV-simulator along the electron beam.

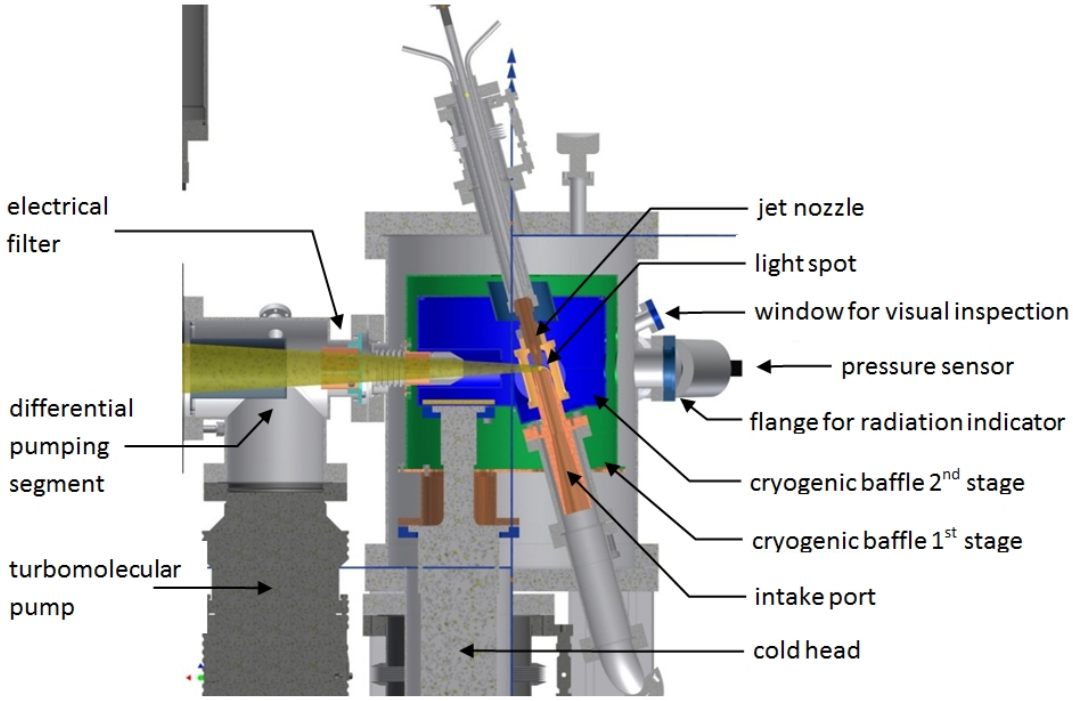

Figure 3.8: Sectioning of the VUV-simulator along the light outlet (yellow).

than 10^{-2} mbar inside the pipeline.

A differential pumping segment is installed at the light outlet consisting of a turbomolecular pump and an aperture assembly. It improves the pressure conditions inside the radiation chamber and reduces the metal traces to the lowest possible limit. Since tests can be performed in the chamber at pressures of 10^{-6} mbar and less the pollution by metals over the test period is expected to be negligible. The fraction of light which is permitted to the test chamber is colored yellow in Fig. 3.8. An opening angle of about 6° is defined by the apertures in the cryogenic baffles and at the differential pumping segment. It ensures the irradiation of a target area with a diameter of 80 mm at a distance of about 770 mm from the spot, as it is realized in CIF. To avoid that charged particles produced at the spot can reach the irradiated object, an electric filter is installed at the light outlet, which deflects them beyond the radiation flow.

The axes of the gas jet, the electron beam and the light outlet are arranged out of square, while the orientation of the light outlet is horizontal. The axis of the gas jet is turned by 15° to the vertical axis in the direction of the light outlet. The electron beam is inclined by 15° to the horizontal axis but in its vertical plane it is perpendicular to the light outlet. The idea of this design is that the probability that particles could reach the radiation chamber or damage the cathode of the electron source is less than for a perpendicular arrangement.

The electron source is realized as a Pierce-type model with a magnetic lens behind the anode. The LaB_6-cathode is heated up electrically by adjusting the cathode voltage depending on which emission current is needed. The electronic control unit of the source provides a PID algorithm which stabilizes the emission current by varying the Wehnelt voltage automatically. The beam is focused by setting the current for the magnetic lens.

Two flanges are located at the opposite side of the light outlet. Each is connected with a window for visual inspection of the luminous jet and with a radiation indicator compartment (see Fig. 3.8). The indicator measures the signal of the source. The digital value of the signal is visualized by the controlling software to monitor the stability of the radiation. During the calibration procedure for every measured spectrum the corresponding sensor value has been determined.

Fig. 3.9 illustrates the size and intensity of the spot qualitatively with different settings for the emission current and for the gas flow. The photos were taken through the window at the opposite side of the light outlet (see Fig. 3.8).

Based on the experience of the first design of the VUV simulator [77], the same gas mixture has been chosen to produce the spectra. The mixture provides a continuum spectrum similar to the Sun's spectrum. Due to the presence of the water particles in the chamber the Hydrogen Lyman α as well as the other H lines are present (see Figs. 3.11 and 3.12). The intensity of the VUV light increases generally up to a saturation value with increasing gas flow. An increasing gas flow, however, reduces the quality of the vacuum in the radiation chamber. Thus, the sensitive balance between VUV light intensity and vacuum quality has to be taken into account when optimizing the VUV source parameters. In the same way, a larger emission current causes, for a given gas flow, a higher intensity of the radiation. Therefore it is favorable to operate the simulator with relatively small gas flows and high electron currents to get the same intensity.

After first function tests concerning the stability and operating life, the following settings were chosen for the calibration procedure:

- Gas mixture: Ar (98.5%), Kr (1%) and He (0.5%)
- Electron energy: 1 keV,
- Electron emission current: 20 mA,

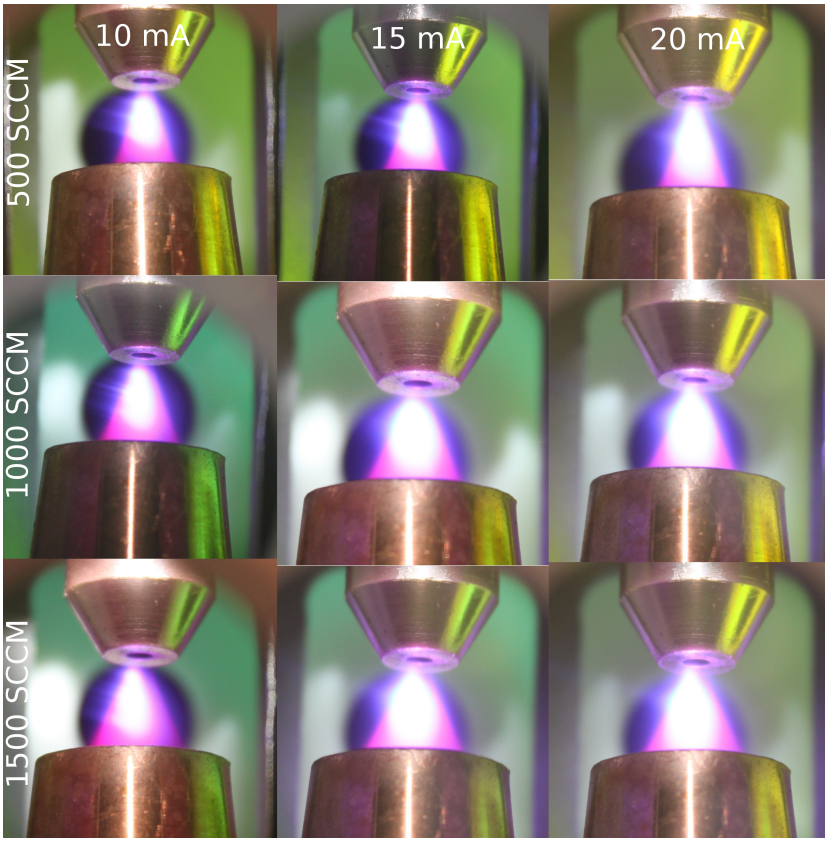

Figure 3.9: Pictures of the VUV-spot with different settings of the gas flow rate (rows: 500, 1000 and 1500 sccm) and the emission current (columns: 10, 15 and 20 mA).

- Flow rate of the gas jet: 300, 600, 1200 sccm.

The goals for the calibration procedure were:

1. Finding the optimal alignment between electron beam and gas jet,
2. Finding the magnetic lens current for an optimal focus of the electron beam,
3. Measurement of the spectral radiant intensity of the radiation.

3.4.2 The method and procedure of calibration

The VUV source was calibrated in the radiometry laboratory of the Physikalisch-Technische Bundesanstalt (PTB) at Berlin Electron Storage Ring for Synchrotron Radiation of Helmholtz Zentrum Berlin (BESSY II) in Berlin-Adlershof. PTB provides the calibration of radiation detectors and sources as well as the characterization of optical components in the UV and VUV range [78, 79].

Fig. 3.10 shows the normal-incidence monochromator (1m, 15° McPherson type) beam line for source calibration in the configuration for the calibration of the measurement site, where synchrotron radiation is used as a primary source standard.

The whole device can be rotated around the entrance axis to take the polarization of synchrotron radiation into account during that procedure. Moreover, it is possible to shift the monochromator

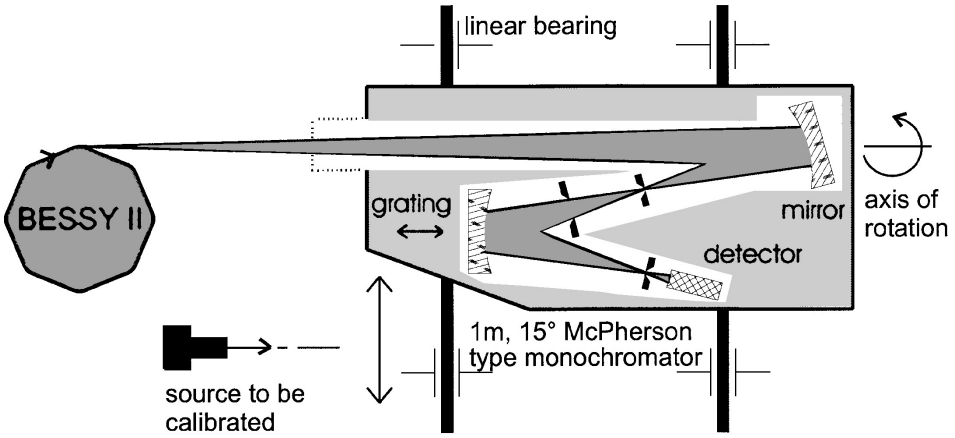

Figure 3.10: The normal - incidence monochromator beam line used for calibration of radiation sources [78].

compartment via linear bearings perpendicular to the entrance axis in order to connect it with the light outlet of the source to be calibrated.

The toroidal mirror (see Fig. 3.10) images the light spot into the entrance slit of the monochromator. The solid angle of accepted radiation is precisely defined by apertures (not shown in Fig. 3.10). A spherical grating maps the entrance slit in the first spectral order into the exit slit, where the radiation of the selected wavelength is detected by a photomultiplier tube. The corresponding wavelength and the spectral resolution depend on the angular position of the grating, the grating constant, the slit width, and other parameters, which are optimized in order to suppress the influence of higher spectral order too. The measurement of the spectral radiant intensity is performed by varying the angle of the grating in different spectral ranges with a given resolution (wavelength scan). Additionally, it is possible to vary the angle of the toroidal mirror to measure the intensity at different horizontal and vertical positions at a fixed wavelength (in combination with appropriate apertures and slits) to record a spatial profile of the radiating spot and to align the image of the spot into the entrance slit of the monochromator. Four monochromator configurations were used to calibrate the VUV-simulator in the following spectral ranges with given resolutions:

- 40 nm to 120 nm, resolution: 0.2 nm,
- 110 nm to 220 nm, resolution: 0.2 nm,
- 160 nm to 330 nm, resolution: 1 nm,
- 300 nm to 410 nm, resolution: 1 nm.

The first step for the calibration of the VUV-simulator was the alignment to the entrance axis of the monochromator and the connection of the vacuum systems of both facilities. After first wavelength scans in the range between 110 nm and 220 nm a relatively intense spectral line was chosen for the alignment of the electron beam to the gas jet. That means, the monochromator was adjusted to that intense wavelength (e.g. 123.62 nm) and the orientation of the electron source and the gas nozzle were changed during the timely monitoring of the detector signal to find the optimum. The same procedure was performed for the setting of the magnetic lens current. After that, the wavelength scans were performed with the settings of the VUV-simulator described in Section 3.4.1 in the spectral ranges given above.

3.4.3 The VUV spectra, comparison to the solar spectra

Spectral intensity distribution

In order to get the spectral radiant intensity in W sr^{-1} nm^{-1}, the measured detector signals in the described wavelength ranges were converted with the corresponding measurement site sensivity by PTB. By use of the geometrical parameters of the CIF that spectral radiant intensity was re-calculated into spectral irradiance at the position of the object under test in W m^{-2} nm^{-1}. Since for each parameter setting several measurements have been performed, an averaged spectral distribution was calculated.

The resulting spectral irradiance distributions are shown in Figs. 3.11-3.14 for each gas flow (300, 600, 1200 sccm) with a different color. The integral irradiance for each configuration of the VUV-source is given in the legend. A survey of all spectra over the whole range from 40 to 410 nm is presented in Fig. 3.15.

The spectra of the VUV-simulator are characterized by a large number of lines. I have made the verification of these spectral lines by use of the database of the National Institute of Standards and Technology (NIST) [14]. Each identified spectral line is marked in Figs. 3.11-3.14 by a label which contains the name of the chemical element and the degree of ionization. An overview of all identified spectral lines is presented in the Appendix C (Table C.1).

Spectral lines in the wavelength range from 138 nm to 160 nm are classified separately (see Fig. 3.12 and Table C.2). For larger gas flows the spectral lines in that range disappear and large bumps appear. This is an effect of the increasing number of collisions between the gas atoms. That result in a broadening of the spectral lines which form eventually a continuum. The NIST database possesses in this wavelength range 112 Ar lines, 140 Kr lines and no He lines.

In order to get an idea how good the VUV-source simulates the solar spectrum, the appearance of solar spectral lines and their possible counterparts of the VUV-simulator has to be studied.

Since the ASTM E-490 standard of the spectral solar emissivity covers the wavelength range from 119.5 nm to 1000000 nm, the Gueymard database [73] is used as a reference for wavelengths < 120nm. The VUV-simulator spectrum and the Gueymard standard are shown in Fig. 3.16. From 119.5 nm to 150 nm the VUV-simulator spectrum coincides well with the solar emission lines. Below 119.5 nm the spectral intensity of the VUV-simulator is larger than the solar one. Since the VUV-source has a very small intensity for wavelengths above 150 nm, this range must be covered by the light of a Deuterium lamp - another light source of the CIF, see Section 3.3.

To compare the VUV-simulator emission lines with the solar ones, I have used the SUMER database [15] as a reference. A Lyman-α line at 121.57 nm has been identified both in the spectrum of the VUV-simulator and in [15]. Its intensity in the spectrum of the VUV-simulator is 18% of the corresponding solar one. Strong Hydrogen lines of the VUV source are present at: 91.93 nm (131 times stronger-), 93.07 nm (138 times stronger-), and 94.97 nm (10 times stronger- than the Sun spectrum at that wavelengths). The presence of Hydrogen and residual water vapor in the VUV-simulator is a consequence of the fact, as it is the predominant residual gas in metal vacuum systems at very low pressures [80]. The two strongest lines of the VUV-source spectrum appear at 104.82 nm and 106.61 nm. They correspond to the Ar I and Cu II lines that are 2922 - times and 1423 - times stronger than the solar spectrum at these wavelengths. In the solar spectrum these lines are not present. Also not present in the solar spectrum are the VUV-source lines at 123.62 nm and 116.49 nm (Kr I and Cr III). The Ar- Kr- and He-lines are caused by constituents of the gas flow excited by the electron beam. The metal lines such as: Cu, Cr, W, Fe, Mo, Ni, La and Al originate from the construction materials of the VUV-simulator. These lines are constituents of the solar spectrum too [15].

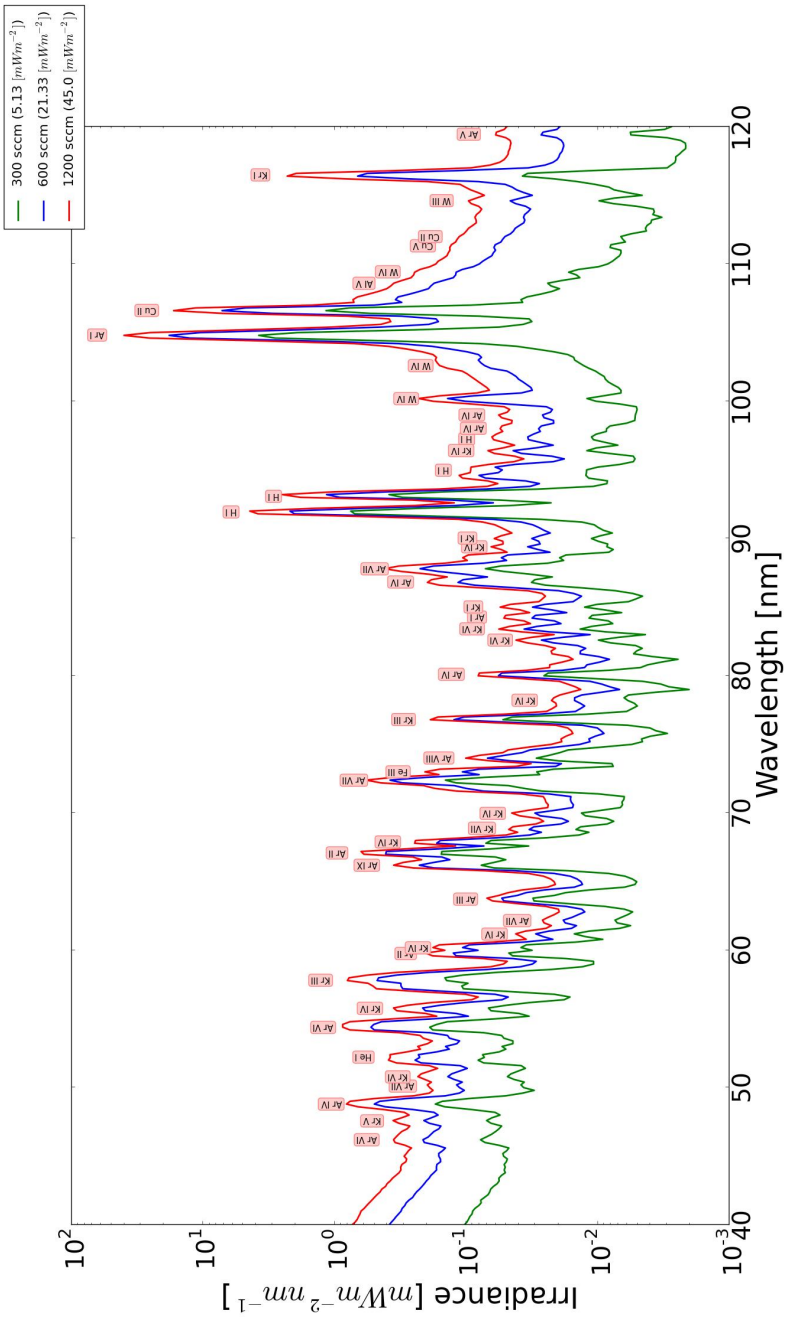

Figure 3.11: The VUV spectral lines in the wavelength range from 40 nm to 120 nm for different gas flows: 300 (green line), 600 (blue line) and 1200 (red line).

Acceleration factors

The acceleration factor of material tests for space application is generally defined as the ratio of the intensity of a degrading radiation applied to a material at the laboratory versus the intensity of the same degrading factor in space [2]. In the following the acceleration factors achieved by the VUV-

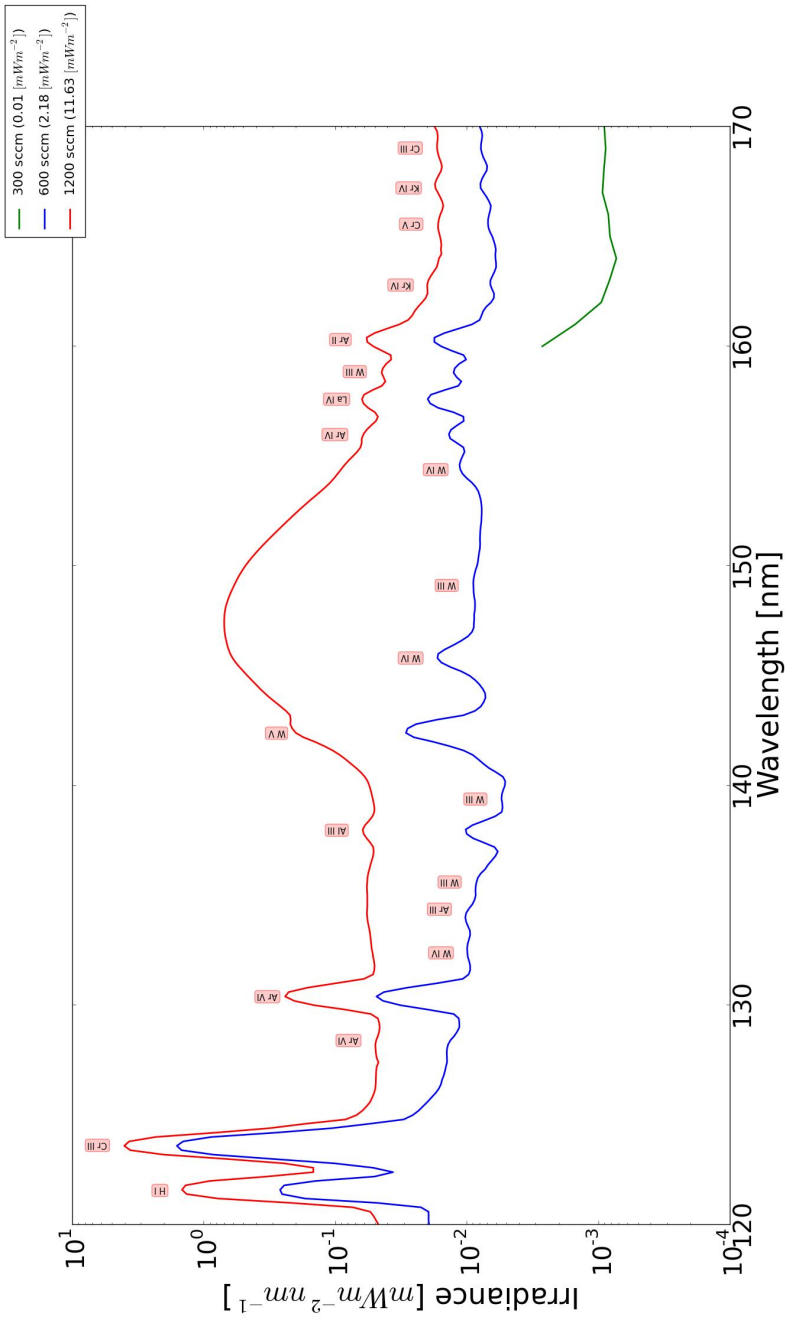

Figure 3.12: The VUV spectral lines in the wavelength range from 120 nm to 170 nm for different gas flows: 300 (green line), 600 (blue line), 1200 (red line).

simulator are discussed. They are calculated as the ratio of its intensity in a certain spectral range to the intensity of the solar radiation in the same range at 1 AU. The factors decrease if materials are tested for space applications that go closer to the Sun, whereas the factors increase in the case of applications that veer away from the Sun.

The differential as well as integrated values of the Gueymard's and VUV-simulator's spectral

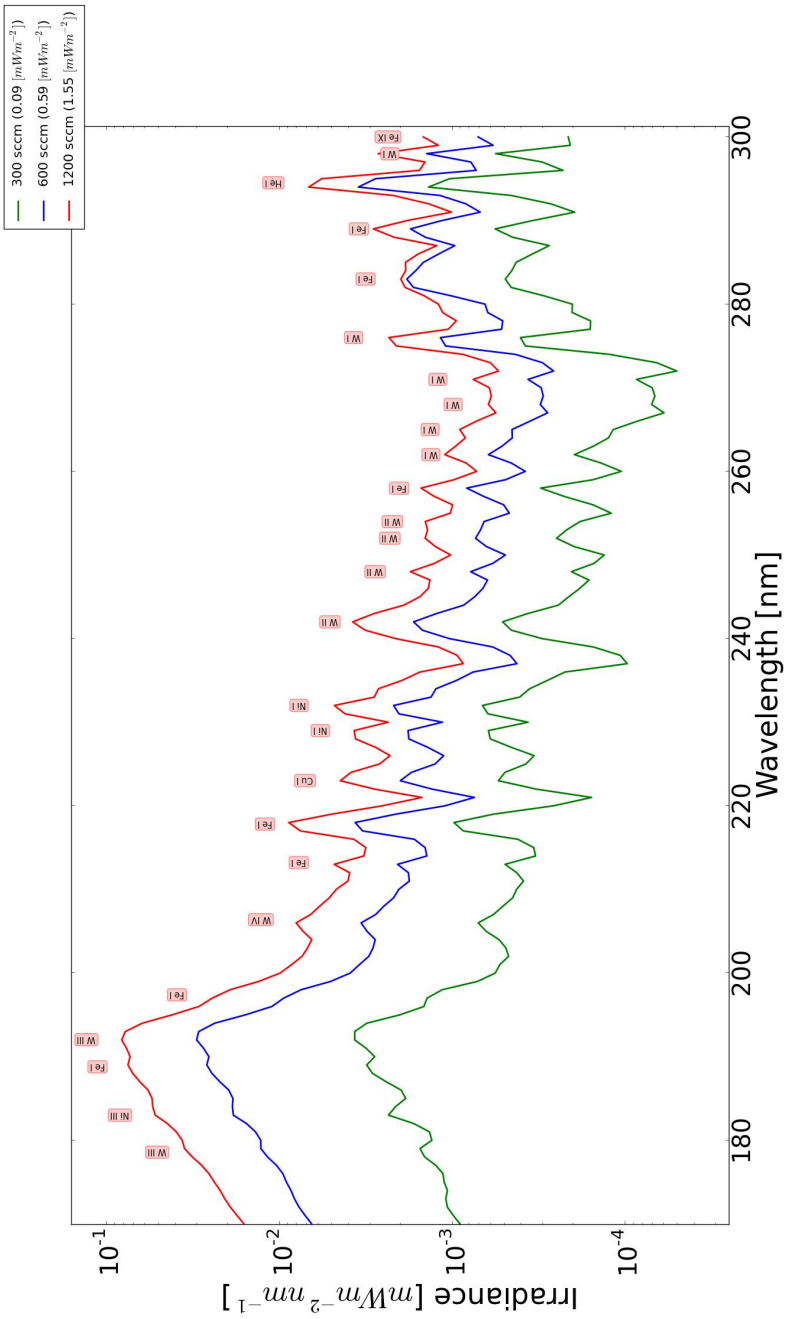

Figure 3.13: The VUV spectral lines in the wavelength range from 170 nm to 300 nm for different gas flows: 300 (green line), 600 (blue line), 1200 (red line).

intensities and acceleration factors are presented in Tables 3.2 and 3.3, respectively. The highest differential acceleration factor of 95.4 SC is reached in the wavelength range 100 nm to 110 nm and a gas flow of 1200 sccm (see Table 3.2). The integral of the VUV-simulator's irradiance can reach: 26.3 SC for a gas flow of 1200 sccm, 12.5 SC for a gas flow of 600 sccm and 3 SC for a gas flow of 300 sccm in the wavelength range from 40 nm to 120 nm. Fig. 3.16 shows the spectra of the VUV-simulator

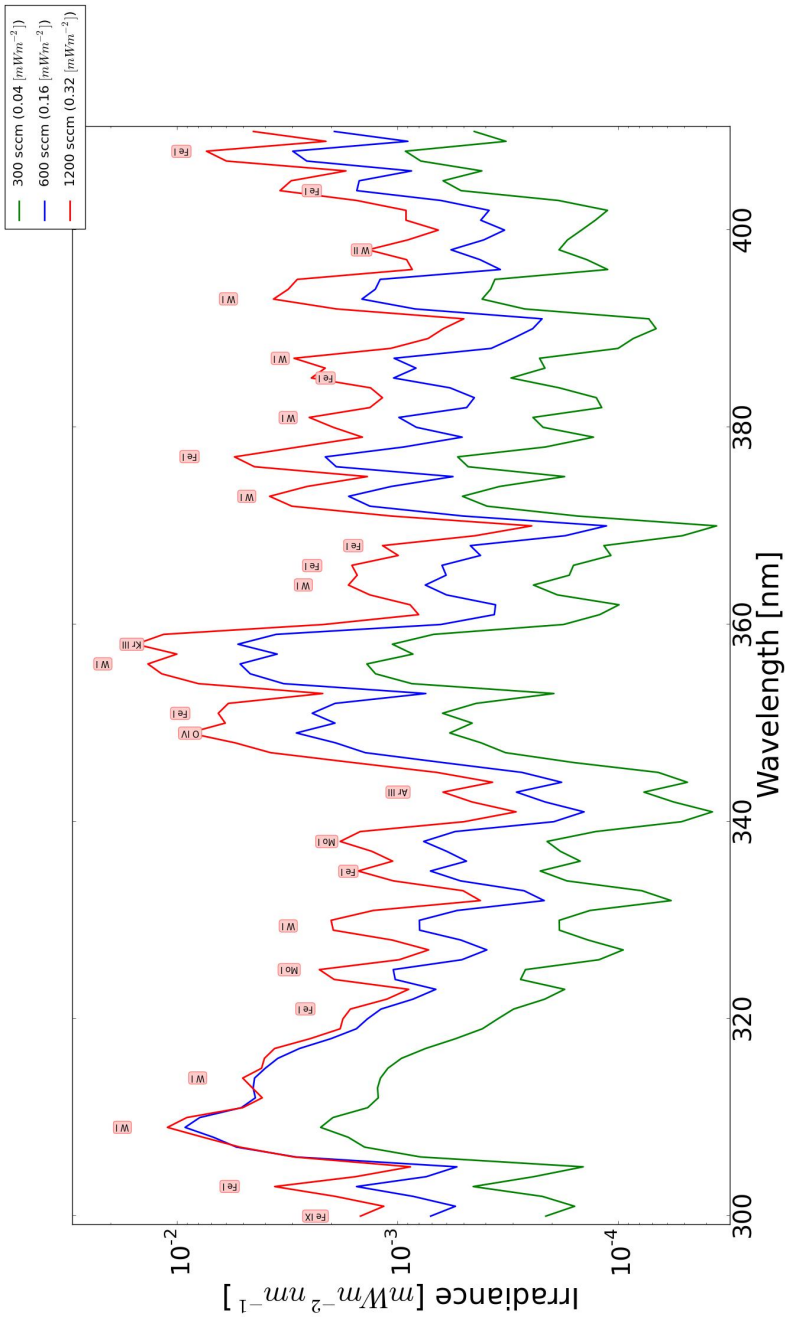

Figure 3.14: The VUV spectral lines in the wavelength range from 300 nm to 410 nm for different gas flows: 300 (green line), 600 (blue line), 1200 (red line).

for two different gas flows 600 and 1200 sccm. There is plotted the solar spectrum of the Gueymard database for comparison too. The solar spectral intensity is larger than that of the VUV-simulator at wavelengths higher than 150 nm.

The spectral distribution of the accelerating factors is presented in Fig. 3.17. The spectral intensity distributions of the VUV-simulator are divided by the solar ones taken from the Gueymard

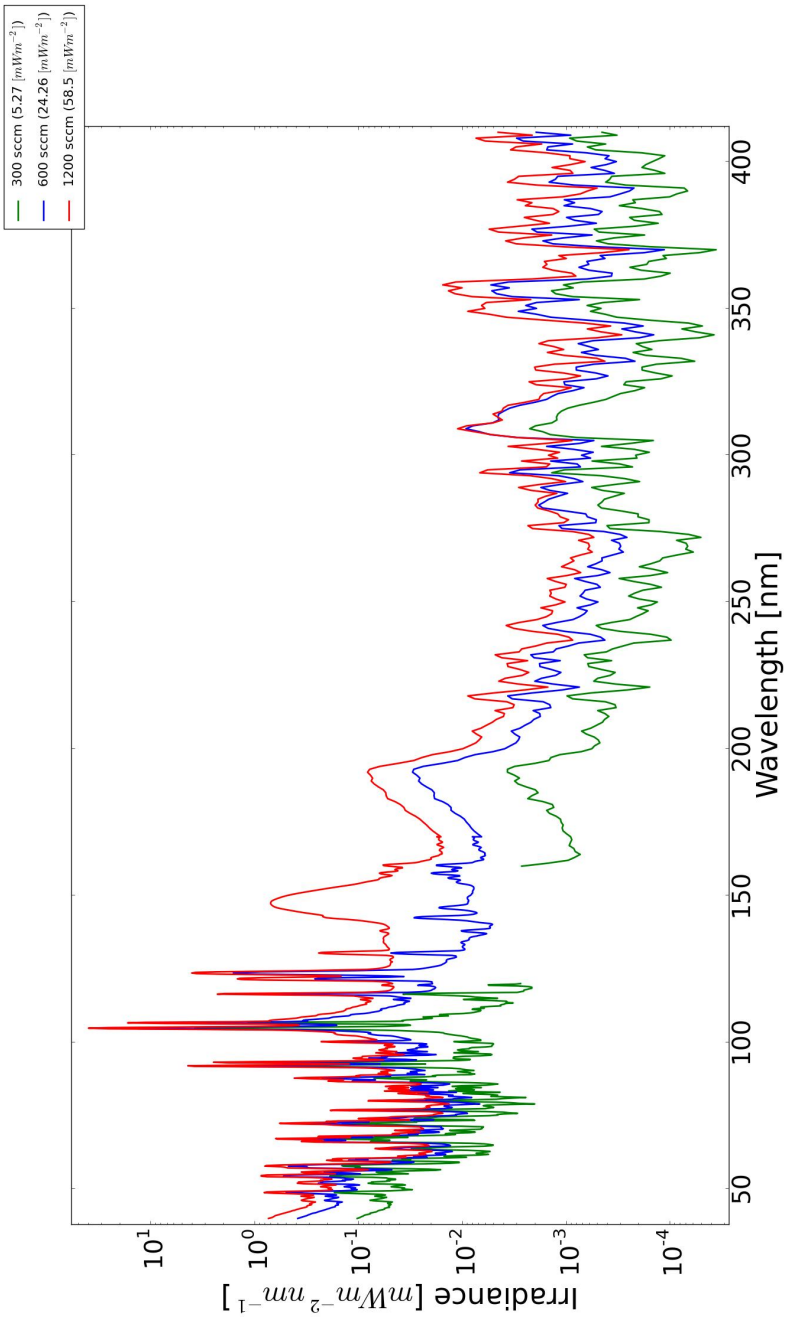

Figure 3.15: Summary plot of the VUV spectra in the wavelength range from 40 nm to 410 nm for different gas flows: 300 (green line), 600 (blue line), 1200 sccm (red line).

database for two representative gas flows. The acceleration factor is significantly larger than 1 in almost the complete range up to 120 nm. For wavelengths higher than 115 nm, a Deuterium lamp yields higher intensities and sufficiently large acceleration factors. Depending on the specific purposes of experiments to determine degradation effects of materials exposed to VUV radiation, the appropriate gas flow has to be chosen.

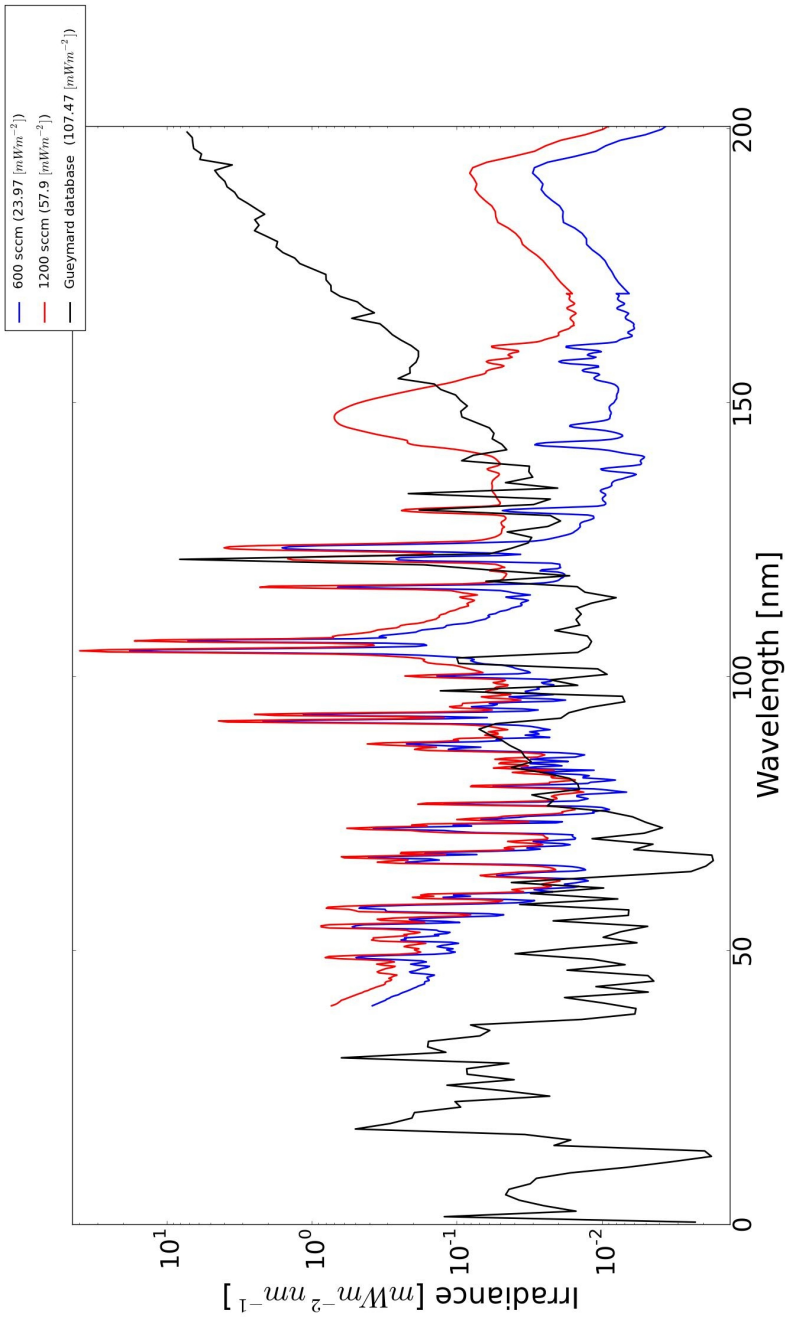

Figure 3.16: The spectra of the VUV-simulator for different gas flows (600 and 1200 sccm) comparing to the Gueymard database denoted as a black line. The given total intensity of the solar spectrum taken from the Gueymard database is calculated from 40 nm to 200 nm and it is shown in the legend.

The stability of the radiation intensity of the VUV-simulator

The presumption of the variability of the radiation intensity, as seen during the calibration campaign, has been confirmed by the stability analysis. In order to get an idea about the stability, several

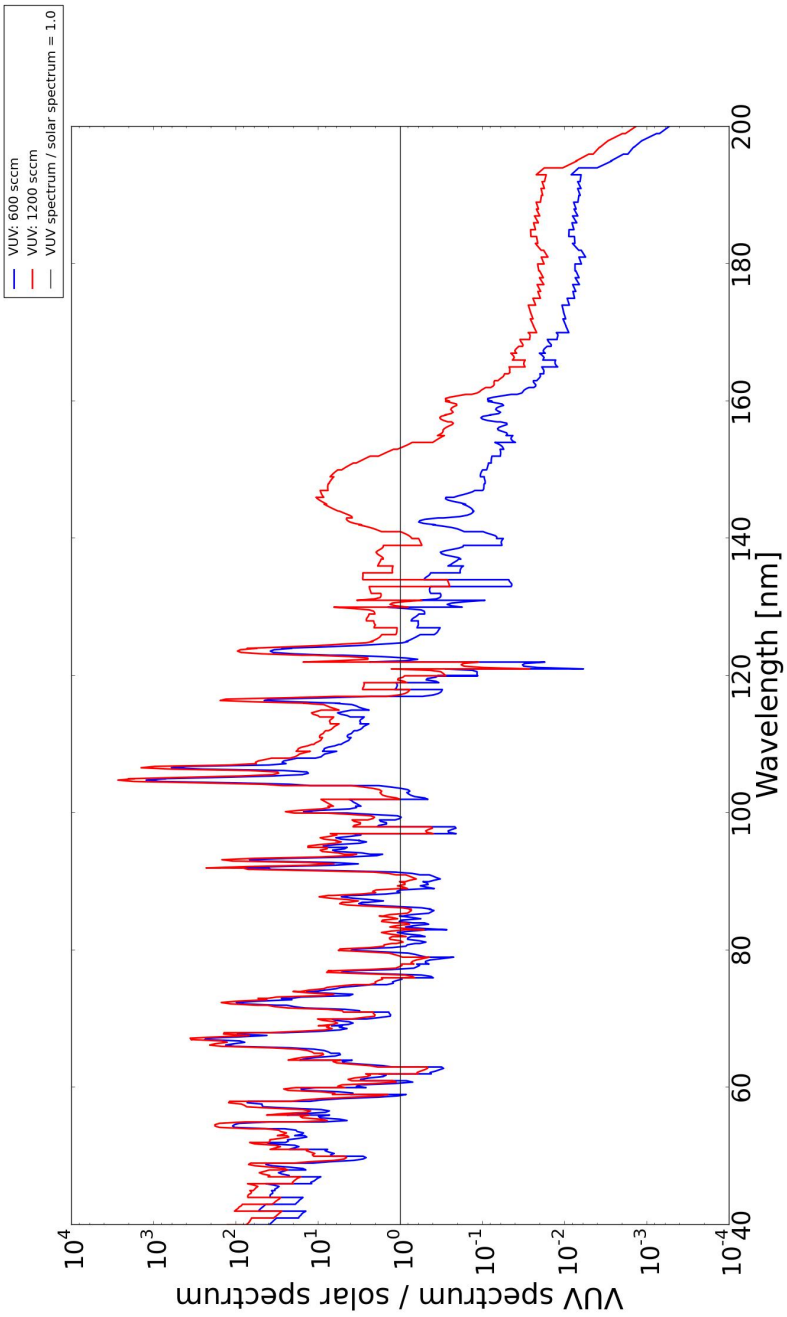

Figure 3.17: VUV spectra for gas flows of 600 and 1200 sccm divided by the spectrum of the Sun taken from the Gueymard database [73].

measurements with identical settings of gas flow and electron current has been performed at different days and different operating times after the regeneration of the source during the calibration process at PTB.

The stability is affected by different effects which may compensate each other, at least partially. One effect is the formation of ice at the cold baffles around the light spot. The growing lumps of

Table 3.2: The differential values of the Gueymard's and VUV-simulator's spectral intensities as well as acceleration factors in bins of 10 nm. Unfortunately, there is no matchable spectrum for a gas flow of 300 sccm in the wavelength range of $120 - 160$ nm.

Wavelength	Gueymard	300 sccm		600 sccm		1200 sccm	
nm	mW m^{-2}	mW m^{-2}	Acc.	mW m^{-2}	Acc.	mW m^{-2}	Acc.
40-50	0.11	0.69	6.27	2.23	20.27	4.05	36.82
50-60	0.14	0.62	4.43	1.85	13.21	3.09	22.07
60-70	0.11	0.28	2.55	0.69	6.27	1.08	9.82
70-80	0.13	0.19	1.46	0.49	3.77	0.79	6.08
80-90	0.33	0.14	0.42	0.42	1.27	0.76	2.30
90-100	0.37	0.63	1.70	1.85	5.00	3.74	10.11
100-110	0.31	2.51	8.10	13.11	42.29	29.56	95.35
110-120	0.21	0.07	0.33	0.07	3.33	1.93	9.19
120-130	8.58	-	-	1.77	0.21	5.24	0.61
130-140	0.67	-	-	0.12	0.18	0.70	1.04
140-150	0.69	-	-	0.11	0.16	4.02	5.83
150-160	1.65	-	-	0.11	0.07	1.46	0.88
160-170	3.60	0.01	2.78×10^{-3}	0.08	0.02	0.22	0.06
170-180	11.09	0.01	9.02×10^{-4}	0.08	7.21×10^{-3}	0.21	0.02
180-190	26.01	0.02	7.69×10^{-4}	0.18	6.92×10^{-3}	0.53	0.02
190-200	53.47	0.02	3.74×10^{-4}	0.19	3.55×10^{-3}	0.53	0.01

Table 3.3: The integrated values of the Gueymard's and VUV-simulator's spectral intensities as well as acceleration factors with fixed lower limit of the wavelength range (40 nm). Unfortunately, there is no matchable spectrum for a gas flow of 300 sccm in the wavelength range of $120 - 160$ nm.

Wavelength	Gueymard	300 sccm		600 sccm		1200 sccm	
nm	mW m^{-2}	mW m^{-2}	Acc.	mW m^{-2}	Acc.	mW m^{-2}	Acc.
40-50	0.11	0.69	6.27	2.23	20.27	4.05	36.82
40-60	0.25	1.31	5.24	4.08	16.32	7.14	28.56
40-70	0.36	1.59	4.42	4.77	13.25	8.22	22.83
40-80	0.49	1.78	3.63	5.26	10.73	9.01	18.39
40-90	0.82	1.92	2.34	5.68	6.93	9.77	11.91
40-100	1.19	2.55	2.14	7.52	6.32	13.51	11.35
40-110	1.50	5.06	3.37	20.64	13.76	43.07	28.71
40-120	1.71	5.13	3.00	21.33	12.47	45.00	26.32
40-130	10.29	-	-	23.11	2.25	50.25	4.88
40-140	10.96	-	-	23.22	2.12	50.95	4.65
40-150	11.65	-	-	23.33	2.00	54.97	4.72
40-160	13.30	-	-	23.44	1.76	56.43	4.24
40-170	16.90	-	-	23.52	1.39	56.64	3.35
40-180	27.99	-	-	23.60	0.84	56.86	2.03
40-190	54.00	-	-	23.78	0.44	57.39	1.06
40-200	107.47	-	-	23.98	0.22	57.92	0.54

ice decrease the pumping power. Therefore, the intensity could increase because the gas density increases. It has to be mentioned, that this increase of intensity is mostly seen in measurements performed at the same day, however, not always and not in the full spectral range. On the other hand, the apertures at the cold baffles for the electron beam and for the light outlet will freeze up at longer operating time. That may cause a decrease of intensity. It will be reduced by the lower and/or defocussed electron beam and/or the lower solid angle of the out-coming light. Other the stability influencing effects are a small variation of both the gas flow and the electron current.

Due to the small number of comparable measurements a complete statistical analysis was not

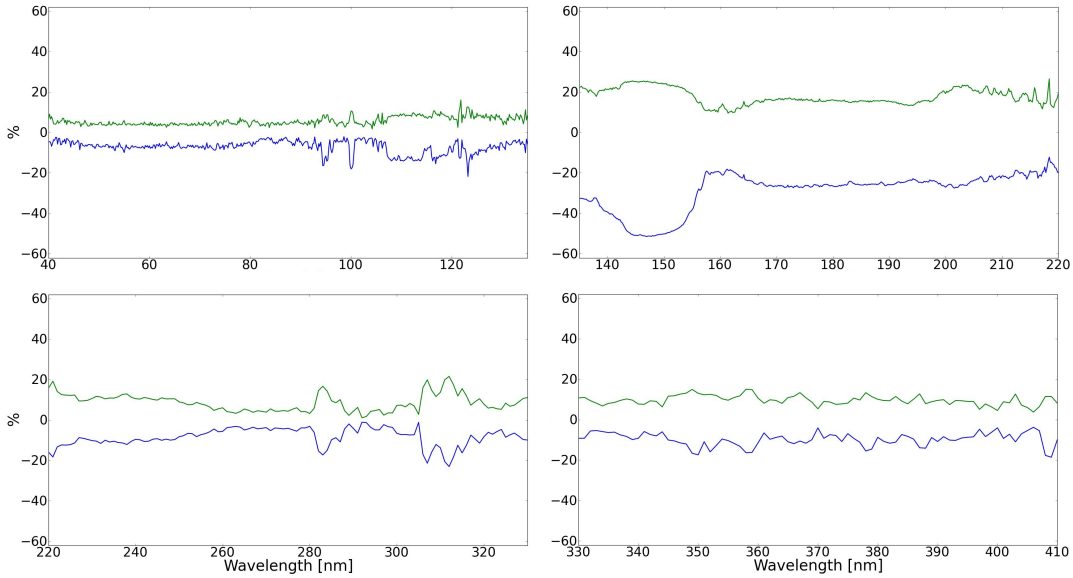

Figure 3.18: The maximum deviation (green line positive, blue line negative) of the spectral intensity distribution in the 4 spectral ranges related to their mean value.

feasible. Instead, a worst case estimation has been performed as follows.

The stability of the VUV-simulator has been estimated by comparing the intensity spectra taken at almost identical settings but made at as far as possible distant moments in time. The different number of measurements at each spectral range ($40-135$ nm: 3; $135-220$ nm: 9; $220-330$ nm: 5; $330-410$ nm: 5) was taken into account to determine the mean value. The maximum deviation was calculated by division of the maximum respectively the minimum intensity by the mean value at each wavelength. The results are shown in Fig. 3.18 only for the gas flow of 1200 sccm.

The lowest deviation to the average signal of +/- 10% appears in the wavelength range from 40 nm to 105 nm. Above 105 nm to 135 nm are bands where the deviation is +/- 20% (see upper left plot). The highest one of -50% is in the wavelength range of 145 nm to 155 nm, while in the range of 160 nm to 220 nm the deviation is +/-25% (see upper right plot). In the ranges of 220 nm to 330 nm and 330 nm to 410 nm the deviation from the average signal is equal or less than +/- 20% (see lower left and right plot).

The analysis of the plots in Fig. 3.18 shows an increase of the maximum deviation in the higher wavelength ranges. This result is influenced by the different number of measurements too. Nevertheless, it is acceptable in the range of short wavelengths. This stability analysis shows that the VUV simulator is not qualified as a calibration standard, i.e. for detector calibration. However, the stability in the VUV range is sufficient to perform irradiation tests for material investigations. The larger deviations in higher wavelength ranges are not a serious problem since the intensity there is at least one order of magnitude smaller than in the range below 115 nm see Figs 3.15 and 3.16. The very low intensity of the VUV-simulator at wavelengths larger than 115 nm is in the CIF compensated by the Deuterium lamp. It exceeds for wavelengths > 115 nm the solar intensity by about one order of magnitude.

3.4.4 Summary

Short wavelength electromagnetic radiation as generated by the VUV-simulator plays a crucial role in space material science due to photoionization and photodissociation effects. The maximum acceleration factor reached at the wavelength range from 40 nm to 120 nm is about 26.3 SC at a gas flow of 1200 sccm. In the same range but at a gas flow of 600 sccm the acceleration factor is 12.5 SC. With the smallest gas flow used in the calibration procedure (300 sccm) the factor is about 3 SC. Since the source has many operational parameters (see Section 3.4.1), changes of the gas flow will cause variations of the acceleration factor. Given an operating time of at least 8 hours and the large acceleration factors, the VUV-simulator is a suitable facility for various material tests and degradation experiments.

The simulator passed the first campaign of the calibration procedure. The spectral lines are calibrated from 40 nm to 410 nm. Based on the experiences made with first VUV-simulator [77] a significant intensity down to 5 nm can be expected, i.e. this source would cover also the soft X-ray range of the solar spectrum. Therefore a second calibration campaign for wavelengths smaller than 40 nm is necessary. It can be performed at the recently set-up facility for source calibration at the Metrology Light Source of PTB (MLS) [81].

The calibration procedure has proved that the VUV-simulator meets the requirements with respect to the solar spectral intensity distribution, the achievable acceleration factors, and the size of the irradiated area.

The stability analysis of the VUV-simulator signal shows that the maximum intensity deviations in the VUV range below 115 nm are in the order of 10%. The larger deviation for wavelengths above 115 nm are not a serious problem for material testing in the CIF because the VUV-simulator intensity in that range is negligible small and the Deuterium lamp is used (see Section 3.4.3) Therefore, a satisfactory operation of the VUV-simulator can be expected. Nevertheless, in a forthcoming calibration campaign the stability will be subject of a more systematic analysis.

3.5 Conclusions

The knowledge of degradation processes of materials under space conditions must be deepened. Therefore, the DLR Institute of Space Systems in Bremen has commissioned a new facility to study the behavior of materials under complex irradiation and to investigate their degradation in a space environment. With the CIF it is possible to irradiate samples with three light sources (for the simulation of the spectrum of solar electromagnetic radiation) simultaneously with protons and electrons. The light sources are a solar simulator with a Xenon lamp (wavelength range 250 to 2500 nm), a deuterium UV-source (112 to 400 nm), and a VUV-simulator (40 to 410 nm). The latter enables the irradiation of samples with shorter wavelengths below the limitation of any window material. All sources have been calibrated by the PTB and DLR-Berlin. The availability of UV-radiation below 115 nm is a particular advantage of the CIF. For such small wavelengths ionization of metal atoms can appear. In the Figs. 3.19 and 3.20 the spectral distribution in the short wavelength range is presented in detail, while Fig. 3.21 gives an idea about the acceleration factor of the whole electromagnetic spectrum covered by the CIF sources.

As seen in Fig. 3.19, 3.20, and 3.21 there is a significant gap between 180 and 250 nm in the UV-spectrum and in the corresponding acceleration factor. This will be closed in the near future by modification of the solar simulator.

In addition to the different light sources, CIF provides electron and proton irradiation. The charged particles are generated in a low energy range from 1 to 10 keV with currents from 1 to 100

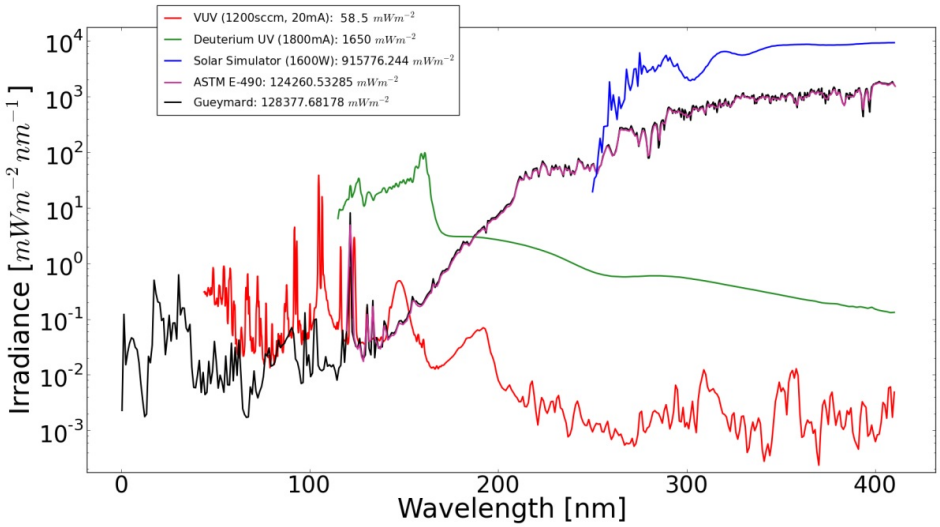

Figure 3.19: The spectra of the CIF light sources compared to the solar radiation standards [72, 73]. Both standards are shown, however, the ASTME-490 standard (pink line) reaches down to 120 nm only, while the Gueymard standard (black line) covers the range from 0.5 nm to 450 nm.

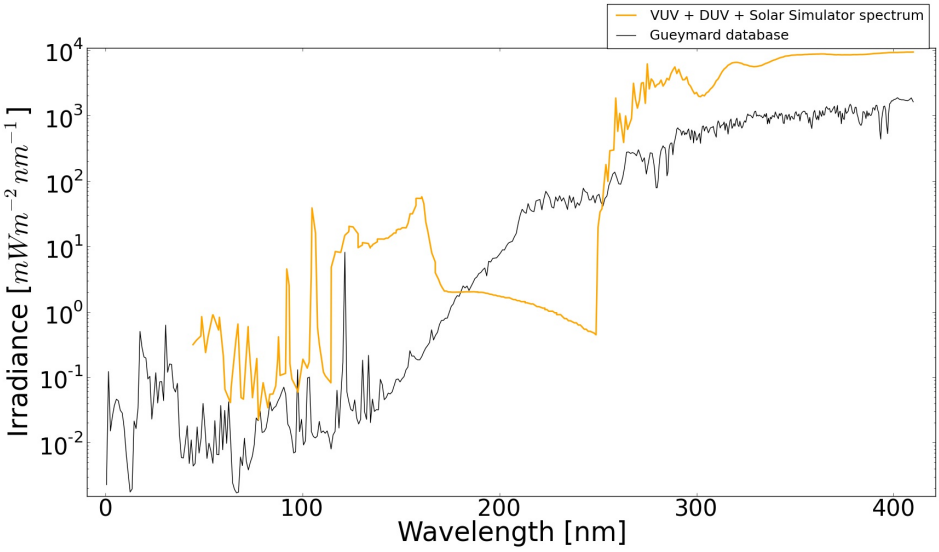

Figure 3.20: Overall spectrum of electromagnetic radiation of the CIF in the wavelength range from 40 nm to 410 nm in comparison to Gueymard database [73].

nA and in a higher range from 10 to 100 keV with 0.1 to 100 μA. Both particle sources can be operated simultaneously. However, another advantage of the CIF is that electrons and protons are led in a common beam onto the sample. In order to model temperature variations as appear in free space, the sample can be cooled down to liquid Nitrogen level and heated up to about 450°C by halogen lamps behind the target.

The complete facility has been manufactured in UHV-technology with metal sealing. It is free of organic compounds to avoid self-contamination. The different pumping systems achieve a final

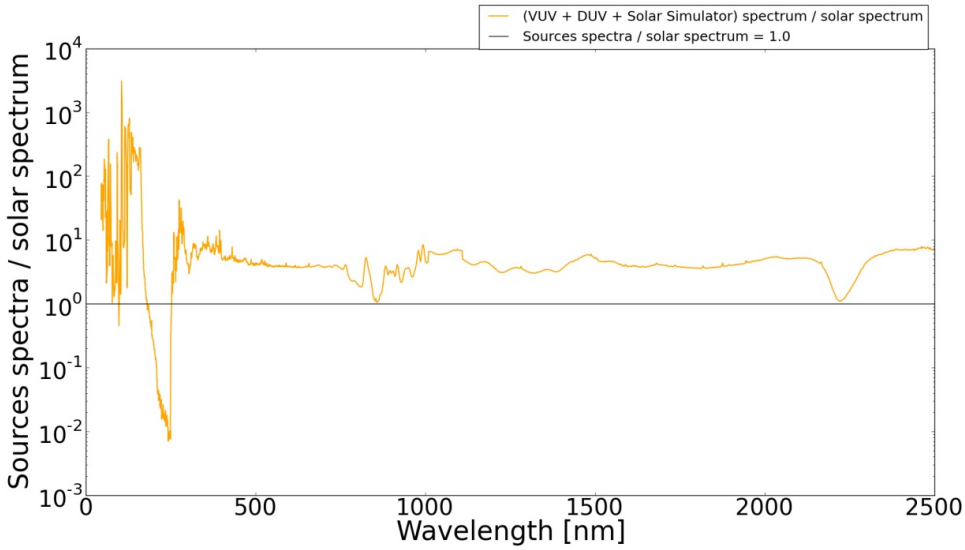

Figure 3.21: Spectral distribution of the acceleration factor of electromagnetic factor of electromagnetic radiation in comparison to [72, 73] in the whole spectral range covered by the CIF radiation sources.

pressure in the 10^{-10} mbar range (empty irradiation chamber). Besides the installed radiation sensors, which control the stability of the various radiation sources, and an attached mass spectrometer for analyzing the outgassing processes in the irradiation chamber, the construction of CIF allows adding other in-situ measurement systems to measure parameters that are of user's interest. It is planned to develop an in-situ measurement system in order to determine degradation caused changes in the thermo-optical properties of the samples without leaving the vacuum.

The future activities of the CIF facility are not only focused on tests of materials which will be used in the GOSSAMER solar sail project [11]. The Complex Irradiation Facility is a device that can be used in a wide spectrum of degradation investigations. Thus, it will irradiate materials that are supposed to be used in the construction of satellites such as multilayer insulations, ropes and other support structures. With its light sources together with proton and electron guns one can plan, manage and execute simulations of erosion effects of materials with large acceleration factors. Thereby, the CIF allows the study of degradation effects as may appear in long-term space missions. Moreover, the CIF will be used safely for studies in the field of planetary research.

Chapter 4

Degradation of materials under space conditions

4.1 Overview of degradation processes

4.1.1 Positive electric charging of foils due to irradiation

Metallic surfaces will lose electrons and become positively charged by ionization. This can be caused by the photoelectric effect, by Compton scattering, and/or by electron - positron pair production when high-energy photons interact with metallic ions [22]. For instance electrons may be ejected from the surface by the Auger-process (see Section 2.4.1). Part of the electron flux will escape from the metal surface, another part will be attracted back by the positively charged metal and therefore partially neutralize it. A third part will produce an electron cloud near the surface, which will screen the electric field [22]. Also, electrons from solar wind can partially neutralize the positively charged metallic surface.

During the space mission total surface charge density can be written as:

$$\Delta Q_{\mathrm{s}} = e\left(\frac{dN_{\mathrm{i}}}{dt} - \frac{dN_{\mathrm{r}}}{dt}\right)\Delta t, \tag{4.1}$$

where dN_{i}/dt is the number of metal atoms ionized per second and square meter, dN_{r}/dt is the number of ions recombined per second and square meter, Δt is the operation time of the space mission [22]. Now the rate of ionization can be determined. It is shown e.g. by Kezerashvili and Matloff [22] that only a small fraction of $X\%$ of metal atoms are ionized. X has to be determined experimentally. In order to estimate the recombination rate of metal atoms per unit area, the number of recombined metal ions per mass has to be calculated. In kg this is [22]:

$$\frac{N_{\mathrm{A}}}{A10^{-3}} \cdot \frac{X}{100}, \tag{4.2}$$

where N_{A} is Avogadro's number and A is the mass number. Multiplying this number by the material density ρ_{material} and the thickness of the metallic structure L (see Fig. 4.1 [22]), the number of recombined ions per unit area is then:

$$\frac{N_{\mathrm{A}}\rho_{\mathrm{material}}L}{A10^{-3}} \cdot \frac{X}{100}. \tag{4.3}$$

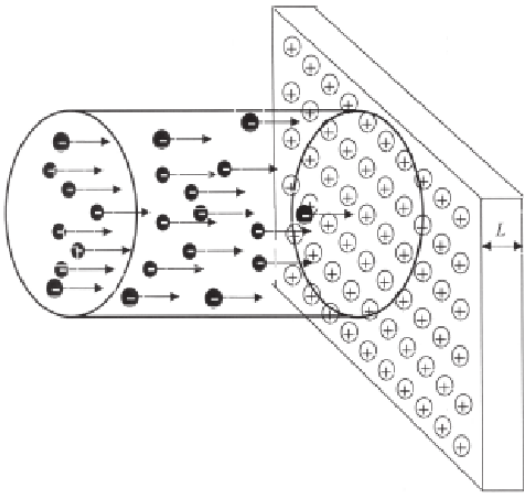

Figure 4.1: Schematic representation how solar wind electrons (black cycles) bombard metal ions (white cycles) of a surface of thickness L [22].

The flux of incident electrons is $n_\mathrm{e} \times v_\mathrm{e}$, where n_e is the number density and v_e the velocity of the incident electrons, respectively. Hence the recombination rate per unit time and area is:

$$\frac{dN_\mathrm{r}}{dt} = n_\mathrm{e} v_\mathrm{e} \frac{N_\mathrm{A} \rho_\mathrm{material} L}{A \cdot 10^{-3}} \frac{X}{100} \Sigma_\mathrm{RR} \tag{4.4}$$

where Σ_RR is the total cross section of radiative recombination processes. The cross section decreases with increasing electron energy, as the Bethe-Bloch-equation for the interaction of electrons with metal surfaces proves [18]. The recombination rate increases with:

- number density of incident electrons,
- velocity of incident electrons,
- thickness and density of the metallic foil,
- the total cross section of radiative recombination.

On the other hand it decreases with mass number of metallic structure. A charged metallic surface can cause a failure of the electrical equipment mounted in the spacecraft. Charged foils can cause also distortions in a trajectory of e.g. sail-craft, since solar ions are screened by the foil and an additional pushing force may act. Therefore, sophisticated methods have to be developed to discharge the metallic surfaces.

4.1.2 Sputtering - removal of the metallic foil ions by the incident particles

Sputtering is defined as removal of material atoms by incident particles: neutral atoms, neutrons, protons or electrons. The sputtering is a well investigated subject, there exist many reviews [82, 83, 84, 85, 86, 87]. Sputtering as a physical process has many useful applications:

- the production of atomically clean surfaces in vacuum,
- analysis of surfaces,
- the production of the thin films.

The production of atomically clean surfaces was studied by Fransworth et al. [88]. They have described how impurities are removed from surfaces. The bombardment of surfaces with neutral or charged particles has, however, some unwanted side effects: it damages the surfaces. In this thesis it will be considered only the second point: the analysis of the surfaces and their damages.

Methods to analyze materials by sputtering was studied e.g. by Liebl and Herzog [89]. The idea is to sputter a target, and the fraction of particles that leaves the material as ions is accelerated and analyzed in a mass spectrometer. This technique is known as the Secondary Ion Mass Spectrometry, the SIMS [86]. The idea is to measure the charged/neutral ratio of the sputtered ions, which depends on the state of the surface and can vary from one element to another. The SIMS method can provide useful information about the physical properties of the metallic foil [86]. Castaing and Slodzian [90] used the SIMS technique for spatial surface analysis. Abdullayeva el al. [91] have used secondary ions from sputtered surfaces to produce negative ions for particular applications [86].

An appropriate theory of sputtering was developed e.g. by Sigmund in 1969 [87]. Sigmund's description is based on collision processes, Boltzmann's equation and general transport theory. Sputtering takes place when the incident atoms that sputter off surface ions have a larger kinetic energy than the surface binding energy of the metal ions. A collision cascade can be initiated when the incident particle energy E is sufficient to transfer an energy greater than the displacement energy of a lattice atom. Sigmund considered the amount of energy per unit length $F(x, E, \kappa)$ that is transferred to the lattice in a layer of a thickness dx at x close to the surface by incident particles of an energy E; κ is the direction cosine. He has shown that the number of low-energy atoms which are put in motion in an energy range from E_0 to $E_0 + dE_0$ (where E_0 is the energy of sputtered ions) in the pre-defined layer is [85, 86, 87]:

$$\frac{6}{\pi^2}\frac{F(x, E, \kappa)}{E_0^2}dE_0dx, \qquad E_0 \ll E. \tag{4.5}$$

To calculate the number of surface atoms $SY(E, \kappa)$ that acquired sufficient energy to overcome the surface binding energy, Eq. 4.5 should be integrated over the surface [85, 86, 87]. The result is:

$$SY(E, \kappa) = \frac{3}{4\pi^2}\frac{F(0, E, \kappa)}{n_0 U_0 C_0}, \tag{4.6}$$

$SY(E, \kappa)$ is also known as a Sputtering Yield. Here n_0 is the number density of material atoms in a unit volume, U_0 is the surface binding energy, C_0 is a constant value with a dimension of an area [86, 87]. The energy loss per unit length $F(x, E, \kappa)$ is in detail derived in Winterbon et al. [92]. For the low incident particle energies up to 1 keV, Eq. 4.6 can be approximated by:

$$SY(E, \kappa) = \alpha_{\mathrm{m}}\frac{3}{4\pi^2}\frac{4mM}{(m + M)^2}\frac{E}{U_0}, \tag{4.7}$$

where m is the mass of the incident particle, M is the mass of the material ion, α_{m} is a dimensionless physical quantity which depends on the ratio M/m. For the high energy incident particle energies greater or equal than 1 keV [86] the Sputtering Yield is:

$$SY(E,\kappa) = 0.042\alpha_{\mathrm{m}} 4\pi Z_m Z_M \frac{ae^2}{U_0}\left(\frac{m}{m+M}\right) s_n(\epsilon_{\mathrm{m}}), \tag{4.8}$$

where $\epsilon_{\mathrm{m}} = a\frac{ME}{m+M}/(Z_m Z_M e^2)$, Z_m, and Z_M are charge numbers of the incident particle and the material ion, respectively. $s_n(\epsilon_{\mathrm{m}})$ is a universal function tabulated by Lindhard et al. [93], $a = 0.8853 r_0 (Z_m^{\frac{2}{3}} Z_M^{\frac{2}{3}})^{-\frac{1}{2}}$, and r_0 is the Bohr radius.

The Sputtering Yield can also be defined as a function of an angle between the normal to the irradiated surface and the path of the incident particles $SY(\theta)$:

$$SY(\theta) = \frac{SY(E,\kappa)}{SY(E,1)} = \sec^f \theta, \tag{4.9}$$

where f is a function of the ratio of the mass of a material ion and a mass of the incident particle M/m [86]. The coefficient is plotted in Fig. 4.2.

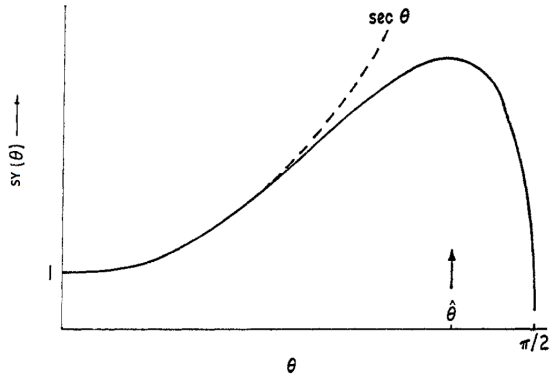

Figure 4.2: The Sputtering Yield as a function of angle θ [86].

$SY(\theta)$ has its maximum at $70^o \sim 80^o$ and then decreases to zero at 90^o. This fact cannot be explained in terms of the here presented theory, because according to the Eq. 4.9, $SY(\theta)$ is proportional to the secans of the angle θ [86]. However, the theory can explain the phenomenon up to $\theta \leq 80^o$, as it is seen in Fig. 4.2. For angles larger than 80^o sputtering is not a dominating degradation effect.

There exist many sputtering experiments. Karmakar et al. [94] investigated the sputtering on to a variety of thin metallic foils: Cobalt, Copper, Silver, Platinum and Gold. The thickness of films varied in the range of 30 - 200 nm. The samples were exposed to ion fluences of 1×10^{17} ions cm^{-2} for Cobalt, Copper, Silver and Gold and 5×10^{16} ions cm^{-2} for Platinum of the 16.7 keV Ar^+ ion beam. The base pressure in the target chamber was less than 5×10^{-8} mbar [94]. Results are presented in Fig. 4.3.

The first column shows non-irradiated surfaces, while the second, third and fourth columns show surfaces bombarded under $\theta = 60^o$, 70^o and 80^o with above mention fluxes, respectively. At 60^o ripples appear for Cobalt and Copper parallel to the ion beam direction. At 70^o arrays of tiny cones appear in the ion beam direction. At 80^o characteristic ripples appear in all films [94].

By use of the SRIM software, the Sputtering Yield can be calculated for a given angle between normal to the target and a beam line. 7.5 μm Kapton foil covered on both sides with 100 nm Aluminum, a typical material used in space industry, was examined. The Al-sample was irradiated perpendicular by incident protons. Fig. 4.4 shows the Sputtering Yield as a function of energy of incident protons. Results are derived for 1000 incident particles.

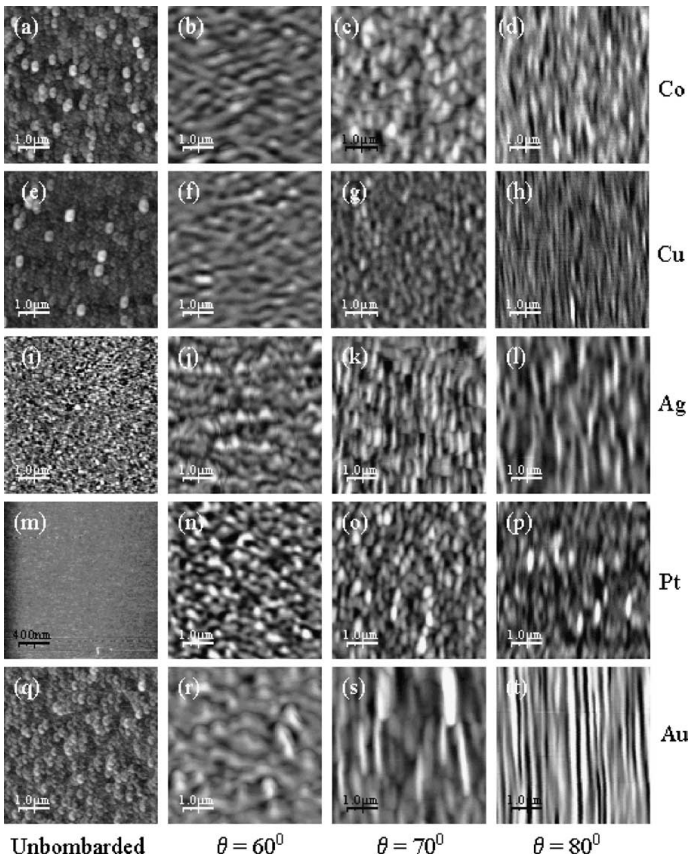

Figure 4.3: First column shows non-irradiated surfaces, second, third and fourth 60^o, 70^o and 80^o of the θ angle, respectively. Rows from top to bottom for: Cobalt, Copper, Silver, Platinum and Gold [94].

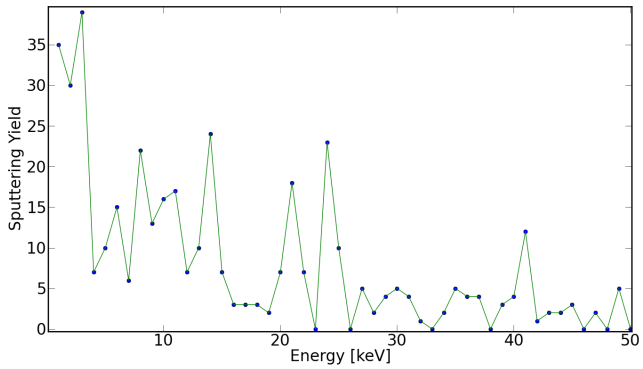

Figure 4.4: Sputtering Yield as a function of the energy of incident protons. The data were derived by use of the SRIM software [95].

The Sputtering Yield decreases with increasing energy. It is obvious because higher energetic particles penetrate the foil to deeper layers, while low energy incident particles degrade only the first few atomic layers of the foil. This causes the ejection of foil ions from the surface.

In the laboratory it is possible to measure the mass of a foil before and after irradiation. The mass difference is proportional to the number of sputtered ions. It is worth studying both experimentally and theoretically the Sputtering Yield for a given configuration of: energy of incident particles, angle between beam line and surface normal, type of target film, pressure and temperature conditions in the vacuum chamber, where the sputtering processes are observed.

4.1.3 Atomic Oxygen - ATOX

Atomic Oxygen (ATOX) in the Low Earth Orbits (LEOs) is known to cause severe damage to organic-based materials as well as to polymers and metals. It is produced by the photo-dissociation of molecular oxygen in the upper atmosphere by solar radiation of wavelength of about 243 nm [96]. Fig. 4.5 shows the relation between the altitude, the concentration of the ATOX and the ATOX flux in a height of 8 km [97]. For moderate solar activity and for an altitude of 500 km the concentration of ATOX is 10^7 cm^{-3} and the flux is 10^{13} cm^{-2} s^{-1}. In this altitude the thermal energy of ATOX is about 0.1 eV [96]. At LEO space vehicles are orbiting the Earth with velocities of 7.113 to 7.726 km s^{-1} [98]. Under such conditions the impact energy of ATOX on the satellite is about 5 eV.

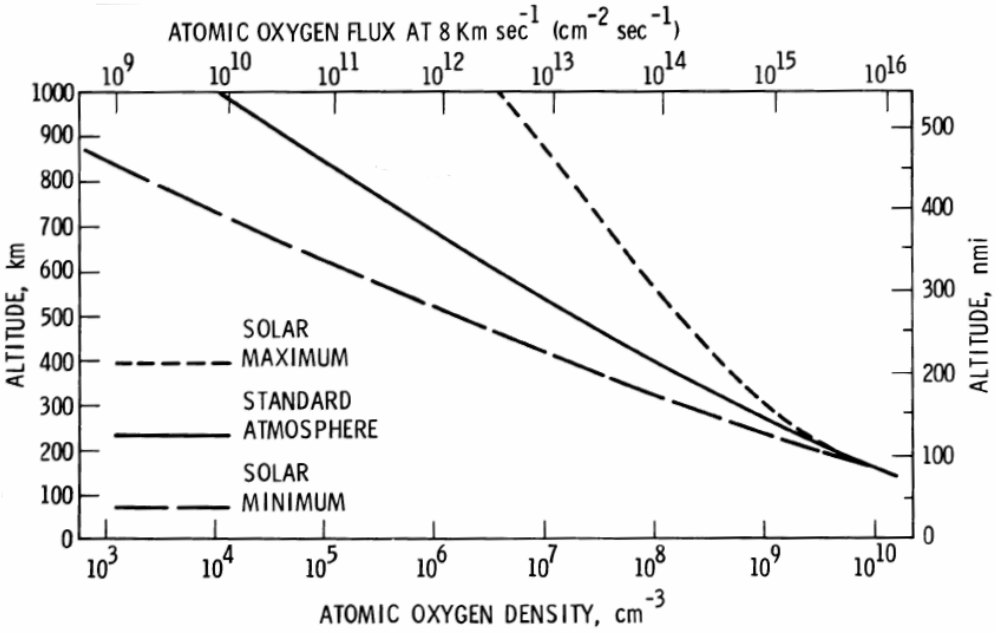

Figure 4.5: Atmospheric Atomic Oxygen density in Low Earth Orbit [99].

SASLab, the Laboratory of the Aerospace and Astronautics Engineering Department of the University of Rome, performed experiments with Kapton and Kapton-ge films. Kapton-ge film is a germanium coated Kapton film [100]. The SAS (Space Environment Simulator) facility simulates space conditions of the LEO in which the impacting kinetic energy between the spacecraft moving with speed 7-8 km/h and incident particles is approximately 4.5 - 5 eV [100, 101, 102]. SAS facility used ATOX as incident particles. Degradation processes manifest themselves as material's mass loss, changes of chemical, electrical, thermo-optical and mechanical properties of the irradiated foils [100, 103, 104].

Fig. 4.6 shows results of bombardment of Kapton (first columns) and Kapton-ge (second column) films. The Kapton film looks very smooth before bombardment (upper left, magnification 20000). After 1 h bombardment by ATOX ions with a fluence of 4.3×10^{18} ions cm^{-2} (lower left, magnification 60000) the surface is eroded and has a cone-like morphology [100]. Kapton-ge film before experiment (upper right) looks similar to the Kapton film. After 1 h of bombardment with the same fluence of ATOX ions, it's erosion looks very different (lower right): there appears only a slightly visible roughness of the surface. Of course the differences of the bombardment results are caused by structural differences between both films [100].

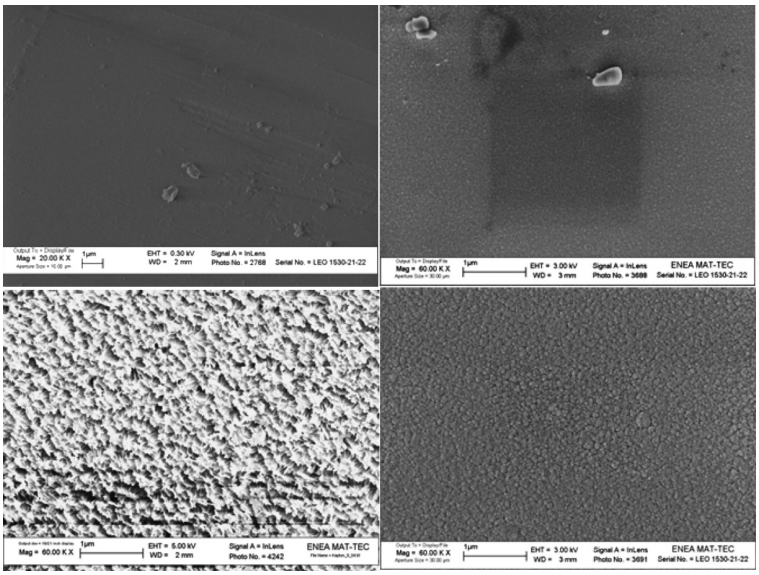

Figure 4.6: Two films, Kapton (first column) and Kapton-ge (second column) before (first row) and after (second row) bombardment of 4.3×10^{18} ATOX ions cm^{-2} in 1 hour experiment [100].

Degradation effects caused by ATOX are considered as one of the most serious hazard to spacecraft materials and are effective at altitudes between 200 and 700 km [99]. They change optical, mechanical, electrical, and chemical properties of materials [105]. Fig. 4.7 shows the erosion of a Kapton foil covered with Aluminum. The picture has been taken by an electronic microscope [106]. It gives an impression how a typical ATOX flux of 10^{13} cm^{-2} s^{-1} damages surfaces exposed to it over a few mission years.

4.1.4 Electromagnetic radiation

The effects of all degradations encountered in space can be represented by a decrease of the thermo-optical properties of investigated materials over the exposure time of materials [7].

The most important damages in the free space originates from the combined influence of the ultraviolet (UV) radiation at wavelength below 200 nm together and simultaneously with particle radiation by protons and electrons [5].

The role of UV radiation in degradation processes of space materials has been studied experimentally by many scientific groups. Selected results and conclusions are presented below.

Simultaneous UV and ionizing irradiations can give different results then those obtained during an irradiation using only one type of irradiation, or two types of irradiations sequentially carried out [107]. That has been shown by a series of experiments performed at ONERA/DESP. Various

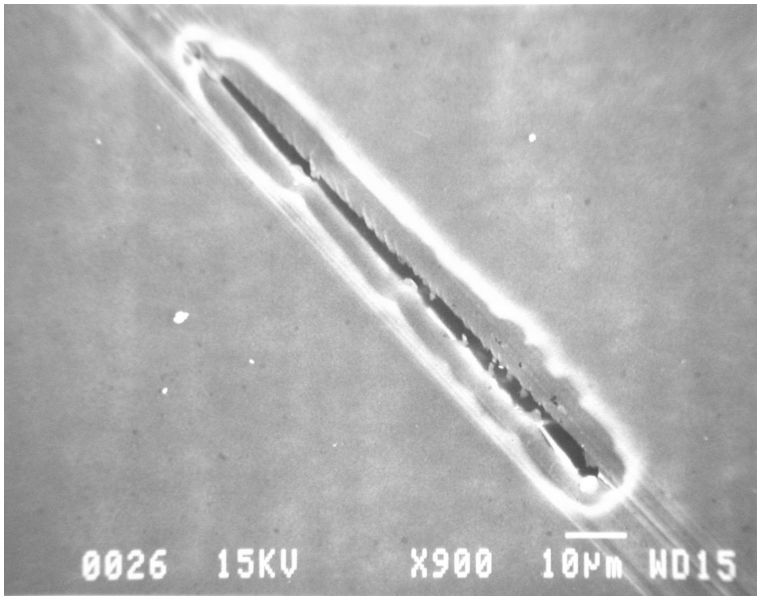

Figure 4.7: The scanning electron microscope photography. The crack is caused by ATOX bombarding an Aluminum covered Kapton film [106].

polymers and white paints have been irradiated: Polyimide Kapton, S13G/LO, PSG120, Z93 and PSZ 184 [107].

Studies of solar absorption coefficient α_S have been carried out by a DLR group in collaboration with the Institute of Physics and Power Engineering, Russia. It has been shown that UV radiation together with proton/electron irradiation causes a larger increase (about 131 %) of α_S, opposed to the exposure of the sample only to protons/electrons [3, 5]. The sample was a 7.5 μm thick Kapton foil, its front side was covered with a 100 nm Al layer and its back side with a 30 nm Chrome layer [5]. The black chrome back side guarantied a fast thermalization. The front side of the sample was exposed to the radiation sources.

According to the irradiation test performed in the SEMIRAMIS facility (ONERA), degradation of silicate (white ceramic) and silicone paints is higher with electrons than with UV light and proton irradiation [108]. The degradation of material was measured as a change of solar absorption coefficient and reflectance of irradiated probes. The test duration of 5 months simulated eight years of flight in a Geostationary orbit (GEO) [108].

Another set of tests has been performed by Sharma et al. [6]. The group used the SEMIRAMIS facility. The aim was to simulate the radiative geostationary space environment. Different kind of materials were examined: white paints, black paints, multilayer insulation materials (MLI), varnish coated aluminized polyimide, germanium coated polyimide, polyether ether katone (PEEK) and poly tetra fluoro ethylene (PTFE). The solar absorption coefficient α_S as well as the thermal emission coefficient ϵ_t were measured after 0.5, 1.0, 2.0 and 3.0 ESY (Equivalent Sun Years) of irradiation by UV-light. Note that Equivalent Sun Hour (ESH) is defined as a number of laboratory irradiation hours multiplied by the number of used solar constants in a given spectral range. For instance for MLI after 3 ESY of irradiation the α_S increased by a factor of 33% after UV exposure. The α_S increased by a factor of 48% when MLI was exposed to UV radiation together with irradiation of electrons and protons. For aluminized Polyimide foil and 3 ESY the α_S increased 46% after the exposure only to UV light. It increased 59% after irradiation of the sample with UV-light together with electrons

and protons. On the other hand the emissivity ϵ_t increased by a factor of: 2% and 3% for MLI and aluminized Polyimide, respectively. Consequently, the degradation effect is significantly larger for α_s than for ϵ_t. Note that ϵ_t was measured after the samples were exposed to UV-light and irradiated by electrons and protons together.

Unfortunately, the group used the sequential irradiation of the samples, which means that the probe was first exposed to UV-light then α_S was measured and after that the same sample was irradiated by electrons and protons and again α_S was measured. This method does not allow to examine the true role of degradation of the probe due to electron/proton irradiation alone, because the optical properties of the sample were already changed by the preceding UV irradiation.

The space mission BepiColombo to planet Mercury planned and prepared by ESA together with JAXA, provides a great opportunity to check the role of UV radiation in the degradation process of the protection shield of the spacecraft. Tests have been made in the ESA/ESTEC laboratories [4]. The shield has been produced with various silicate paints (white ceramic). Probes were irradiated by two types of UV radiation sources: a deuterium lamp (UV) and a VUV source. The UV wavelength bandwidth is 200 to 400 nm, while the VUV bandwidth is 115 to 200 nm. Probes were exposed at elevated (450^oC) temperature to UV and VUV radiation of approximately 17 Solar Constants (SC), accumulating a total UV dose of 52000 ESH [4]. Many types of white ceramic have been tested (Astroquartz 2, Astroquartz 3 and Nexel Refrex 1210), the increase of the solar absorptance α_S varied from 353 % to 410% [4].

In summary, the optical properties (α_S, ϵ_t) of different kinds of surfaces are damaged more by exposure to UV-light than by electron/proton irradiation at least in relatively short distances to the Sun [3, 5]. However, according to the studies accomplished by Marco et al. [108] in a GEO orbit, electrons cause larger changes of optical properties only to white ceramic and silicone paints then UV-light together with proton irradiation.

In case of aluminized Kapton and MLI blankets sequential irradiation with UV-light and charge particles has shown than the UV-light causes the main contribution to changes of the α_S and ϵ_t [6]. Extreme environmental conditions like those which are present at Mercury distance to the Sun were carefully studied at ESA/ESTEC [4]. The growth of the α_S of white ceramic due to UV radiation was enormous. Unfortunately degradation effects due to particle irradiation were not investigated.

4.2 Blistering - formation of molecular Hydrogen bubbles

The presented here ideas and theoretical model (Subsection 4.2.2) have been published in a review scientific journal *Advances in Space Research* [17].

H_2-bubbles are metal pockets filled with Hydrogen molecular gas resulting from recombination processes in the metal lattice. Blistering occurs as irradiation damage. It changes the physical properties of the irradiated surface and increases the erosion rate [109]. As it is known from terrestrial laboratory experiments, that caps of bubbles lose thermal contact with the target body and, therefore, become overheated under intensive beams [109]. Growth of bubbles on a flat surface can be interpreted as the increase of surface roughness that causes the decrease of mirror reflectivity [109].

Degradation of structural properties of solids, caused by Hydrogen (referred to as embrittlement), plays an important role in materials physics [110]. Four general processes of the embrittlement have been proposed: formation of a hydride phase, enhanced local plasticity, grain boundary weakening, and bubble formation [110, 111].

H_2-bubbles form just below the metal surface. The tendency to form bubbles depends on: proton energy, time - integrated proton flux, temperature of the target, crystallographic orientation of the

irradiated surface and on impurities and defects in the sample [112]. The amount of Hydrogen retained in the sample is sensitive to the crystallographic orientation as well as to the diffusion rate [112].

Hydrogen atoms are much smaller than metal atoms, but they can introduce strain into a metal lattice when absorbed as interstitial ions [113, 114, 115]. They can also change the electronic structure of near neighboring metal atoms [114]. That causes an increase of the lattice energy. It may be decreased by the aggregation of the interstitial Hydrogen atoms into Hydrogen atom clusters, and then molecular Hydrogen bubbles [114]. Hydrogen could not agglomerate into H_2-clusters without the presence of vacancies. According to Damask [116] a vacancy is a missing atom in the metal lattice. Vacancies may be created by incident ions while penetrating the target metal. For Aluminum, numerical analysis performed with the SRIM software [95] have shown that a flux of 5 keV protons can induce 4 vacancies per one incident proton, while flux of 100 keV protons can induce up to 11 vacancies. The final number of bubbles depends also on the number of vacancies initially placed in the metal lattice [97], i.e. it depends crucially on the production process of the metallic surfaces. A single vacancy in Aluminum can trap up to twelve H atoms. For comparison, a vacancy in Iron can trap only up to six H atoms [110].

Formation of molecular Hydrogen bubbles takes place together with the so-called pitting formation. The pits are surface micropores that occur during proton irradiation of materials. The distribution of pits was found to be affected by particle energy, total flux, crystal orientation, and crystal substructure [97]. The surface density of pits increases with decreasing energy of incident particles. Thus, even a perfectly produced metallic surface that contains no vacancies will acquire a certain surface roughness as soon as it is exposed to solar proton irradiation.

According to experiments performed by many scientific groups, e.g. [97, 112, 117], there exist two critical parameters for the bubble formation: the total dose of protons and the temperature of a sample. The temperature range in which bubbles were observed on the foils is 288-573 K [97, 112]. Above 630 K, the diffusivity of H in Aluminum is so large that Hydrogen atoms escape from the metal lattice before they can form bubbles [117]. Depending on the experimental setup, the critical dose of protons above which the process occurs is $10^{16}...10^{17}$ H^+cm^{-2}. The blistering phenomenon was observed also after sample irradiation by H_2^+ ions. In that case the critical dose of ions above which the process appeared is $\sim 10^{18}$ H_2^+ cm^{-2}.

The procedure that was used to estimate the critical temperature (573 K) above which the process of bubble formation was stopped e.g. [97, 112] due to the bubble cracking mechanism was as follows. The Aluminum target was irradiated by a flux of protons at room temperature. When irradiation of the sample was stopped, the probe was heated up to higher temperatures. A significant increase of both, the surface density and sizes of the bubbles has been observed until the critical temperature was reached. That procedure, used by the authors, allows to capture more Hydrogen by the vacancies since during the irradiation, and at room temperature the vacancies will collect more Hydrogen than at elevated temperatures. Also a diffusion of Hydrogen in Aluminum at room temperature is much lower than at temperatures reaching ~ 570 K [93]. In space a probe is bombarded by the solar protons at the temperature which is related to its orbit. Therefore, the procedure presented by [97, 112] does not match the bubble formation mechanism under real space conditions.

A large set of proton irradiation tests has been made by Milacek et al. [97]. Rolled 99.999% Aluminum was used as target material. The energy range of incident protons varied from 10 to 200 keV. Aluminum samples were exposed to a flux of 1.5×10^{12} and 11.8×10^{12} H^+ cm^{-2} s^{-1} at room temperature. Some of the samples were annealed above 470 K. Depending on the experimental setup, the total dose of protons varied from 1.0×10^{16} H^+ cm^{-2} to 3.5×10^{17} H^+ cm^{-2}. Molecular Hydrogen bubbles were observed at room temperature after proton irradiation with energies lower than 70 keV. For higher proton energies bubbles appeared after annealing of the samples to approximately 470 K.

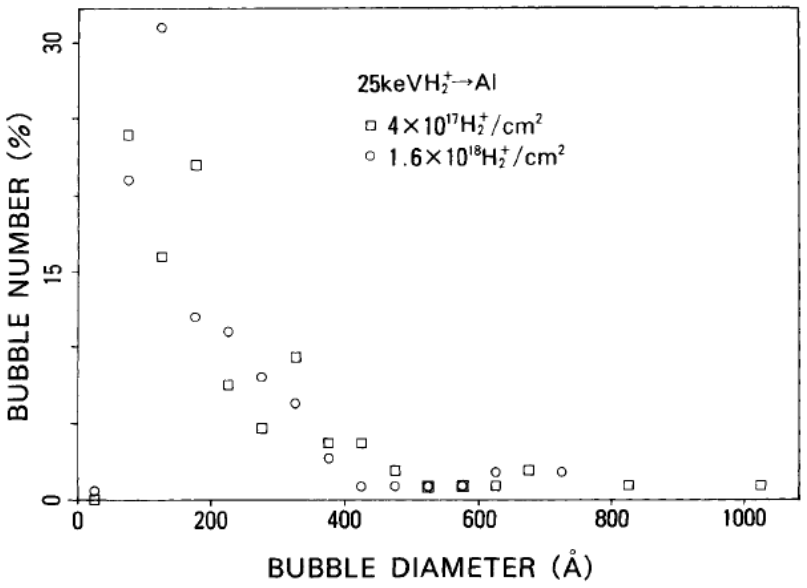

Figure 4.8: Diameter distribution of molecular Hydrogen bubbles on a surface of Aluminum. The target was irradiated by 25 keV H_2^+ ions with a fluence of 4×10^{17} H^+ cm^{-2} (squares) and 1.6×10^{18} H^+ cm^{-2} (cycles) [119].

The bubbles, once formed, were elongated along the rolling of the samples. Typical lengths of bubbles were 1.2 μm for samples irradiated at room temperature by 50 keV protons, and 117 μm for samples irradiated by 200 keV protons at 470 K. The higher the temperature of the sample, the larger the observable size of the bubbles.

An energetic and temperature threshold of formation of molecular hydrogen bubbles was measured by Daniels [112]. The Aluminum sample was irradiated by a flux of 100 keV protons. The total dose of protons was 10^{17} H^+ cm^{-2}. The sample was irradiated at a temperature of 300 K. Under these conditions no bubbles were observed. Afterwards, the sample was heated up to 570 K and a dense concentration of bubbles appeared.

Molecular Hydrogen bubbles were observed also on different materials than Aluminum. Copper, Tungsten, Palladium and Iron were investigated [109]. Bubbles are not forming on Tantalum and Vanadium. These metals are well known as *blistering-resistant* materials [109]. However, they are not suitable for space applications where the surface reflectivity plays a crucial role, e.g. in the solar sail propulsion technology since their reflectance is $\sim 50\%$ lower than that of Aluminum [118].

The size distribution of molecular Hydrogen bubbles was studied by Kamada et al. [119]. They irradiated Aluminum foils by a flux of 25 keV H_2^+ ions. The result is shown in Fig. 4.8, for a total fluence of 4×10^{17} H_2^+ cm^{-2} (squares) and 1.6×10^{18} H_2^+ cm^{-2} (cycles). The temperature of the specimen was hold at 300 K. Two samples have been irradiated. The first sample had a dimension of $20 \times 20 \times 0.1$ mm while the second one had a thickness of 5 μm. The majority of bubbles have diameters below 400 Å. The maximum number of bubbles, about 30% of the population, have a diameter of 180 Å.

Different results have been shown by Milcius et al. [117] who used as well H_2^+ ions as incident particles. The Aluminum foil of thickness of 5 μm has been irradiated by a flux of 1 keV H_2^+ ions, the total fluence of incident ions was 10^{18} H_2^+ cm^{-2}. As is seen in the Fig. 4.9, the diameter of bubbles at room temperatures (left panel) is in μm range. The largest bubble diameter is smaller than 10 μm.

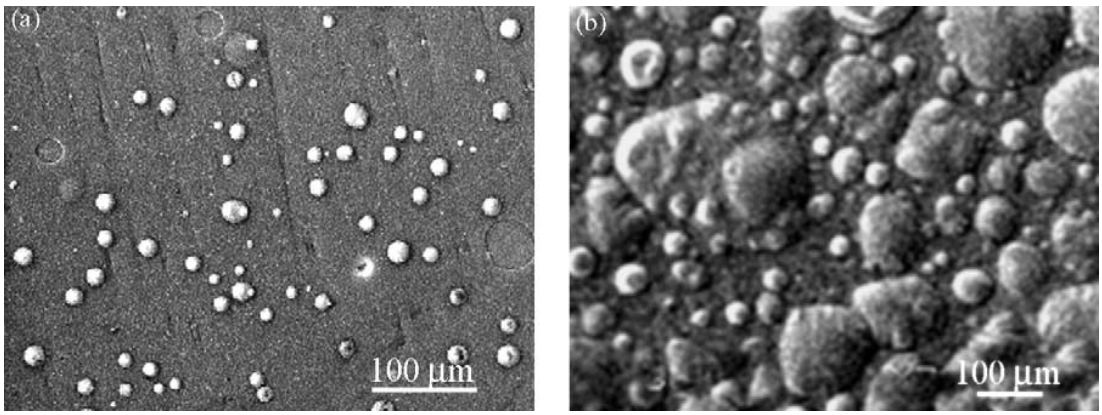

Figure 4.9: Aluminum irradiated with 1 keV H_2^+ ions. The left panel shows the sample at $T = 300$ K, while the right one at 450 K [117].

On the left panel, at $T = 450$ K it is seen that the diameter of some bubbles is even larger than 100 μm.

Hemispherical bubbles have been observed by Rozenek [120]. Hydrogen was filled into the samples by electrochemical charging. Current densities of 50 mA cm^{-2} were applied. The method is based on the principle that the sample is negatively and the gas is positively charged. Then a flux of ions is generated. Bubbles were observed on a surface of 99.999% Aluminum samples with thickness of 2 mm. A wide variation in the size from large (tens of micrometers in diameter) to very small (nanometers in diameter), in the distribution, in the density, and in the geometrical shapes of the surface bubbles were observed [120]. A single bubble of Rozenek's experiments is presented in Fig. 4.10. The picture is taken by use of the Scanning Electron Microscope (SEM) method. The Aluminum sample was electrochemically charged for 24h at room temperature. The method of electrochemical charging, however, can serve as a model of bubble creation under space conditions.

4.2.1 Formation of bubbles under space conditions

Devices, while operating in the interplanetary space, are exposed to solar wind and electromagnetic radiation. The solar wind, as the Sun's corona, is essentially made up of electrons and protons plus a small proportion of heavier ions, and it carries a magnetic field. Particles and fields are intimately coupled in plasmas [121].

Extraterrestrial Sun observatories measure a few key solar wind parameters, e.g.: components of proton and electron velocity, their mean number density as well as components of the magnetic field.

Fig. 4.11 shows solar proton and electron fluxes at 1 AU distance from the Sun. Proton fluxes are calculated by use of the data collected by the SOHO (since 1995) and the ACE (since 1997) satellites. The OMERE as well as the SPENVIS databases were also considered.

When a probe is irradiated in space, it collects incident ions from a wide energy range. The range depends on the type and the thickness of an irradiated material. The thiner the target material, the less ions stuck in it. Therefore, there must exist a critical energy of incident ions (E_c) above which they pass through the material. Hence, the integrated proton flux over the energies is:

$$I_E = \sum_{E_{min}}^{E_c} I(E), \tag{4.10}$$

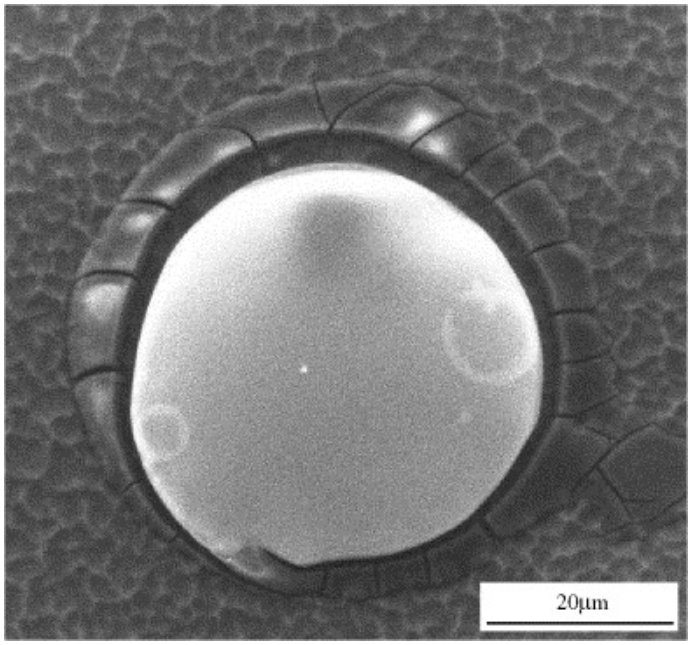

Figure 4.10: Bubble diameter: 50 μm, sample temperature 300 K [120].

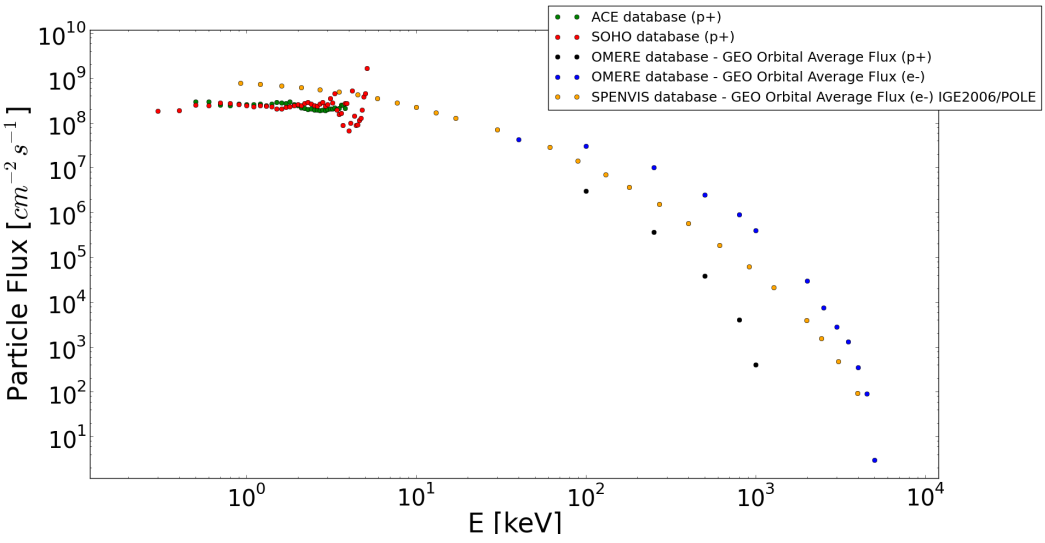

Figure 4.11: Flux of solar protons and electrons as a function of energy. Data are taken from the SOHO, ACE, OMERE, and SPENVIS databases.

where $E_{\min}$ is the ion's lowest energy recorded by the satellite's detector system. The I_{E} values are presented in the Table 4.1. To calculate the fluxes the ACE database was used.

To estimate the flux of solar protons I_{d} at distance d from the Sun, the following relation can be used:

$$4\pi(1\mathrm{AU})^2 \times \mathrm{I_E} = 4\pi \mathrm{d}^2 \times \mathrm{I_d}. \tag{4.11}$$

Growth of molecular Hydrogen bubbles will be possible in the interplanetary space if the criterion

Table 4.1: Integrated proton fluxes over the energies for 1 AU distance orbit from the Sun.

E_c [keV]	$I_E \times 10^{13}$ [$p^+ cm^{-2} s^{-1}$]
1.0	0.44
1.5	0.68
2.0	0.91
2.5	1.06
3.0	1.12
4.0	1.14
5.0	1.15
9.0	1.15

of the minimum dose of protons is fulfilled. The temperature of the sample has to be high enough to start the bubble formation, but not too high to lose Hydrogen much too rapidly due to the high diffusivity of Hydrogen in metals.

Under the simplifying assumption that the Sun generates only mono-energetic 5 keV protons, the criterion of minimum dose of protons will be fulfilled after 116 days for 1 AU distance orbit from the Sun. Obviously, taking into account proton fluxes from the whole energy range, the criterion will be fulfilled much earlier.

The temperature of a foil placed in a given distance d from the Sun can be calculated by:

$$T = \left(\frac{A_a}{A_e} \frac{\alpha_S}{\epsilon_t} \frac{H_{Sun}}{\sigma_{SB}} \right)^{\frac{1}{4}}, \qquad H_{Sun} = \frac{1 \text{ SC}}{d^2}. \tag{4.12}$$

Here, A_a is the area of the sample which absorbs the electromagnetic radiation, while A_e is the area which emits the heat by radiation. Hence, the ratio $\frac{A_a}{A_e}$ equals 0.5. σ_{SB} is the Stefan-Boltzmann constant. *SC* states for Solar Constant. The thermo-optical parameters have been provided by the manufacturer of the Upilex − S® foil, the UBE company. Solar absorptance α_S and normal emittance ϵ_t are 0.093 and 0.017, respectively. The foil temperature as a function of distance from the Sun is represented by solid line in Fig. 4.12. Note, that the heat released by stopped protons is negligible small in comparison to the Sun's input. The red area (570 - 300 K) is the temperature range in which the bubble formation has been confirmed by the terrestrial laboratory experiments. Unfortunately, commonly used experimental procedures to estimate the maximum temperature at which the bubble formation is stopped, are not suitable for the real space conditions. The real critical temperature is lower, and it has been estimated to 383 K. The dark-red area (below 383 K) represents temperatures at which the bubble formation has been confirmed by the experimental findings presented in this thesis, see Section 5.1. The bubble growth continues even when the probe is moving outwards from the Sun ($\geq$ 2.5 AU, grey area). Obviously, at larger distances the bubble growth slows down, since the probe is being bombarded by the smaller proton fluxes, see Eq. 4.11.

4.2.2 Thermodynamic approach to blistering process

In the following a thermodynamic model of bubble growth is proposed. The model is based on the assumption that the growth proceeds quasi-static i.e. during a j^{th} period of time Δt_j a small portion of H_2-molecules, $N_{H_2,i,j}$, is added to the i^{th} bubble and a thermodynamic equilibrium is established.

For simplicity it is assumed that a single bubble is a half of a sphere with a radius of r_i. The gas within a bubble behaves to a good approximation like an ideal gas:

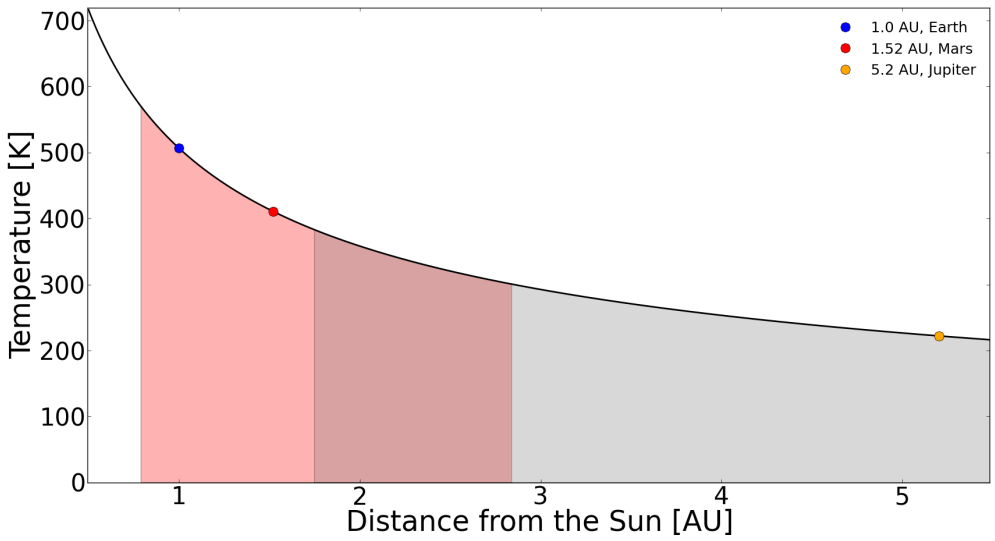

Figure 4.12: Temperature of the Upilex – S® foil covered on both sides with 100 nm vacuum deposited Aluminum layer as a function of the distance from the Sun. The red area represents temperature range in which the bubble formation was reported in the literature. The dark-red area is the temperature range in which the formation has been confirmed by studies presented in this thesis.

$$p_{\mathrm{i}} V_{\mathrm{i}} = \sum_{\mathrm{j}}^{\mathrm{N}} N_{\mathrm{H_2,i,j}} k_{\mathrm{B}} T, \tag{4.13}$$

where p_{i} is the pressure of the gas, k_{B} is the Boltzmann constant, T denotes the temperature of the sample, N is the number of time steps up to a given state of bubble growth, hence the irradiation time of the sample after N steps is $N \times \Delta t_{\mathrm{j}}$.

The number of recombined H atoms, subtracted by those which diffuse from the sample out ($N_{\mathrm{diff,j}}$) is:

$$\begin{aligned} N_{\mathrm{H,j}} &= I_{\mathrm{E}} \Delta t_{\mathrm{j}} A (1 - BS) + N_{\mathrm{diff,j}}, \\ N_{\mathrm{diff,j}} &= -D_{\mathrm{H}}(T) \frac{\zeta_{\mathrm{H,j}}}{d_{\mathrm{PR}}(E)} (A - A_{\mathrm{b}}) \Delta t_{\mathrm{j}}. \end{aligned} \tag{4.14}$$

The term $D_{\mathrm{H}}(T) \frac{\zeta_{\mathrm{H,j}}}{d_{\mathrm{PR}}(E)}$ determinates how much Hydrogen diffuses from the sample out (per unit area and time). Therefore, by dimension it is a flux of outflowing Hydrogen from the specimen. Its constant value results from the following fact. The model assumes that the sample is exposed to the protons having kinetic energies from eVs to 8 keV. According to the data (see, Fig. 4.11), the magnitude of the proton flux remains almost constant for the considered energy range. Therefore, the sample is uniformly populated by the protons (H atoms after recombination) to a depth of d_{PR}. The d_{PR} is calculated for the fastest protons. Therefore, there is no differentiation of Hydrogen concentration with respect to the depth.

In the Eq. 4.14 A is the area of the sample irradiated by the protons, A_{b} is the area of the sample covered by the bubbles. BS is the factor of backscattered ions. If BS is 1 then all of the incident ions are backscattered. If BS is 0 then all of the incident ions penetrate the target. $D_{\mathrm{H}}(T)$ is the diffusion

coefficient for H atoms in a given material, $\zeta_{\mathrm{H,j}}$ is the number density of H atoms which may diffuse through the lattice in the j^{th} period of time, $d_{\mathrm{PR}}(E)$ is the so-called projected range. It is defined as an average value of the depth to which a charged particle will penetrate in the course of slowing down to rest. This depth is measured along the initial direction of the particle, and it depends on the kinetic energy of the particle [25].

The number of Hydrogen molecules added in the j^{th} period of time to the i^{th} bubble $N_{\mathrm{H_2,i,j}}$ is constant and then given by:

$$\begin{aligned} N_{\mathrm{H_2,i,j}} &= 0.5 G_{\mathrm{i}} N_{\mathrm{H,j}}\ \eta_{\max}(s)\ \xi, \\ \sum G_{\mathrm{i}} &= 1, \qquad \dim \mathrm{G} = \mathrm{N_B^T}. \end{aligned} \tag{4.15}$$

Here 0.5 denotes that a single H_2 molecule consists of two H atoms, G is a matrix, its role is to redistribute certain number of H_2 molecules into the bubbles. The input pattern of H_2 molecules into the bubbles follows experimental findings of Kamada et al. [119]. $N_{\mathrm{B}}^{\mathrm{T}}$ is the total number of bubbles on the irradiated sample. While 100% of protons recombine into H atoms in the metal lattice, only a part of them recombine to H_2 molecules [122]. Hence the $\eta_{\max}(s)$ coefficient is the ratio between the number of H_2-molecules and the H-atoms in the lattice. The H_2 molecule is formed when electrons of two H atoms have anti-parallel spin s, otherwise the molecule cannot be created. Therefore, at most half of the H atoms can form H_2 molecules, hence $\eta_{\max}(s) = 0.5$. Not all of the H_2-molecules will merge into H_2-clusters and finally form H_2-bubbles. Thus, the coefficient ξ denotes the ratio of the number of H_2-molecules inside and outside the bubbles.

The first step to estimate the radius of the i^{th} bubble is to calculate the Helmholtz free energy of the whole configuration, F_{config}. Since the free energy is an additive quantity, the total free energy of bubble formation is a sum of following quantities: free energy of H_2 gas inside the i^{th} bubble ($F_{\mathrm{gas,i}}$), of the metal surface deformation ($F_{\mathrm{md,i}}$) caused by the bubble growth itself, of the surface free energy ($F_{\mathrm{surf,i}}$) of the bubble cap, of the free energy of H_2-molecules ($F_{\mathrm{H_2}}$) and of H-atoms (F_{H}) placed outside the bubbles but within the metal lattice. The Helmholtz free energy of the whole configuration described above is then:

$$F_{\mathrm{config}} = \sum_{i}^{\mathrm{N_B}} \left(F_{\mathrm{gas,i}} + F_{\mathrm{md,i}} + F_{\mathrm{surf,i}}\right) + F_{\mathrm{H_2}} + F_{\mathrm{H}}. \tag{4.16}$$

The next step is to estimate the free energy of the i^{th} bubble. It consists of the free energy of the gas filled in the bubble, the free energy of metal deformation, and of the bubble cap surface free energy.

Using the thermodynamic relation between gas pressure and its Helmholtz free energy $p = \left(\frac{\partial F}{\partial V}\right)_T$ together with the equation of state Eq. 4.13, the free energy of a gas within the i^{th} bubble is:

$$F_{\mathrm{gas,i}} = -\sum_{\mathrm{j}}^{\mathrm{N}} N_{\mathrm{H_2,i,j}} k_{\mathrm{B}} T \ln\left(\frac{V_{\mathrm{max,i}}}{V_{\min}}\right), \tag{4.17}$$

where $V_{\mathrm{max,i}}$ is the maximum volume of a given bubble. The model assumes that two H_2 molecules form the smallest ("initial") possible bubble, its volume is denoted by $V_{\min}$. The radius of such a bubble is approximately 1.45 Bohr radii [123]. Every bubble will crack if the pressure of the gas inside is higher than the pressure exerted by the metal deformation of the cap. The relation between the pressure of the gas, surface tension σ_{S}, and the bubble radius corresponding to $V_{\mathrm{max,i}}$ is [124]:

$$p_{\text{gas, insite bubble}} - p_{\text{outside bubble}} = \frac{2\sigma_{\mathrm{S}}}{r_{\mathrm{max,i}}}. \tag{4.18}$$

Since the sample is placed in vacuum, the pressure outside the bubble is set to zero.

The free energy of metal deformation $F_{\mathrm{md,i}}$ caused by the gas pressure inside the bubble with radius r_{i} can be found in [125], and is given by:

$$F_{\mathrm{md,i}} = \frac{4\pi}{3}\frac{r_{\mathrm{i}}^3(1+\gamma)}{E_{\mathrm{Y}}}p_{\mathrm{i}}^2. \tag{4.19}$$

Here γ is the Poisson coefficient, i.e. ratio of transverse to axial strain of a sample material, E_{Y} is the Young's module.

The free energy of a surface of a cap of the i$^{\mathrm{th}}$ bubble is given by [126]:

$$F_{\mathrm{surf,i}} = 4\pi r_{\mathrm{i}}^2\sigma_{\mathrm{S}}(T). \tag{4.20}$$

The Helmholtz free energy of the H_2-molecules located at certain positions in the metal lattice but outside the bubbles is calculated in the form $F = E_{\mathrm{int}} - TS$. Where E_{int} is the internal energy of molecules/atoms located at certain positions in the metal lattice. Applying the statistical definition of the entropy S, this free energy is:

$$\begin{aligned} F_{\mathrm{H_2}} &= \left(N_{\mathrm{H_2}}^{\mathrm{T}} - \sum_{\mathrm{i}}^{N_{\mathrm{B}}^{\mathrm{T}}}\sum_{\mathrm{j}}^{\mathrm{N}} N_{\mathrm{H_2,i,j}}\right) \\ &\times \left[\epsilon_{\mathrm{H_2}} + k_{\mathrm{B}}T\ln\left(\frac{N_{\mathrm{H_2}}^{\mathrm{T}} - \sum_{\mathrm{i}}^{N_{\mathrm{B}}^{\mathrm{T}}}\sum_{\mathrm{j}}^{\mathrm{N}} N_{\mathrm{H_2,i,j}}}{N_0}\right)\right], \end{aligned} \tag{4.21}$$

where $N_{\mathrm{H_2}}^{T}$ is the total number of H_2 molecules inside the sample, $\epsilon_{\mathrm{H_2}}$ is the binding energy of H_2 molecule to a vacancy. A detailed derivation of the Eq. 4.21 is presented in Appendix D.1. N_0 is the number of lattice sites, which can be expressed by:

$$N_0 = N_{\mathrm{A}}d_{\mathrm{PR}}\frac{A}{M_{\mathrm{u}}}, \tag{4.22}$$

where N_{A} is the Avogadro's number. M_{u} is the molar mass of the sample's material.

The Helmholtz free energy of H atoms located at certain positions within the metal lattice is:

$$F_{\mathrm{H}} = \left(N_{\mathrm{H}}^{\mathrm{T}} - 2N_{\mathrm{H_2}}^{\mathrm{T}}\right)\left[\epsilon_{\mathrm{H}} + k_{\mathrm{B}}T\ln\left(\frac{N_{\mathrm{H}}^{\mathrm{T}} - 2N_{\mathrm{H_2}}^{\mathrm{T}}}{N_0}\right)\right], \tag{4.23}$$

where ϵ_{H} is the migration energy of the H atom in the metal lattice, and $N_{\mathrm{H}}^{\mathrm{T}}$ is the total number of H atoms in the sample. A detailed derivation of the Eq. 4.23 can be found in Appendix D.2.

Since now each term of the Eq. 4.16 is determined, the next step is to estimate the radius r_{i} of the i$^{\mathrm{th}}$ bubble at given time t. This will be achieved by assuming that the process of bubble growth is quasi-static, i.e. during each j$^{\mathrm{th}}$ time step Δt_{j} a small portion of H_2 molecules is merged to the i$^{\mathrm{th}}$ bubble and the thermodynamic equilibrium is rapidly re-established:

$$\frac{\partial F_{\mathrm{config,i}}}{\partial N_{\mathrm{H_2,i,j}}} = 0. \tag{4.24}$$

This condition leads to the following fifth order equation for r_i:

$$8\pi\Xi_{\mathrm{i,j}}\sigma_\mathrm{S}(T)r_\mathrm{i}^5 - H_\mathrm{i}r_\mathrm{i}^4 + \tfrac{3}{\pi}\tfrac{1+\gamma}{E_\mathrm{Y}}\left(\sum_\mathrm{j}^\mathrm{N} N_{\mathrm{H_2,i,j}}\right)k_\mathrm{B}^2T^2 \times \left[2Nr_\mathrm{i} - 3\Xi_{\mathrm{i,j}}\sum_\mathrm{j}^\mathrm{N} N_{\mathrm{H_2,i,j}}\right] = 0, \tag{4.25}$$

$\Xi_{\mathrm{i,j}}$ is defined below in Eq. 4.27, H_i denotes the abbreviation:

$$H_\mathrm{i} = -\frac{\partial F_{\mathrm{gas,i}}}{\partial N_{\mathrm{H_2,i,j}}} - \frac{\partial F_\mathrm{H}}{\partial N_{\mathrm{H_2,i,j}}} - \frac{\partial F_{\mathrm{H_2}}}{\partial N_{\mathrm{H_2,i,j}}}. \tag{4.26}$$

The derivatives of the Helmholtz free energy, of the gas inside the i$^\mathrm{th}$ bubble, of metal deformation caused by the bubble, of the i$^\mathrm{th}$ bubble cap surface, of H_2 molecules, and of H atoms with respect to the number of H_2 molecules added at the j$^\mathrm{th}$ time step to the i$^\mathrm{th}$ bubble are presented in Appendix D.3.

A realistic model of bubble radius growth, $\Xi(i,j)$, can be estimated by following Gedankenexperiment. Obviously at the beginning of the bubble growth process, the differential increase of the bubble radius is higher than at its end. It is implied, that the number of H_2 molecules in the system is conserved and at each time step one of them merge into a bubble. After Δt the bubble consists of $2H_2$ molecules, hence the number of molecules increases by 50%. At the time $2\Delta t$ the bubble consists of $3H_2$ molecules, hence the number increase is now 33.3%, and so on. Therefore Ξ is:

$$\Xi_{\mathrm{i,j}} = \frac{\Delta r_\mathrm{i}}{\Delta N_{\mathrm{H_2,i,j}}} = j^\alpha r_{\mathrm{i},0}, \qquad \alpha = \frac{1}{3} \tag{4.27}$$

The exponent α is a model parameter of the bubble growth. The value $\frac{1}{3}$ corresponds to the Gedankenexperiment presented above. However, the true value of the α parameter differs from that. In the process of bubble growth, particles (the Hydrogen) are added to the system i.e. the probe is permanently irradiated by the protons, they penetrate the target and recombine to the Hydrogen. On the other hand, both, due to the diffusion process and bubble cracking, some Hydrogen atoms leave the system. Therefore, the number of Hydrogen atoms in the system is not conserved. Hence, a series of experiments have been performed to estimate a realistic α parameter, results are presented in Section 5.1.

4.2.3 Reflectivity of a metallic foil covered with bubbles

The momentum transfer of a photon to an ideal reflecting surface is given by $\Delta q = 2q\cos\theta$, where the factor 2 is just in accordance with specular reflectivity. Certainly, the surface quality will suffer during the irradiation with protons from progressing bubble formation. At time $t = 0$ the foil has not been exposed to the electromagnetic radiation and/or charged particles, and is considered to be a perfect mirror with the reflectivity of $R = 1$. It means that all of the incident light rays are reflected perfectly, no light ray is absorbed or diffusively reflected by the target. Later, when the foil has been irradiated by a flux of protons and molecular Hydrogen bubbles have been formed on its surface, the reflectivity of the degraded foil will be reduced. This deterioration is calculated in the following way: the foil is covered by a grid with a fixed single cell size of $\epsilon_\mathrm{cell} \times \epsilon_\mathrm{cell}$, see Fig. 4.13. The reflectivity of a single cell is by definition $\frac{\Delta q}{\Delta q_\mathrm{max}}$, where Δq is momentum transfer of a photon to the i$^\mathrm{th}$ cell of the degraded foil, while $\Delta q_{\mathrm{max,i}}$ is the momentum transfer of a photon to the i$^\mathrm{th}$ cell of a perfect mirror.

Therefore, taking into account all cells, one has:

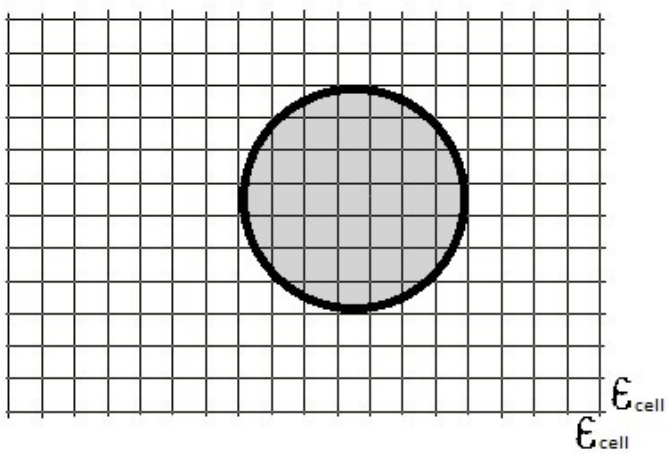

Figure 4.13: A fraction of the foil with one spherical bubble is shown. The size of a single cell of the grid is $\epsilon_{\rm cell} \times \epsilon_{\rm cell}$.

$$\Delta R = \frac{\sum_{\rm i}^{\rm N_{cell}} \Delta q_{\rm i}}{\sum_{\rm i}^{\rm N_{cell}} \Delta q_{\rm max,i}}. \tag{4.28}$$

Here $N_{\rm cell}$ is the number of cells. The path of photons is directed parallel to the foil surface normal. Therefore, at time $t = 0$ the foil was a perfect mirror without surface imperfections and $\theta_{\rm i} = 0$. Later, when the surface is populated with bubbles, $\theta_{\rm i}$ will vary between 0^o and 90^o. Thus, Eq. 4.28 reduces to:

$$\Delta R = \frac{\sum_{\rm i}^{\rm N_{cell}} 2q \cos\theta_{\rm i}}{N_{\rm cell} \times 2q} = \frac{\sum_{\rm i}^{\rm N_{cell}} \cos\theta_{\rm i}}{N_{\rm cell}}. \tag{4.29}$$

Chapter 5

Experimental and numerical studies of molecular Hydrogen bubble formation

5.1 Validation of the thermodynamic model - proton dose dependency on bubble formation mechanism

I performed the following set of experiments to validate the thermodynamic model. The model together with its validation have been published in a review scientific journal *Advances in Space Research* [17]. Three probes (A1, A2, and A3) were exposed to a flux of 2.5 keV protons, each one with longer irradiation time, see Table 5.1, where t_S is a number of days in space until a probe will collect a given dose of protons. Results are shown in Fig. 5.1. From top to bottom, the pictures correspond to the probes A1, A2, and A3, respectively. Average radii of bubbles have been estimated to 0.18 ± 0.05 μm, 0.19 ± 0.05 μm, and 0.2 ± 0.05 μm for probe A1, A2, and A3, respectively. There is a strict correlation between a dose of protons and the average bubble size for a given population. The higher the proton dose, the larger the bubble sizes. Examining the electron microscope pictures, the surface density of bubbles has been estimated to $\sim 10^8$ cm^{-2}.

Table 5.1: Test parameters for samples A1, A2, and A3.

Probe symbol	T [K]	E [keV]	D [p$^+$ cm^{-2}]	t_S [days]	t_{lab} [days]	$\frac{t_S}{t_{lab}}$
A1	323.0	2.5	7.8×10^{17}	4.8	7.9	0.6
A2	323.0	2.5	8.2×10^{17}	5.0	5.5	0.9
A3	323.0	2.5	1.3×10^{18}	7.9	10.9	0.7

Flux of protons was chosen in a way that $f_{lab}^{p^+} \geqslant f_S^{p^+}$. That choice has an important meaning. If flux of protons generated in the laboratory is similar to that in space then the outcoming irradiation results also correspond to that in space. However, it must be pointed out that in laboratory the probe can be irradiated by monoenergetic protons, while in the interplanetary space, the probe is exposed to a flux of protons in the whole energy range, see Fig. 4.11. The presented here degraded foils can be treated as a reference ones in comparison to future aging tests.

The next tests are performed for proton fluxes $f_{lab}^{p^+} > f_S^{p^+}$. Such choice is from technical and economical point of view necessary. However, there exist a danger that $f_{lab}^{p^+}$ is too high and that the outcoming irradiation results are unphysical. In the context of bubble formation the overestimated proton flux may cause following unwonted side effects. The increased number of incoming protons

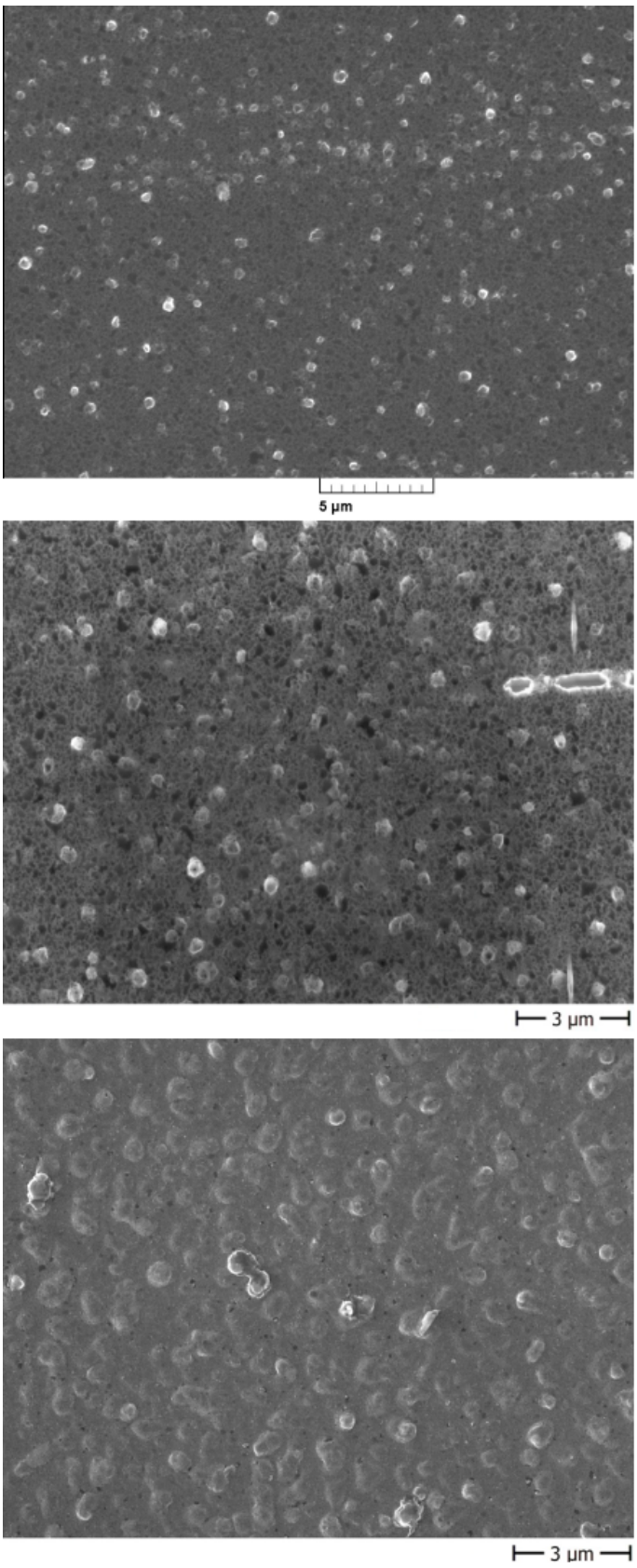

Figure 5.1: Electron microscope pictures of probes A1 (top), A2 (middle), and A3 (bottom).

may dissociate the H_2 molecules within the bubbles and effectively decrease their size. Higher proton flux may also increase diffusion of H atoms within the bombarded metal lattice. Each proton brings a small portion of energy which is transformed in the metal lattice into the heat (in the literature such effect is called *the thermal spike*, see e.g. [127]). Local temperature increase rise the mobility of H atoms in the lattice, as a result more H atoms may escape from the sample out (such effect is called *radiation simulated diffusion*, see e.g. [128]). Therefore, the experimental parameters should be chosen with great care.

For numerical simulation a $10\mu\text{m} \times 10\mu\text{m}$ foil was specified. That choice allows to simulate a smaller number of bubbles, i.e. it decreases the computation time of the simulation. It implies also an important assumption that surface arrangement of the bubbles is isotropic i.e. any $10\mu\text{m} \times 10\mu\text{m}$ area of the irradiated sample is indistinguishable. Table 5.2 collects all of the model parameters used in the simulation. The first set of parameters characterize mechanical and thermo-optical properties of vacuum deposited Aluminum on UBS's Upilex $-$ S® foil. Second set specifies values of the parameters which have been used to fit the model to the experimental data presented here.

To fit the proper gradient of bubble growth, the α parameter was set to 0.6, see Eq. 4.27. Comparison of the average bubble size of the experimental and numerical findings are drawn in the top plot of the Fig. 5.2. The ξ parameter was set to 0.98. It determines the height of the curve. A decrease of the specular reflectivity of the foil as a function of time is shown in the bottom plot of the Fig. 5.2. The decrease of the reflectivity is 3.0, 3.2, and 4.6 % in comparison to the non-irradiated foil for 4.75, 5.0, and 7.9 t_S, respectively. At the end of the simulation, the decrease of the reflectivity is 8 %. Clearly, the larger the bubble sizes, the larger the specular reflectivity decrease ΔR in comparison to the non-irradiated foil. A distribution of the bubbles at three different time steps: 4.8, 5.0 and 7.9 t_S is shown in Fig. 5.3. During time, the probe collects higher dose of protons, therefore, the distribution drifts i.e. size of bubbles increases.

Additionally, a surface morphology of probe A3 has been investigated. Fig. 5.4 presents it's surface height-profile. Three different positions have been pointed out (marked as red cross) to show a typical height of a bubble as well as cavities which remain due to proton irradiation.

Table 5.2: Model parameters

Symbol	Value	Description
ϱ	2.7 [g cm^{-3}]	Al density
M	26.98 [g mol^{-1}]	Al molar mass
E	69×10^{10} [dyn cm^{-2}]	Al Young modulus
γ	0.33	Al Poisson coefficient
ϵ_H	0.52 [eV]	H migration energy in the Al lattice [93]
ϵ_{H_2}	0.06 [eV]	H_2 binding energy to a vacancy in Al [110]
α_S	0.093	solar absorptance
ϵ_t	0.017	normal emittance
BS	0.02	H^+ back scattering factor [95]
A	100 [μm^2]	irradiated area
T	323 [K]	sample's temperature
$\eta_\text{max}(s)$	0.5	$\frac{\text{H}_2 \text{ lattice}}{\text{H lattice}}$ ratio
ξ	0.98	$\frac{\text{H}_2 \text{ bubbles}}{\text{H}_2 \text{ lattice}}$ ratio
α	0.6	bubble growth parameter
N_B	10^8 [cm^{-2}]	number of bubbles per unit area

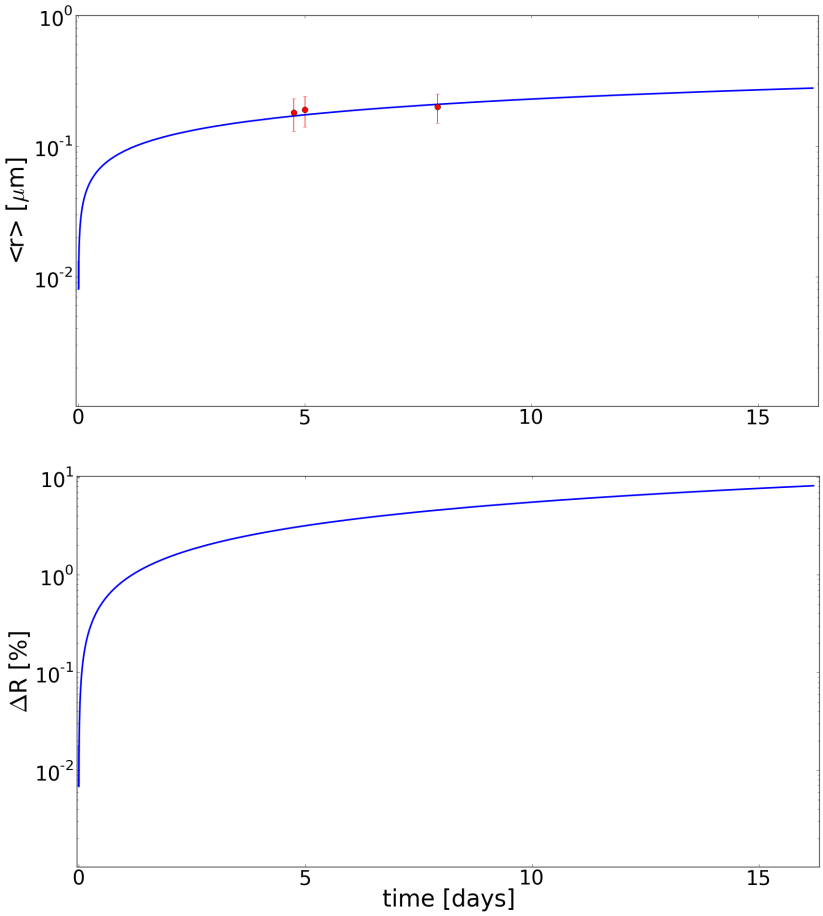

Figure 5.2: Time evolution of an average bubble radius from the population (top plot), specular reflectivity decrease due to bubble growth (bottom plot).

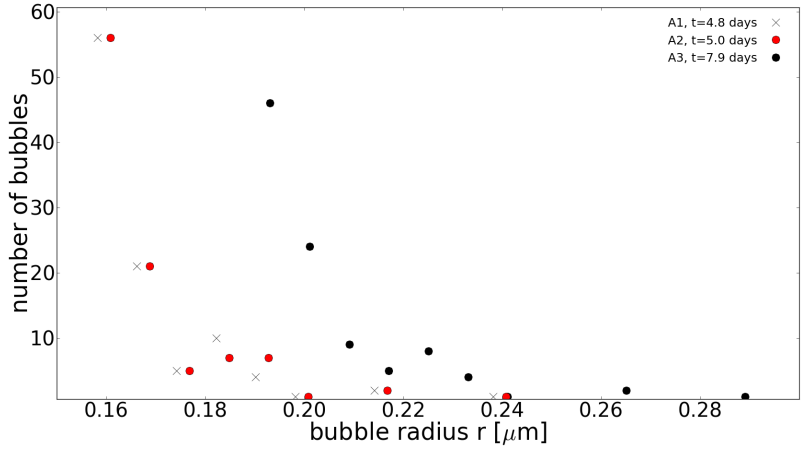

Figure 5.3: Bubble size distribution at a 100 μm^2 sample at three different time steps: 4.8, 5.0, and 7.9 t_S.

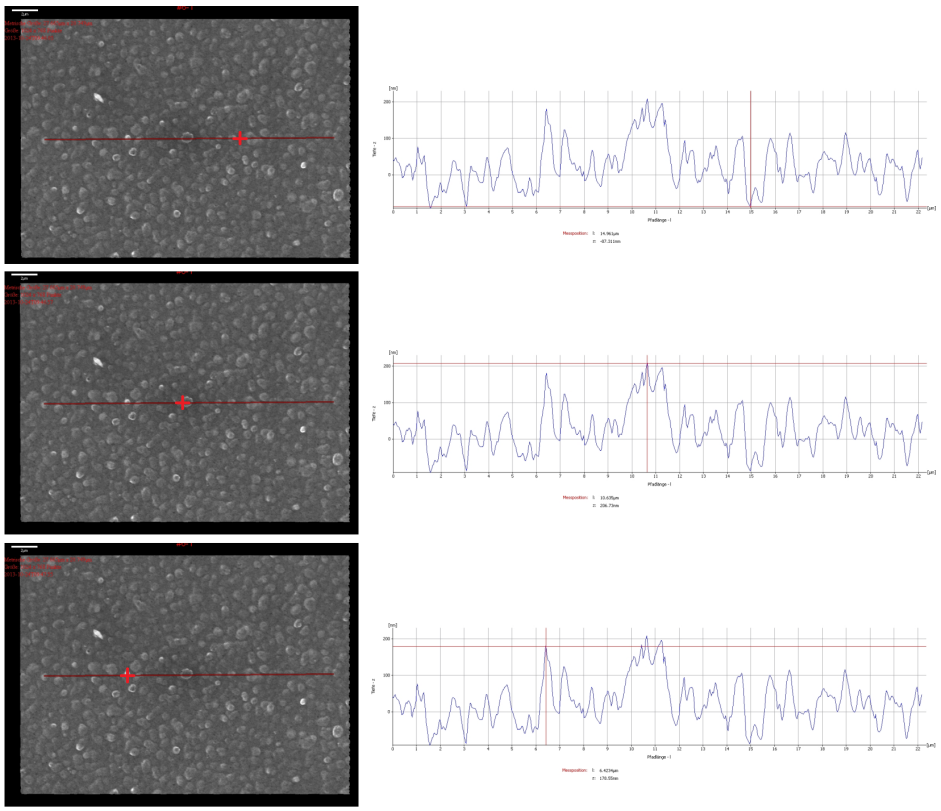

Figure 5.4: Three different positions on the probe A3 are shown. Top picture indicates a cavity on the surface, while the middle and the bottom pictures the height of selected bubbles.

5.2 Proton kinetic energy dependency on bubble formation mechanism

Influence of protons kinetic energy on bubble formation mechanism was considered. Two probes were irradiated by a flux of protons at the temperature of 300 K. That temperature corresponds to a distance of 2.85 AU from the Sun, see Fig. 4.12. Probe B1 was bombarded by 2.5 keV protons, while probe B2 by 6.0 keV protons. Probe B2 was exposed longer to the proton flux than probe B1. It collected a total dose of 5.9×10^{17} p^+ cm^{-2}, while probe B1: 4.3×10^{17} p^+ cm^{-2}. Test parameters are summarized in Table 5.3. Morphological studies of both specimens were made by use of the electron microscope. Results are presented in Fig. 5.5. The left picture shows probe B1, while right one the probe B2. Clearly, only the sample B1 was populated by the bubbles. Sample B2 does not exhibit the bubble formation phenomenon. Small dark points seen on the picture are the pits i.e. small holes created due to proton irradiation. Note that both pictures were taken with different magnification.

For 6 keV protons approx. 67% stuck in the Al lattice at average projected range of 77 nm [25], while rest of them travel through Al and degrade the Upilex part of the foil. The reason that the surface was not populated by the bubbles is due to low proton dose. For longer irradiation times the recombined H atoms and H_2 molecules would increase their concentration near by the surface and therefore form the bubbles.

The experiment brought also an important question. It is well known [129, 130] that bare Kapton/Upilex after proton irradiation loose N, O, and H as molecular gas while C remains in the structure. In the situation that the Upilex foil is covered by thin Al layer the formed N, O, and H molecular gas is blocked by the Aluminum. Therefore, the amount of gas should increase between both structures (between Al and Upilex). The open question is: how the formed gas influences the bubble formation? To answer that question, the probe should be exposed to higher proton fluxes than considered here.

Table 5.3: Test parameters for probes B1 and B2.

Probe symbol	T [K]	E [keV]	D [p^+ cm^{-2}]	t_S [days]	t_{lab} [days]	$\frac{t_S}{t_{lab}}$
B1	300.0	2.5	4.3×10^{17}	3.6	5.1	0.7
B2	300.0	6.0	5.9×10^{17}	4.9	1.8	2.7

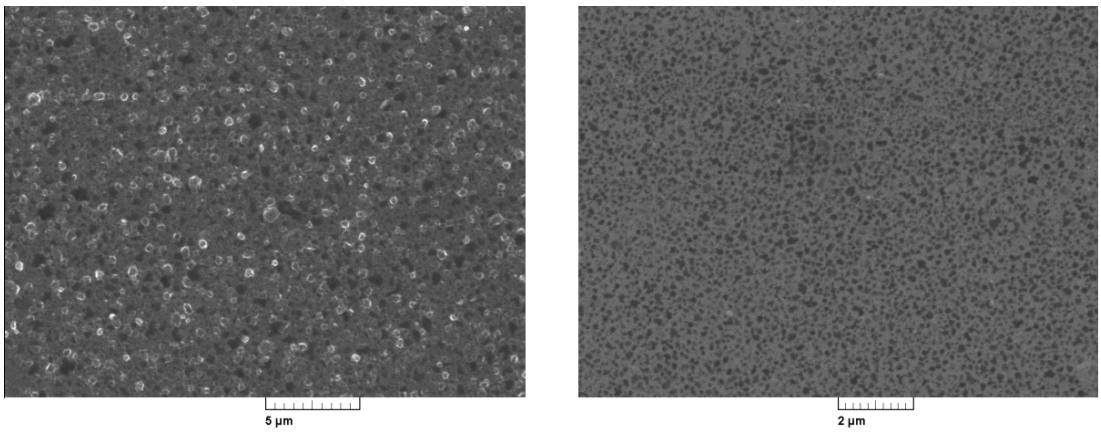

Figure 5.5: Electron microscope pictures of probes B1 (left) and B2 (right).

5.3 Influence of the temperature on bubble growth dynamics

Next, temperature influence on the bubble growth dynamics was considered. Three probes were exposed to proton flux. Since CIF's linear proton accelerator works in two modes i.e. high proton fluxes are achievable above 10 keV of protons' kinetic energy (see Table 3.1), the 10 keV protons were chosen. That choice implies a following issue. Since standard foil used for the tests has an Aluminum thickness of 100 nm, the 10 keV protons will pass through Al and stuck within the Upilex structure. Therefore, to study only protons - Al-ions interactions, the Al-layer of the foil should be thicker. The thickness of 1 μm was chosen. Test parameters are stored in Table 5.4.

As previous, morphological tests were performed by use of the electron microscope. Probe C1, irradiated at the temperature of 338 K, is shown in the Fig. 5.6. Except of bubbles with a diameter of $\lesssim 1\mu$m, the studies brought an unexpected result. A few large bubbles with diameter larger than 400μm appeared on the surface. The top picture shows such a bubble. The central circle-structure is magnified in the middle picture. Small bubbles surround the big ones (see top picture, Fig. 5.6). The small bubbles are shown in the bottom picture of the Fig. 5.6. Their sizes correspond to theoretical

Table 5.4: Test parameters for samples C1, C2, and C3.

Probe symbol	T [K]	E [keV]	D [p^+ cm^{-2}]	t_S [days]	t_{lab} [days]	$\frac{t_S}{t_{lab}}$
C1	338	10.0	2.65×10^{18}	13.4	1.9	7.0
C2	358	10.0	2.65×10^{18}	10.7	3.9	2.7
C3	383	10.0	2.65×10^{18}	8.2	1.9	4.3

predictions of the thermodynamic model. The large bubbles may grow in lattice positions where non-Aluminum atoms/molecules are present. Such atoms may join the material during the production process. It is well known that any kind of lattice symmetry brake, such as vacancies or non-host atoms/molecules accelerate the bubble growth [112].

The large bubbles may grow also due to the fact that $f_{lab}^{p^+}/f_S^{p^+} = 7.0$. The increased number of incoming protons may accelerate the bubble growth in the lattice places where the non-Aluminum atoms/molecules are present. To check rather the flux is responsible for such effect, it may be worth to irradiate the sample with configuration of $f_{lab}^{p^+}/f_S^{p^+} = 1.0$. If such large bubbles appear, then the reason of their presence are impurities in the metal lattice.

Probe C2 was irradiated at the temperature of 358 K. That irradiation test brought an important result. The formed bubbles grown mainly on micro-scratches present on the foil's surface. Such result has an important implication. During the solar-sail production process the foil is many times folded and rolled. Such foil folds may act as agglomeration zones for the bubbles and therefore increase the erosion rate of that places. Therefore the folds may be the weakest points in the whole sail's membrane structure.

Probe C3 was exposed to proton flux at the highest considered temperature of 383 K. The probe was not populated by the bubbles. That seems to be the critical temperature i.e. above which the recombined Hydrogen atoms simply diffuse from the sample out. Under such conditions bubble formation is impossible. The temperature corresponds to the probe-Sun distance of 1.75 AU.

That experimental setup together with set A clearly shows the role of the temperature in the bubble formation mechanism.

Bubbles populate the foils when the both following conditions are fulfilled:

1. the proton dose is higher than 10^{16} p^+cm^{-2},

2. the specimen temperature is within the range from 300 to 383 K. For the here considered type of foil, such temperatures correspond to probe-Sun distance of 1.75 to 2.85 AU.

5.3.1 Reflectance measurements - preparation of the Bruker 80v spectrometer

The reflectance measurements were made by use of the Vertex Bruker 80v spectrometer. They were preceded by stability analysis of one of the light source being a component of the device. The light source is the Hamamatsu Deuterium lamp. The lamp works in the wavelength range from 200 to 500 nm. The stability measurements were performed as follows. Sixty independent measurements were made in time interval of 5 minutes between each other. A single measurement consists of 256 scans of the wavelength range. The maximum, minimum, and average signal of that sixty measurements is shown in Fig. 5.9.

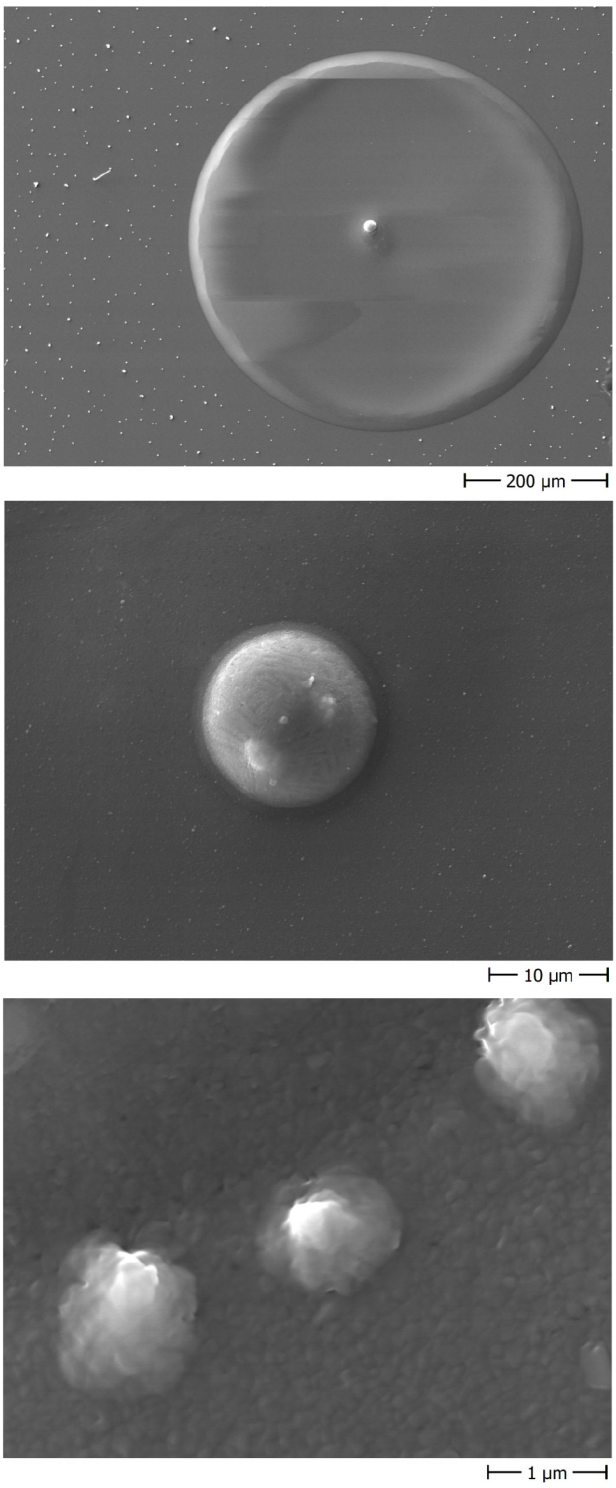

Figure 5.6: Electron microscope pictures of probe C1. The foil was irradiated at the temperature of 338 [K].

The percentage deviation of the signal from the average one is presented in the Fig. 5.10 (top plot). The bottom plot shows the deviation but after excluding first 140 minutes of the measurements. Clearly, the signal deviation from the average one (below 250 nm) is three times larger than above 250 nm. Therefore, future analysis will be taken into account only above that wavelength. Comparing

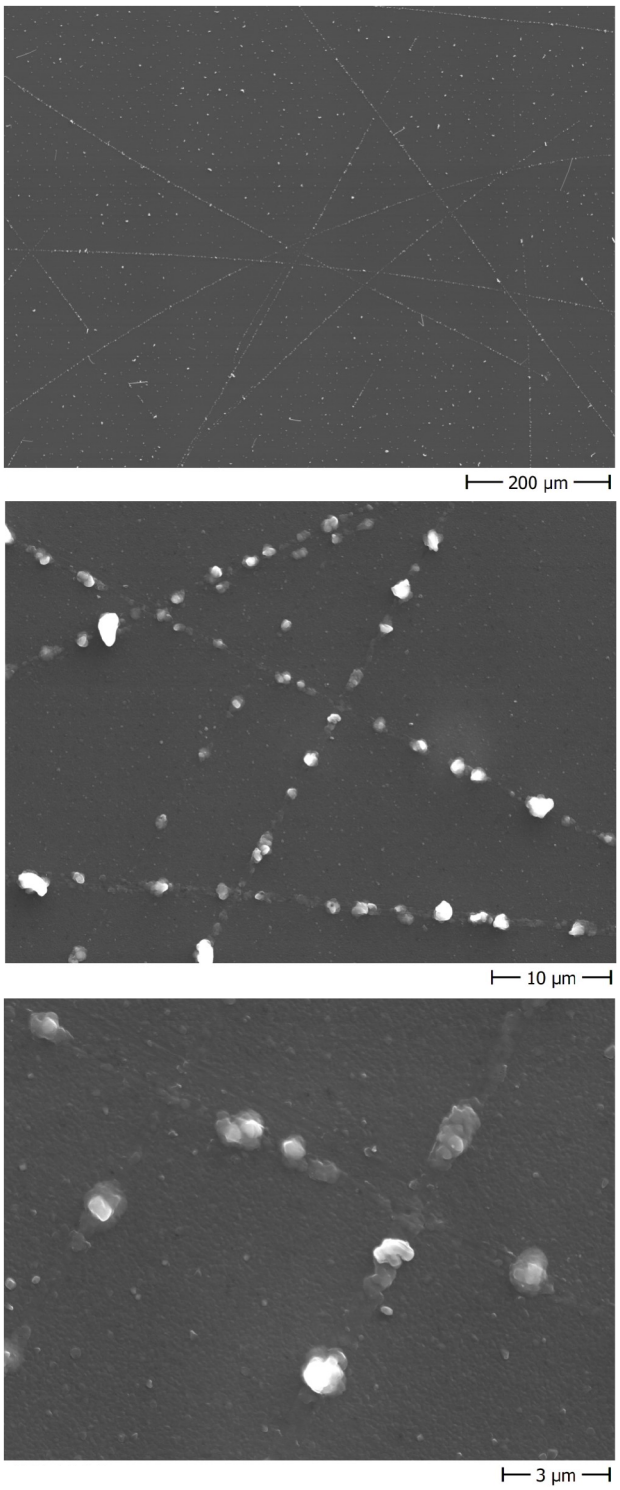

Figure 5.7: Electron microscope pictures of probe C2. The foil was irradiated at the temperature of 358 [K].

both plots one can conclude that the signal stabilize itself after approx. 140 minutes. That can be clearly seen by examining selected wavelength e.g. 350 nm as a function of time, Fig. 5.11. After excluding the data from the first 140 min., the deviation of the signal above 250 nm decreases approx. 2 times, from $\pm 4\%$ to $\pm 2\%$.

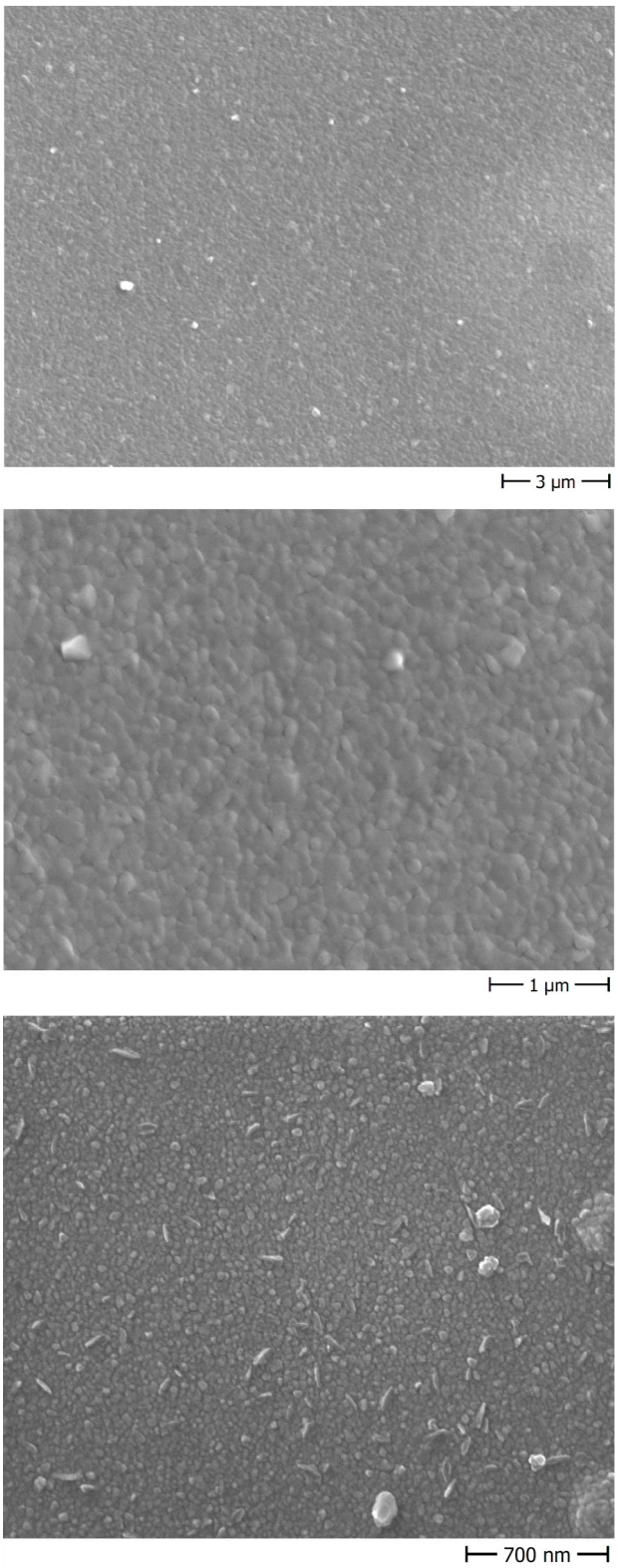

Figure 5.8: Electron microscope pictures of probe C3 (top and middle) and the non-irradiated foil, bottom picture. The test was proceeded at the temperature of 383 [K].

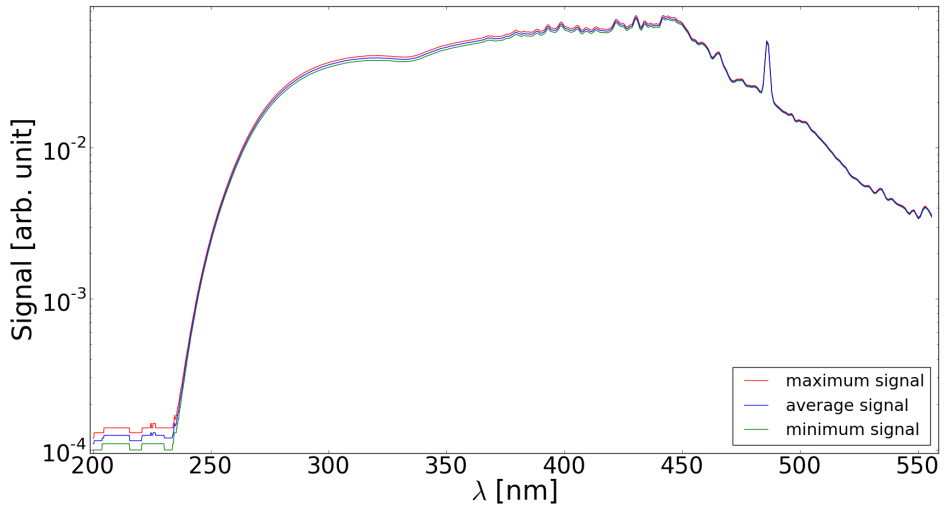

Figure 5.9: The maximum, minimum, and average signal of the Hamamatsu Deuterium lamp mounted in the Bruker 80v spectrometer. The data are averaged over sixty independent measurements taken in time intervals of 5 minutes.

5.3.2 Relative reflectance measurements

The relative reflectance i.e. reflectance of the irradiated foil divided by the reflectance of the reference non-irradiated foil is presented in Fig. 5.12. It should be mentioned that the foil $C2$ is not shown because is was damaged and only part of the foil was suitable for electron microscope measurements. Reflectance of each foil was measured six times and then the average spectrum was calculated.

The Hamamatsu Deuterium lamp was used to estimate the reflectance in the wavelength range from 200 to 500 nm. By reasons explained in the Section 5.3.1 the measurements were performed after 140 minutes of the lamp launch. After that time and above 250 nm the signal deviation from the average one varies $\pm 2\%$, see Fig. 5.10. Therefore, the reflectance is considered above 250 nm. For both considered probes the reflectance starts to decrease above 450 nm, see top plot in the Fig. 5.12. The probe C1, which was irradiated at lower temperature than the probe C3 (see Table 5.4), indicates higher reflectance decrease as the probe C3. Clearly, at lower temperatures the recombined Hydrogen is less mobile in the metal lattice and can more easily agglomerate first into H_2-clusters and finally the bubbles.

The halogen lamp was used to estimate the reflectance above 500 nm. The characteristic increase of the reflectance at the wavelength of ~ 645 nm (the middle plot, Fig. 5.12) is caused by the signal which comes from the laser used in the spectrometer. As expected, the probe C1 indicates largest reflectance decrease as the probe C3. The decrease of the reflectance varies from 4.5% (at 500 nm) to about 3% (at 950 nm).

The last considered wavelength range, from 1000 to 2500 nm, was also examined by use of the halogen lamp. That range brought an unexpected result. The probe C3 indicates larger reflectance decrease than the probe C1. However, the difference between both curves is approx. 1%. Such a small difference may be caused both by the stability of the lamp but also by the sensitivity of the used RT-DLaTGS detector.

The foil C1 which was populated by the bubbles indicates larger relative reflectance decrease as apposed to foil C3. However, difference of the reflectance between both specimens is approx. 2%. The foil C3 was not populated by the bubbles but due to proton irradiation its surface roughness

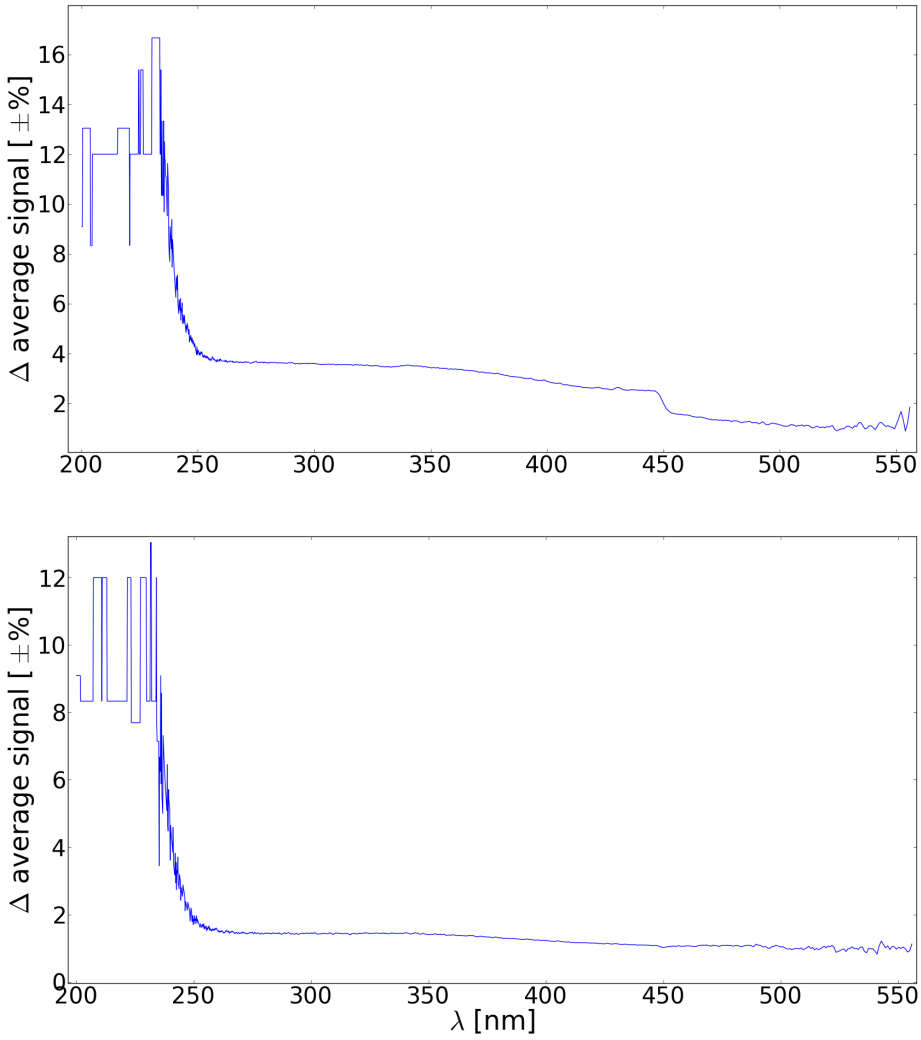

Figure 5.10: Top plot, deviation from the average signal given in % as a function of wavelength. Bottom plot, the average signal deviation but for data taken after 140 minutes of the measurements.

increases what can be clearly seen by comparison the irradiated foil (the top and middle picture in the Fig. 5.8) and the non-irradiated foil (bottom picture).

5.4 Conclusions

It has been proven that thermodynamic model is a flexible tool to simulate and to reproduce the real growth of the molecular Hydrogen bubbles. However, the estimated α and ξ parameters are applicable only for the here presented experimental findings. These parameters depend on type and temperature of the irradiated material. Therefore, change of the material type and the experimental conditions requires a new validation of the model.

The time evolution of decrease of the specular reflectivity ΔR is a model prediction. However, the simulated value of $\Delta R = 4.6\%$ after the 7.9 days of proton irradiation (probes set A, see Section 5.1) seems to coincide well with the measured ΔR (for probe C1), where the specimen was irradiated

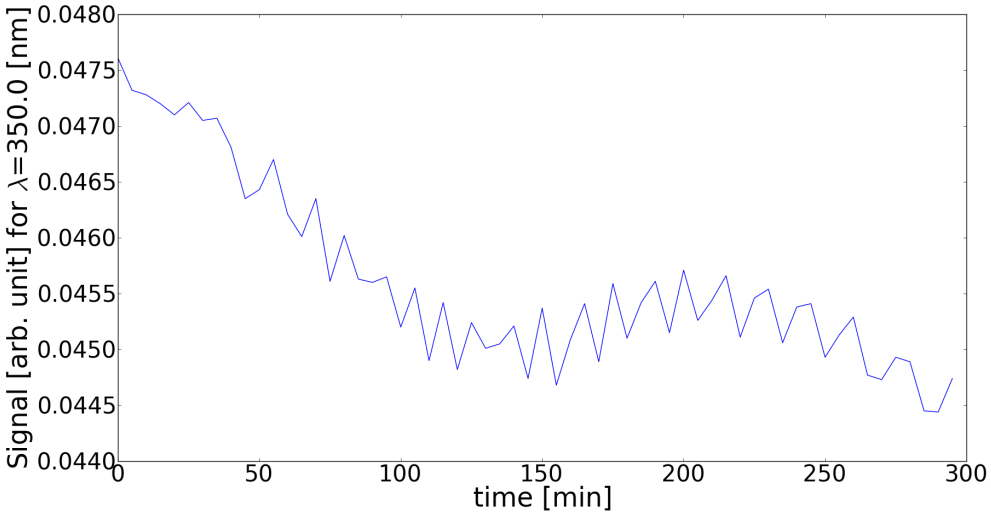

Figure 5.11: Strength of the signal as a function of time for wavelength of 350 nm.

at 338 K. For that sample, and after the test, the $\Delta R = 5\%$ (for $\lambda \cong 500$ nm).

The thermodynamic model requires further improvements. The considered aging factor, the solar protons, are not the only one which can influence the bubble growth process. The solar wind is also essentially made up of electrons and small proportion of heavier ions [121]. Additionally, electromagnetic radiation in the lower wavelength range has also to be taken into consideration. These degradation factors can slow down the bubble growth. The growth deceleration can be explained as follows. Hydrogen molecule dissociate at the energy of 4.5 eV [131]. The dissociation may be caused by the UV-light with the wavelengths ≤ 274 nm. The H_2 gas within the bubbles can then be partially dissociated, and H atoms can diffuse easily through the bubble caps. As a result the bubble growth process may slow down. By these reasons further experimental studies are planned i.e. the influence of the UV-light on the bubble growth dynamics will be studied.

The deceleration can be strengthen by heavier ions generated by the Sun e.g. α-particles. Their diameter is much larger than that of protons or electrons, hence, collisions between the H_2 molecules and the α-particles within the bubbles can additionally increase the dissociation efficiency.

The present condition for the bubble crack mechanism, Eq. 4.18, assumes that the pressure outside the bubbles is negligible small. Under the real space conditions the electromagnetic radiation will exert a pressure on the caps, hence, their sizes may be smaller. On the other hand, bubble caps loose thermal contact with the base material and they become overheated [109]. As a consequence the caps can brake and the H_2 gas can be released. That aspect of the blistering process needs to be examined.

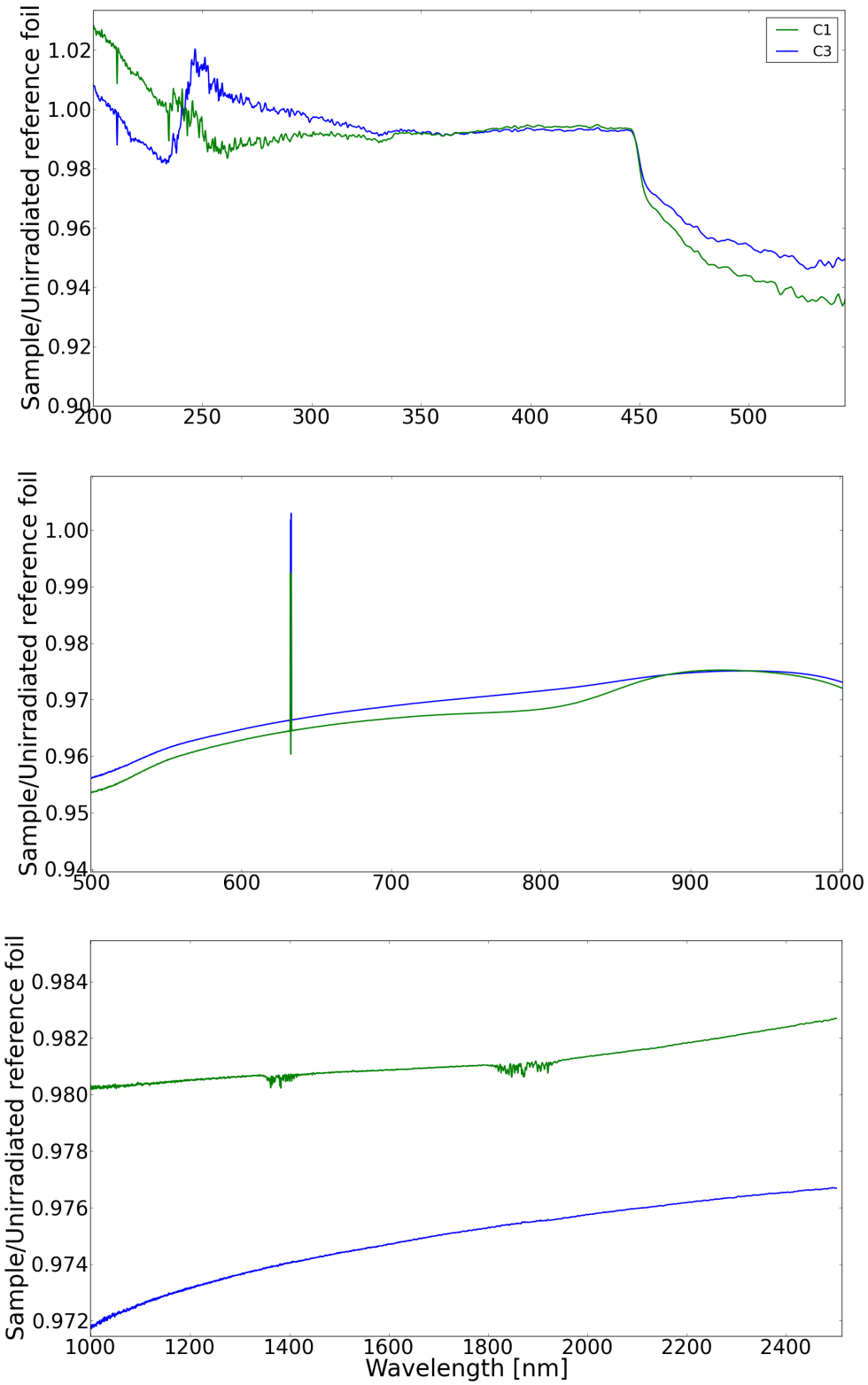

Figure 5.12: Relative reflectance measurements of the probes C1 (green line) and C3 (blue line).

Chapter 6

Conclusions and Outlooks

This thesis demonstrates the importance of degradation processes of materials under space conditions. Since space is filled with high energetic charged particles and electromagnetic radiation, the space environment is highly rough for any technical equipment. In this thesis the thin vacuum deposited Aluminum layers are investigated under the proton flux exposure. Such structures are commonly used in space industry e.g. in the solar sail propulsion technology.

A short review of the most important degradation processes is given. The following degradation processes that may appear in space are discussed: the sputtering process, influence of the Atomic Oxygen, and effects of electromagnetic irradiation. Additionally, I investigated the possibility to charge metallic foils under particle irradiation.

I investigated with special attention recombination processes of incident protons with the free electrons of metals. Recombination is a precondition for the Hydrogen molecular bubble formation. I gave detailed mathematical description of the following three processes: the Auger-, the resonant-, and the Oppenheimer-Brinkman-Kramers (OBK)-process.

The used in the proton irradiation experiments the DLR's Complex Irradiation Facility (CIF) is described in great detail especially its abilities and flexibility to simulate conditions of that present in the interplanetary medium.

The central topic of this thesis is the development and validation of a thermodynamic model of formation of molecular Hydrogen bubbles on metallic surfaces under space conditions. The here presented model allows the description of bubble growth on selected materials and under well defined environmental conditions.

I have validated the model experimentally. Three Upilex $-$ S$^{\textcircled{R}}$ foils covered both sides with 100 nm vacuum deposited Aluminum layers were exposed to the low energetic (2.5 keV) proton flux. All specimens were populated by the bubbles. The proton dose is set to simulate 4.8, 5.0, and 7.9 days in the interplanetary medium at the distance of 2.46 AU from the Sun. The higher the dose, the larger the observed bubbles. Time evolution of an average bubble from the population fits very well of that estimated from the thermodynamic model. Additionally, surface reflectivity decrease as a function of time is evaluated. It coincided well with experimental results.

I have investigated the bubble formation mechanism as a function of proton kinetic energy. I have proven that the flux of 6.0 keV protons does not initiate the bubble growth mechanism (for the dose of 5.9×10^{17} $p^{+}cm^{-2}$ and thickness of the Aluminum layer of > 100 nm) as opposed to lower energy protons. For that energy, 67% of protons stuck in the Aluminum layer at the average depth of 77 nm. Rest of them degrade the Upilex $-$ S$^{\textcircled{R}}$ structure. To produce the bubbles at the surface of the specimen, the larger proton doses are required i.e. to increase the Hydrogen concentration below the Aluminum surface. That experiment implies an important problem. The protons which degrade

the Upilex – S® structure release N, O, and H molecular gas which gather between both layers (Aluminum - Upilex). It is worth to explore how the gas influences the bubble growth mechanism.

I have examined temperature influence on the bubble growth mechanism. I have proven that the bubbles populate the vacuum deposited Aluminum layers when the irradiated specimens' temperature varies from 300 to 383 K. For the here considered foils, that temperature range corresponds to the distance of 1.75 to 2.85 AU from the Sun. For the higher temperatures the Hydrogen atoms diffuse for the sample out and no bubble formation is possible.

The used in the experiments proton fluxes varies from $1.0 f_{\mathrm{S}}^{\mathrm{p}^+}$ to 7.0 $f_{\mathrm{S}}^{\mathrm{p}^+}$. In both cases the results are comparable. However, for the flux of 7.0 $f_{\mathrm{S}}^{\mathrm{p}^+}$, on the irradiated sample (temperature of 338 K) appear few bubbles much larger than for the flux of $f_{\mathrm{S}}^{\mathrm{p}^+}$. Large bubbles may appear in the lattice positions were the non-Aluminum atoms/molecules are present. I have proven that proton flux up to 7.0 $f_{\mathrm{S}}^{\mathrm{p}^+}$ may be used in the terrestrial laboratory experiments to simulate degradation effects caused by proton interactions with Aluminum samples. That is a factor which allows extrapolation of long term degradation effects. I plan to examine higher proton fluxes.

The experiments indicate important behavior of bubble growth. I observed bubbles agglomeration on micro-scratches present on the Aluminum surface. That is important result in context of the solar sail technology. Before the foil's deployment it is many times folded and rolled. Therefore, bubbles may gather in the places where such folds are present.

I plan further theoretical and experimental studies of the bubble growth process. A more sophisticated mechanism of bubble crack process will be implemented. My idea is to take into account the dynamic thickness change of a bubble cap during the growth process.

Since the solar wind is essentially made up of protons, electrons and small proportion of heavier ions, the model should consider collisions e.g. of the α-particles and H_2-molecules within the bubbles. The collisions can dissociate H_2 molecules and decelerate the bubble growth.

I have prepared and took part in the calibration of the Vacuum-UV simulator, which I will use in the second stage of my studies. Electromagnetic radiation in the lower wavelength range can decelerate the bubble growth. The photons with energy higher than 4.5 eV can dissociate the H_2 molecules within the bubbles and therefore H atoms can diffuse easily through the bubble caps.

Since for the foreseeable future no sample returns of materials exposed to the interplanetary space is planned, only both laboratory and theoretical studies of degradation processes that are based on Hydrogen recombination can be carried out. They are nevertheless necessary, since bubble formation can be a serious problem for the success of space missions.

Schlussfolgerunegen und Ausblick

Diese Dissertation demonstriert die Bedeutung von Degradationsprozessen in Materialien unter Weltraumbedingungen. Da der Weltraum mit hochenergetischen Partikeln und elektromagnetischer Strahlung "angefüllt" ist, bildet er eine sehr raue Umgebung für jeden technischen Apparat. In dieser Dissertation werden dünne, mit Aluminium vakuumbeschichtete, Folien untersucht, die einem Protonenfluß ausgesetzt sind. Solche Folien werden häufig in der Weltraumtechnologie verwendet, zum Beispiel bei der Sonnensegeltechnologie.

In der Dissertation gebe ich einen kurzen Überblick über die wichtigsten Degradationsprozesse. Folgende Degradationsprozesse, welche unter Weltraumbedingungen auftreten können, werden diskutiert: Sputtering, der Einfluß von atomaren Sauerstoff und Folgen der Bestrahlung mit elektromagnetischen Wellen. Außerdem untersuche ich die Möglichkeit, metallische Folien durch Bestrahlung mit geladenen Teilchen aufzuladen.

Insbesondere studierte ich den Prozeß der Rekombination von in das Metall eindringenden Protonen mit seinen freien Elektronen. Diese Rekombination ist eine Voraussetzung für die Bildung von Blasen molekularen Wasserstoffs. Ich liefere eine ausführliche mathematische Beschreibung folgender drei Prozesse: Auger-, resonanter - und Oppenheimer-Brinkmann-Kramers (OBK)- Prozeß.

Die mit der Komplexen Bestrahlungseinrichting (KOBE) des DLR durchgeführten Bestrahlungsexperimente beschreibe ich in aller Ausführlichkeit, insbesondere ihre Fähigkeit und die Flexibilität von KOBE die Bedingungen zu simulieren, welche im interplanetaren Raum vorherrschen.

Der zentrale Gegenstand diese Dissertation ist die Entwicklung und Validierung eines thermodynamischen Modells der Bildung von Blasen aus molekularen Wasserstoff auf metallischen Oberflächen unter Weltraumbedingungen. Das hier vorgestellte Modell gestattet die Beschreibung des Blasenwachstums auf ausgewählten Materialien und unter wohldefinierten Umgebungsbedingungen.

Die Ergebnisse der Modellrechnungen habe ich experimentell überprüft. Drei Upilex – S® - Folien, auf beiden Seiten mit 100 nm dicken Aluminium beschichtet, wurden mit niederenergetischen (2.5 keV) Protonen bestrahlt. Auf allen Proben bildeten sich Blasen. Die Protonendosis war so gewählt, daß ein Aufenthalt der Proben von 4.8, 5.0 und 7.9 Tagen im interplanetaren Raum bei einer Entfernung zur Sonne von 2.46 AU simuliert wurde. Erwartungsgemäß ist der Blasendurchmesser der Protonendosis proportional. Die zeitliche Entwicklung einer mittleren Blase läßt sich sehr gut mit dem in der Dissertation vorgestellten thermodynamischen Model des Blasenwachstums beschreiben. Dieses Model macht auch Aussagen über die Entwicklung der Reflektivität als Funktion der Protonendosis. Hier ergab sich ebenfalls eine gute Übereinstimmung der gemessenen mit der vorhergesagten Reflektivität.

Ich habe den Mechanismus der Blasenbildung in Abhängigkeit von der kinetischen Energie der Protonen untersucht. Dabei habe ich gezeigt, daß, im Gegensatz zu Protonen mit kleinerer Kinetischer Energie, Flüsse von Protonen mit kinetischen Energien > 6.0 keV nicht zur Bildung von Blasen führen (für Dosen von 5.9×10^{17} p^+cm^{-2} und einer Dicke der Aluminiumschicht > 100 nm). Protonen kleinerer Energie bleiben zu 67% in einer mittleren Tiefe von 77 nm im Aluminium stecken. Die

übrigen degradieren die Upilex – S®- Struktur. Um Blasen auf der Probenoberfläche zu bilden sind größere Protonendosen erforderlich um die Konzentration von Wasserstoffionen unter der Aluminiumoberfläche zu erhöhen. Das Experiment impliziert ein wichtiges Problem: die Protonen, welche die Upilex – S® - Struktur degradieren, verursachen die Freisetzung von molekularen Stickstoff -, Sauerstoff - und Wasserstoffgas, welches sich zwischen beiden Schichten (Aluminium - Upilex) ansammelt. Es wäre wichtig zu untersuchen, wie diese Gase das Blasenwachstum beeinflussen.

Ich habe den Einfluß der Temperatur auf den Prozeß des Blasenwachstums untersucht und gezeigt, daß die Blasen vakuumbeschichtete Aluminiumfolien besiedeln, wenn die Temperatur der bestrahlten Folie im Bereich von 300 bis 383 K liegt. Für die in der Dissertation untersuchten Folien entspricht dieser Temperaturbereich einen Abstand von 1.75 to 2.85 AU von der Sonne. Bei noch höheren Probentemperaturen diffundieren die Wasserstoffmoleküle zu schnell aus dem Metall hinaus.

Die in den Experimenten verwendeten Protonenflüsse variieren zwischen $1.0 f_S^{p^+}$ und $7.0\ f_S^{p^+}$. In beiden Fällen sind die Ergebnisse vergleichbar. Jedoch, bei einem Fluß von $7.0\ f_S^{p^+}$, erscheinen auf der bestrahlten Probe (Temperatur 338 K) einige Blasen signifikant größer als für einen Fluß von $1.0 f_S^{p^+}$. Große Blasen werden sichtbar an Gitterplätzen, wo sich Nicht-Aluminiumatome/Moleküle befinden. Ich konnte zeigen, daß ein Protonenfluß bis zu $7.0\ f_S^{p^+}$ in terrestrischen Experimenten verwendet werden kann, um Degradationseffekte verursacht durch die Wechselwirkungen von Protonen in Aluminium zu simulieren. Das ist ein großer Beschleunigungsfaktor, welcher die Extrapolation auf Langzeitdegradationseffekte ermöglicht. Ich habe Experimente mit noch größeren Protonenflüssen geplant.

Die Experimente bestätigten im wesentlichen die Voraussagen des Modells des Blasenwachstums. Ich beobachtete Blasenansammlungen an Mikrokratzern auf der Aluminiumoberfläche. Das ist ein wichtiges Ergebnis für die Solarsegeltechnologie. Bevor das Segel entfaltet wird, wurde es viele Male gefaltet und zusammengerollt, wobei Mikrokrazer entstehen können. Infolgedessen können sich Blasen besonders an solchen Falten ansammeln.

Ich plane weitere theoretische und experimentelle Untersuchungen des Blasenwachstumprozesses. Ein besser wissenschaftlich begründeter Mechanismus des Bersten der Blasen wird implementiert werden. Meine Idee ist es, die dynamische Änderung der Dicke des Blasenkappe während des Wachstums zu berücksichtigen.

Da der Sonnenwind hauptsächlich aus Protonen, Elektronen und einem kleinen Anteil schwererer Ionen besteht, sollte das Modell auch Stöße berücksichtigen, z.B. von α - Teilchen und H_2 - Molekülen im Inneren der Blase. Solche Stöße können die H_2 - Moleküle dissoziieren und dadurch das Blasenwachstum verlangsamen.

In der Dissertation ist die Calibration des Vacuum - UV - Simulators beschrieben, die ich vorbereitet und mit durchgeführt habe. Diese Quelle kurzwelliger elektromagnetischer Strahlung werde ich in der nächsten Phase meiner Untersuchungen verwenden. Kurzwellige elektromagnetische Strahlung kann ebenfalls das Blasenwachstum verzögern. Photonen mit einer Energie größer als 4.5 eV können die H_2 - Moleküle in den Blasen dissoziieren, und die dabei entstehenden Wasserstoffatome können leicht durch die Blasenkappen diffundieren.

Da in der vorhersehbaren Zukunft keine Materialproben zur Erde zurückgebracht werden sollen, welche den Bedingungen des interplanetaren Weltraumes ausgesetzt waren, bleiben nur experimentelle und theoretische Untersuchungen der Degradationsprozesse welche auf Wasserstoffrekombination beruhen. Solche Untersuchungen sind jedoch unerläßlich, weil die Blasenbildung ein ernsthaftes Problem für die erfolgreiche Durchführung von Weltraummissionen darstellen kann.

Appendix A

The Hartree approximation

One can consider a multi-particle system described by a Hamiltonian (all particles are distinguishable) in the form:

$$H = \sum_{\mathrm{i}} H_{\mathrm{i}} + \frac{1}{2} \sum_{\mathrm{i} \neq \mathrm{j}} V_{\mathrm{i,j}}, \tag{A.1}$$

where $H_{\mathrm{i}} = \frac{q_{\mathrm{i}}^2}{2m} + V_{\mathrm{s}}(\mathbf{r}_{\mathrm{i}})$ and $V_{\mathrm{i,j}} = V_{\mathrm{int}}(\mid \mathbf{r}_{\mathrm{i}} - \mathbf{r}_{\mathrm{j}} \mid)$, here V_{s} is the single-particle potential and V_{int} is the interaction potential [132].

In the Hartree approximation, it is assumed that the wavefunction of eigenstates of the Hamiltonian can be written as a product of wavefunctions of single particle states, thus [132]:

$$\Phi = \phi_1(\mathbf{r}_1)\ \phi_2(\mathbf{r}_2)\ \phi_3(\mathbf{r}_3)\ ... \tag{A.2}$$

The expectation value of the Hamiltonian will have the form:

$$\int d^3r_1 d^3r_2\ ...\ \phi_1^*(\mathbf{r}_1)\phi_2^*(\mathbf{r}_2)\ ...\ \left(\sum_{\mathrm{i}} H_{\mathrm{i}} + \frac{1}{2} \sum_{\mathrm{i} \neq \mathrm{j}} V_{\mathrm{i,j}} \right) \phi_1(\mathbf{r}_1)\phi_2(\mathbf{r}_2)\ ... \tag{A.3}$$

Thus, the sum over H_{i} and $V_{\mathrm{i,j}}$ reduces to one and two particle expectation values [132]. Taking the functional derivative of the above equation with respect to $\phi_{\mathrm{m}}^*(\mathbf{r}_{\mathrm{m}})$ for the m^{th} particle, it is:

$$\int d^3r_{\mathrm{m}} \left(H_{\mathrm{m}}\phi_{\mathrm{m}}(\mathbf{r}_{\mathrm{m}}) + \sum_{\mathrm{i} \neq \mathrm{m}} \int d^3r_{\mathrm{i}} \phi_i^*(\mathbf{r}_{\mathrm{i}}) V_{\mathrm{i,m}} \phi_i(\mathbf{r}_{\mathrm{i}}) \phi_m(\mathbf{r}_{\mathrm{m}}) - E\phi_m^*(\mathbf{r}_{\mathrm{m}}) \right) \delta\phi_m^*(\mathbf{r}_{\mathrm{m}}) = 0. \tag{A.4}$$

Thus Eq. A.4 is then:

$$H_{\mathrm{m}}\phi_{\mathrm{m}}(\mathbf{r}_{\mathrm{m}}) + \left(\sum_{\mathrm{i} \neq \mathrm{m}} \int d^3r_{\mathrm{i}} \phi_i^*(\mathbf{r}_{\mathrm{i}})\ V_{\mathrm{i,m}}\ \phi_i(\mathbf{r}_{\mathrm{i}}) \right) \phi_m(\mathbf{r}_{\mathrm{m}}) = E\phi_m(\mathbf{r}_{\mathrm{m}}). \tag{A.5}$$

The stationary Schrödinger equation A.5 is called the Hartree equation [132]. Hartree approximation reduces a N-particle problem to a set of single equations that one can solve. The interaction between the particles is reduced to a single potential [132]:

$$V_{\mathrm{H}}(\mathbf{r}_{\mathrm{m}}) = \int d^3r_{\mathrm{i}} \sum_{\mathrm{i} \neq \mathrm{m}} \mid \phi_{\mathrm{i}}(\mathbf{r}_{\mathrm{i}}) \mid^2 V_{\mathrm{int}}(\mathbf{r}_{\mathrm{i}} - \mathbf{r}_{\mathrm{m}}). \tag{A.6}$$

Equation A.6 describes the interaction of the m$^{\text{th}}$ particle with all other particles. If one consider a Coulomb interaction between the particles, the Hartree potential looks like the interaction of one particle with the charge density of all other particles [132]:

$$V_{\text{H}}(\mathbf{r}_{\text{m}}) = \int d^3r \; \frac{Z_{\text{t}} Z_{\text{p}} \rho_{\text{m}}(\mathbf{r})}{\mid \mathbf{r}_{\text{m}} - \mathbf{r} \mid}. \tag{A.7}$$

Here $\rho_{\text{m}}(\mathbf{r})$ is the probability density that the m$^{\text{th}}$ particle is located at position $\mathbf{r}$. Z_{t} and Z_{p} are a charge numbers of target ions and incident ions, respectively. The m$^{\text{th}}$ particle depends on the states of all the other $N-1$ particles.

Appendix B

The ionization energy of an ion having active electron in the 1s state - the OBK process

The ionization energy of an electron in the $1s$ state is:

$$-I_{\mathrm{K}} = E(\alpha, C) = \langle \phi_{\mathrm{i}}(\mathbf{r}_1) \mid H \mid \phi_{\mathrm{i}}(\mathbf{r}_1) \rangle, \tag{B.1}$$

where the Hamiltonian and the wave function are:

$$H = -\frac{1}{2}\boldsymbol{\nabla}^2 - \frac{1}{r_1} - \frac{(Z_{\mathrm{t}} - 1)}{r_1}\exp(-Cr_1), \tag{B.2}$$

$$\phi_{\mathrm{i}}(\mathbf{r}_1) = \pi^{-\frac{1}{2}}\alpha^{\frac{3}{2}}\exp(-\alpha\mathbf{r}_1). \tag{B.3}$$

To calculate the ionization energy one can use the spherical coordinate system. For simplicity each term of Eq. B.2 is considered separately:

1. $\langle \phi_{\mathrm{i}}(\mathbf{r}_1) \mid -\frac{1}{2}\boldsymbol{\nabla}^2 \mid \phi_{\mathrm{i}}(\mathbf{r}_1) \rangle$:

$$\langle \phi_{\mathrm{i}}(\mathbf{r}_1) \mid -\frac{1}{2}\boldsymbol{\nabla}^2 \mid \phi_{\mathrm{i}}(\mathbf{r}_1) \rangle = -\frac{1}{2}\langle \phi_{\mathrm{i}}(\mathbf{r}_1) \mid \left[-\pi^{-\frac{1}{2}}\alpha^{\frac{5}{2}}\frac{2}{r_1}\exp(-\alpha r_1) + \pi^{-\frac{1}{2}}\alpha^{\frac{7}{2}}\exp(-\alpha r_1) \right]. \tag{B.4}$$

The first term in the Eq. B.4 is:

$$\begin{aligned} -\tfrac{1}{2} \quad & \int_V \pi^{-\frac{1}{2}}\alpha^{\frac{3}{2}}\exp(-\alpha\mathbf{r}_1)\left[-\pi^{-\frac{1}{2}}\alpha^{\frac{5}{2}}\frac{2}{r_1}\exp(-\alpha r_1) \right] dV = \\ & 4\alpha^4 \int_0^\infty r_1 \exp(-2\alpha r_1)\, dr_1 = -\alpha^2 \frac{2\alpha r_1 + 1}{\exp(2\alpha r_1)} \mid_0^\infty = \\ & -\alpha^2 \frac{1}{1 + \frac{(2\alpha r_1)^2}{2(1+2\alpha r_1)} + \frac{(2\alpha r_1)^3}{6(1+2\alpha r_1)} + \ldots} \mid_0^\infty = \alpha^2, \end{aligned} \tag{B.5}$$

and the second one is:

$$-\tfrac{1}{2}\int_V \pi^{-\frac{1}{2}}\alpha^{\frac{3}{2}}\exp(-\alpha\mathbf{r}_1)\left[\pi^{-\frac{1}{2}}\alpha^{\frac{7}{2}}\exp(-\alpha\mathbf{r}_1)\right]dV = \tag{B.6}$$
$$-2\alpha^5\left[\exp(-2\alpha\mathbf{r}_1)\left(\frac{r_1^2}{-2\alpha}-\frac{2r_1}{4\alpha^2}-\frac{1}{4\alpha^3}\right)\right]|_0^\infty = -\frac{1}{2}\alpha^2.$$

So the term $\langle\phi_{\rm i}(\mathbf{r}_1)\mid -\frac{1}{2}\boldsymbol{\nabla}^2\mid\phi_{\rm i}(\mathbf{r}_1)\rangle = \frac{1}{2}\alpha^2$.

2. $\langle\phi_{\rm i}(\mathbf{r}_1)\mid -\frac{1}{r_1}\mid\phi_{\rm i}(\mathbf{r}_1)\rangle$:

$$\langle\phi_{\rm i}(\mathbf{r}_1)\mid -\frac{1}{r_1}\mid\phi_{\rm i}(\mathbf{r}_1)\rangle = -4\alpha^3\int_0^\infty r_1\exp(-2\alpha r_1)\,dr_1 = \tag{B.7}$$
$$\alpha\frac{2\alpha r_1+1}{\exp(2\alpha r_1)}|_0^\infty = \alpha\frac{1}{1+\frac{(2\alpha r_1)^2}{2(2\alpha r_1+1)}+\frac{(2\alpha r_1)^3}{6(2\alpha r_1+1)}+\ldots}|_0^\infty = -\alpha.$$

3. $\langle\phi_{\rm i}(\mathbf{r}_1)\mid -\frac{(Z_{\rm t}-1)}{r_1}\exp(-Cr_1)\mid\phi_{\rm i}(\mathbf{r}_1)\rangle$:

$$\begin{aligned}\langle\phi_{\rm i}(\mathbf{r}_1)\mid -\frac{(Z_{\rm t}-1)}{r_1}\exp(-Cr_1)\mid\phi_{\rm i}(\mathbf{r}_1)\rangle &= \\ -4(Z_{\rm t}-1)\alpha^3\int_0^\infty r_1\exp[-(C+2\alpha)r_1]\,dr_1 &= \\ 4(Z_{\rm t}-1)\alpha^3\frac{\exp[-(C+2\alpha)r_1]}{(C+2\alpha)^2}[(C+2\alpha)r_1+1]\,|_0^\infty &= \\ 4(Z_{\rm t}-1)\frac{\alpha^3}{(C+2\alpha^2)^2}\frac{1}{1+\frac{[(C+2\alpha)r_1]^2}{2[1+(C+2\alpha)r_1]}+\ldots} &= \\ -4(Z_{\rm t}-1)\frac{\alpha^3}{(C+2\alpha)^2}.\end{aligned} \tag{B.8}$$

Thus, ionization energy of the electron in the $1s$ state is the sum of three terms calculated above:

$$-I_{\rm K} = \frac{1}{2}\alpha^2-\alpha-4(Z_{\rm t}-1)\frac{\alpha^3}{(C+2\alpha)^2}. \tag{B.9}$$

Appendix C

VUV-Source, tabulated spectra lines

Table C.1 contains validated spectra lines and their elements in the wavelength range from 40 to 410 nm. The continuous spectrum in the wavelength range from 138 to 160 nm is presented in the Table C.2. All of the spectra lines and their elements are taken from the NIST database [14].

Table C.1: Validated spectra lines in the wavelength range from 40 to 410 nm. The lines are depicted in Figs. 3.11, 3.12, 3.13 and 3.14. Data are taken from the NIST database [14].

Wavelength [nm]	Element	Wavelength [nm]	Element	Wavelength [nm]	Element
46.201	Ar VI	104.822	Ar I	248.00368	W II
47.575	Kr V	106.6134	Cu II	252.00734	W II
48.799	Ar IV	108.592	Al V	253.99098	W II
50.109	Ar VII	109.4264	W IV	257.98438	Fe I
50.782	Kr VI	111.322	Cu V	261.9954	W I
52.2186	He I	111.9947	Cu II	264.998	W I
54.383	Ar VI	114.6102	W III	268.0046	W I
55.775	Kr IV	116.4867	Kr I	271.0004	W I
57.8212	Kr III	119.4528	Ar V	276.0036	W I
59.7701	Ar II	121.56699	HI	283.0054	Fe I
60.183	Kr IV	123.62	Cr III	288.99877	Fe I
61.1831	Kr IV	128.395	Ar VI	294.5106	He I
62.165	Ar VII	130.387	Ar VI	297.9860	W I
63.72881	Ar III	132.3847	W IV	300.0	Fe I
66.200	Ar IX	134.3710	Ar III	303.01481	Fe I
67.0948	Ar II	135.6086	W III	309.0088	W I
67.897	Kr IV	137.9670	Al III	314.0146	W I
68.8915	Kr VII	139.3886	W III	321.01863	Fe I
69.9812	Kr IV	142.3889	W V	324.993	Mo I
72.394	Ar VII	145.8088	W IV	334.97241	Fe I
73.0	Fe III	149.1151	W III	337.997	Mo I
74.011	Ar VIII	154.3841	W IV	343.003	Ar III
76.8132	Kr III	155.982	Ar IV	348.983	O IV
78.216	Kr IV	157.592	La IV	350.98614	Fe I
80.109	Ar IV	158.8466	W III	356.006	W I
82.598	Kr VI	160.3074	Ar II	357.995	Kr III
83.417	Kr VI	162.790	Kr IV	364.0134	W I
84.2805	Ar I	165.5639	Cr V	365.97333	Fe I
85.0154	Kr I	167.211	Kr IV	367.99131	Fe I
86.832	Ar IV	169.028	Cr III	372.999	W I
87.792	Ar VII	178.5729	W III	377.03012	Fe I
89.394	Kr IV	183.001	Ni III	380.9848	W I
90.0313	Kr I	188.77646	Fe I	384.99664	Fe I
91.9342	H I	192.0378	W III	386.9928	W I
93.0749	H I	197.39162	Fe I	393.0231	W I
94.9742	H I	206.3848	W IV	397.98498	W II
96.4075	Kr IV	213.20171	Fe I	403.9938	Fe I
97.2541	H I	217.80806	Fe I	407.98377	Fe I
98.03	Ar IV	223.008	Cu I		
99.004	Ar IV	228.998	Ni I		
100.1883	W IV	232.003	Ni I		
102.5948	W IV	241.9985	W II		

Table C.2: Validated spectra lines in the wavelength range from 138 to 160 nm. The lines are depicted in Fig. 3.12 for a gas flow of 1200 and 2000 sccm. Data are taken from the NIST database [14].

Wavelength [nm]	Element	Wavelength [nm]	Element	Wavelength [nm]	Element	Wavelength [nm]	Element
138.0723	Ar II	144.766	Ar V	152.411	Kr IV	157.5375	Kr II
138.2228	Ar II	144.835	Ar IV	152.515	Kr IV	157.566	Kr IV
138.235	Kr V	145.1879	Ar II	152.5486	Kr II	157.5815	Ar II
138.2765	Ar II	145.226	Kr V	152.566	Kr IV	157.594	Kr IV
138.386	Kr V	145.348	Kr III	152.626	Ar IV	157.6155	Kr II
138.459	Kr V	145.544	Ar IV	152.795	Ar IV	157.65915	Ar III
138.511	Kr IV	145.5484	Ar II	152.818	Ar IV	157.6897	Ar II
138.681	Kr IV	145.630	Kr IV	153.250	Kr III	157.8812	Ar II
138.900	Kr IV	145.730	Kr IV	153.286	Kr IV	157.9513	Kr II
138.996	Kr IV	145.923	Ar IV	153.341	Kr IV	157.9731	Kr II
139.212	Ar XI	145.948	Kr IV	153.553	Kr IV	157.974	Kr IV
139.263	Kr V	145.9875	Ar II	153.600	Ar IV	158.0260	Ar III
139.361	Kr V	146.00973	Ar III	153.668	Ar IV	158.0768	Ar II
139.564	Ar IV	146.02487	Ar II	153.855	Kr V	158.0960	Ar II
139.6231	Ar II	146.099	Ar IV	153.9075	Kr II	158.198	Kr IV
140.089	Kr IV	146.109	Kr IV	154.007	Kr V	158.248	Kr III
140.168	Kr III	146.265	Kr XXIII	154.026	Ar IV	158.30377	Ar III
140.181	Kr IV	146.3	Ar VIII	154.2540	Ar III	158.383	Ar II
140.220	Kr V	146.3155	Ar II	154.291	Kr V	158.4563	Kr II
140.288	Kr III	146.4072	Kr II	154.4177	Ar II	158.601	Kr III
140.750	Ar IV	146.4176	Ar II	154.4711	Ar II	158.6093	Kr II
140.930	Ar IV	146.5153	Ar II	154.508	Kr IV	158.6170	Kr II
141.013	Ar IV	146.553	Kr IV	154.630	Kr IV	158.6256	Ar II
141.157	Kr IV	146.55506	Ar III	164.666	Ar IV	158.6330	Ar III
141.235	Kr III	146.57036	Ar III	154.7354	Ar II	158.66206	Ar III
141.3894	Kr II	146.600	Kr IV	155.452	Ar IV	158.6621	Kr II
141.397	Ar V	146.614	Kr IV	155.539	Kr V	158.8740	Ar III
141.614	Kr V	146.6460	Kr II	155.6220	Ar III	158.9384	Kr II
141.689	Kr IV	146.6524	Ar II	155.6630	Ar III	158.9463	Ar II
141.959	Ar IV	146.78533	Ar III	155.7302	Ar II	158.987	Kr IV
142.060	Ar VI	146.8006	Ar III	155.851	Kr IV	159.0229	Ar II
142.070	Kr III	146.8021	Kr II	155.8802	Kr III	159.032	Kr IV
142.171	Kr IV	147.204	Ar IV	155.9072	Ar II	159.160	Kr III
142.2000	Ar III	147.2594	Ar II	155.982	Ar IV	159.1933	Ar II
142.251	Ar VI	147.448	Ar IV	156.0184	Ar II	159.2565	Kr II
142.2512	Kr II	147.4537	Ar II	156.193	Kr IV	159.3581	Ar II
142.3553	Kr III	147.717	Kr IV	156.2441	Ar II	159.386	Kr IV
142.429	Kr IV	147.915	Ar IV	156.285	Kr III	159.3946	Kr II
142.497	Kr V	148.136	Kr IV	156.3036	Ar II	159.4787	Ar II
142.575	Kr III	148.160	Ar IV	156.5377	Ar II	159.4895	Kr II
142.619	Ar IV	148.3429	Kr III	156.603	Kr V	159.5734	Ar II
142.777	Kr III	148.601	Ar IV	156.6812	Ar II	159.6141	Ar II
142.965	Kr IV	148.628	Kr IV	156.7987	Ar II	159.6210	Ar III
142.984	Kr V	148.952	Kr IV	156.8050	Kr II	159.641	Kr IV
143.068	Kr IV	149.018	Kr IV	156.8690	Ar III	159.667	Kr IV
143.378	Kr V	149.0928	Kr II	156.891	Kr V	159.8082	Kr II
143.4070	Ar III	149.1104	Kr II	156.9135	Kr II	159.8561	Ar II
143.5085	Kr II	149.532	Ar IV	156.982	Kr IV	159.8724	Ar II
143.557	Ar IV	149.5769	Kr II	156.9886	Kr III	159.8872	Ar II
143.5676	Kr II	149.781	Ar IV	157.017	Ar IV	159.9125	Ar II
143.620	Kr V	149.828	Kr V	157.038	Kr IV	159.9492	Kr II
143.648	Kr IV	149.850	Kr III	157.1390	Ar II	159.9597	Ar II
143.7020	Ar III	149.964	Kr V	157.1876	Kr II	159.98	Kr V
143.7170	Ar III	150.0740	Ar III	157.1920	Ar III	159.982	Kr IV
143.912	Kr IV	150.158	Kr IV	157.23340	Ar III		
144.007	Ar III	150.290	Kr IV	157.2340	Kr II		
144.0210	Ar III	150.591	Kr III	157.3050	Ar III		
144.2440	Ar III	150.880	Ar IV	157.318	Kr III		
144.343	Kr IV	150.984	Ar IV	157.3404	Kr II		
144.4	Ar VIII	151.351	Kr IV	157.4103	Kr II		
144.4343	Kr II	151.4585	Kr II	157.4340	Kr II		
144.528	Kr IV	151.605	Ar IV	157.4402	Ar II		
144.563	Kr IV	151.685	Kr IV	157.4733	Kr II		
144.750	Kr III	152.162	Kr IV	157.498	Kr IV		
144.762	Kr IV	152.371	Kr IV	157.4992	Ar II		

Appendix D

Formation of Hydrogen molecular bubbles on metallic surfaces

D.1 Helmholtz free energy of H_2 molecules placed in certain positions in the metal lattice

To get the relation of the Helmholtz free energy of the H_2 molecules located at certain positions in the sample but outside the bubbles, the definition of the free energy is used:

$$F = E_{\rm int} - TS, \qquad S = k_{\rm B} \ln \Omega, \tag{D.1}$$

here $E_{\rm int}$ is the internal energy of the H_2 molecules located at certain positions in the metal lattice, S denotes the entropy, while Ω represents the number of ways in which the H_2 molecules can be arranged on the N_0 lattice sites (see Eq. 4.22).

The number of H_2 molecules located outside the bubbles at certain positions in the metal lattice is $N^{\rm T}_{\rm H_2} - \sum_{\rm i}^{N^{\rm T}_{\rm B}} \sum_{\rm j}^{N} N_{\rm H_2,i,j}$. Where $N^{\rm T}_{\rm H_2}$ is the total number of H_2 molecules in the sample, while $\sum_{\rm i}^{N^{\rm T}_{\rm B}} \sum_{\rm j}^{N} N_{\rm H_2,i,j}$ is the total number of H_2 molecules within all bubbles. The summation over the number of time steps j count the number of H_2 molecules in the $i^{\rm th}$ bubble. The second summation over the number of bubble $i^{\rm th}$ counts the number of H_2 molecules within all bubbles. Therefore, performing the subtraction one gets the total number of H_2 molecules outside all bubbles, located at certain positions in the metal lattice. The entropy $k_{\rm B} \ln \Omega$ of the collection of the H_2 molecules placed on a lattice sites is [51]:

$$\begin{aligned} S &= k_{\rm B} \ln \frac{N_0!}{\left(N^{\rm T}_{\rm H_2} - \sum_{\rm i}^{N^{\rm T}_{\rm B}} \sum_{\rm j}^{N} N_{\rm H_2,i,j}\right)! \left[N_0 - \left(N^{\rm T}_{\rm H_2} - \sum_{\rm i}^{N^{\rm T}_{\rm B}} \sum_{\rm j}^{N} N_{\rm H_2,i,j}\right)\right]!}, \\ &\cong -k_{\rm B} \left(N^{\rm T}_{\rm H_2} - \sum_{\rm i}^{N^{\rm T}_{\rm B}} \sum_{\rm j}^{N} N_{\rm H_2,i,j}\right) \ln \left[\frac{N^{\rm T}_{\rm H_2} - \sum_{\rm i}^{N^{\rm T}_{\rm B}} \sum_{\rm j}^{N} N_{\rm H_2,i,j}}{N_0}\right]. \end{aligned} \tag{D.2}$$

The internal energy $E_{\rm int}$ is given by the following relation:

$$E_{\rm int} = \epsilon_{\rm H_2} \left(N^{\rm T}_{\rm H_2} - \sum_{\rm i}^{N^{\rm T}_{\rm B}} \sum_{\rm j}^{N} N_{\rm H_2,i,j}\right), \tag{D.3}$$

where ϵ_{H_2} is the binding energy of the H_2 molecule to a vacancy [110]. The internal energy of H_2 molecules located in the metal lattice sites is a product of the binding energy of a single H_2 molecule and the number of molecules.

The Helmholtz free energy of the H_2 molecules located outside the bubbles at certain positions in the metal lattice is then:

$$F_{H_2} = \left(N_{H_2}^{T} - \sum_{i}^{N_B^T} \sum_{j}^{N} N_{H_2,i,j} \right) \left[\epsilon_{H_2} + k_B T \ln \left(\frac{N_{H_2}^{T} - \sum_{i}^{N_B^T} \sum_{j}^{N} N_{H_2,i,j}}{N_0} \right) \right]. \tag{D.4}$$

D.2 Helmholtz free energy of H atoms in the sample

The number of H atoms in the sample and outside the bubbles is:

$$N_H = N_H^T - 2 \left(\sum_{i}^{N_B} \sum_{j}^{N} N_{H_2,i,j} + N_{H_2}^{\text{out. bubbles}} \right), \tag{D.5}$$

where N_H^T is the total number of H atoms in the sample, so the number counts all of the incident Hydrogen ions which have recombined into Hydrogen atoms. Some of the Hydrogen atoms have recombined to H_2 molecules and some of the molecules are forming the bubbles. Hence to get the number of H atoms located on the lattice sites one has to subtract the total number of Hydrogen atoms N_H^T and those Hydrogen atoms which build H_2 clusters and H_2 bubbles. The reason of the factor 2 is that a single H_2 molecule consists of two H atoms.

The procedure to estimate the Helmholtz free energy of H atoms in the sample is the same as in Eq. D.4. Hence the term is:

$$F_H = N_H \left(\epsilon_H + k_B T \ln \frac{N_H}{N_0} \right), \tag{D.6}$$

where ϵ_H is the migration energy of the H atom in the metal lattice. The migration energy is defined as the minimum energy which has to be added to the H atom in order to remove it from the lattice site.

D.3 The derivatives of Helmholtz free energy of: gas of the i^{th} bubble, metal deformation caused by the bubble, surface of the i^{th} bubble cap, H_2 molecules, and H atoms located outside the bubbles.

The equilibrium condition of the process of the i^{th} bubble growth is:

$$\frac{\partial F_{\text{config,i}}}{\partial N_{H_2,i,j}} = 0, \tag{D.7}$$

The assumption is fulfilled when the time scale of a bubble growth is longer than the time scale of the formation of a H_2 molecule out of two H atoms and the thermodynamic equilibrium is rapidly re-established after merging a H_2 molecule to a given bubble during a given time step. Since the free energy of the system is given by the Eq. 4.16, condition D.7 can be written as a sum:

$$\frac{\partial F_{\mathrm{gas,i}}}{\partial N_{\mathrm{H_2,i,j}}} + \frac{\partial F_{\mathrm{md,i}}}{\partial N_{\mathrm{H_2,i,j}}} + \frac{\partial F_{\mathrm{surf,i}}}{\partial N_{\mathrm{H_2,i,j}}} + \frac{\partial F_{\mathrm{H_2}}}{\partial N_{\mathrm{H_2,i,j}}} + \frac{\partial F_{\mathrm{H}}}{\partial N_{\mathrm{H_2,i,j}}} = 0. \tag{D.8}$$

Derivatives of the free energy of the gas in the i$^{\mathrm{th}}$ bubble, of metal deformation caused by the bubble, surface of the i$^{\mathrm{th}}$ bubble cap, and of H and H_2 molecules located on the lattice sites with respect to the number of H_2 molecules that merge on each time step to a bubble, will be calculated separately. By use of the Helmholtz free energy of the gas, Eq. 4.17, the derivative is:

$$\left.\frac{\partial F_{\mathrm{gas,i}}}{\partial N_{\mathrm{H_2,i,j}}}\right|_{\mathrm{N}} = -Nk_{\mathrm{B}}T\ln\left(\frac{V_{\mathrm{max,i}}}{V_{\mathrm{min}}}\right) - \frac{3}{2}Nk_{\mathrm{B}}T. \tag{D.9}$$

The free energy of a metal deformation caused by expanding i$^{\mathrm{th}}$ bubble is given by the Eq. 4.19, hence its derivative is:

$$\left.\frac{\partial F_{\mathrm{md,i}}}{\partial N_{\mathrm{H_2,i,j}}}\right|_{\mathrm{N}} = \frac{3}{\pi}\frac{1+\gamma_{\mathrm{p}}}{E_{\mathrm{Y}}}k_{\mathrm{B}}^2T^2\sum_{\mathrm{j}}^{\mathrm{N}}N_{\mathrm{H_2,i,j}}\left[2r_{\mathrm{i}}^{-3}N - 3r_{\mathrm{i}}^{-4}\frac{\partial r_{\mathrm{i}}}{\partial N_{\mathrm{H_2,i,j}}}\sum_{\mathrm{j}}^{\mathrm{N}}N_{\mathrm{H_2,i,j}}\right]. \tag{D.10}$$

The free energy of a surface of the i$^{\mathrm{th}}$ bubble cap is given by the Eq. 4.20. The corresponding derivative is given by:

$$\left.\frac{\partial F_{\mathrm{surf,i}}}{\partial N_{\mathrm{H_2,i,j}}}\right|_{\mathrm{N}} = 8\pi r_{\mathrm{i}}\frac{\partial r_{\mathrm{i}}}{\partial N_{\mathrm{H_2,i,j}}}\sigma_{\mathrm{S}}(T). \tag{D.11}$$

The derivative of the Helmholtz free energy of the H_2 molecules (Eq. D.4) located outside the bubbles at certain positions in the metal lattice is:

$$\begin{aligned}
\left.\frac{\partial F_{\mathrm{H_2}}}{\partial N_{\mathrm{H_2,i,j}}}\right|_{\mathrm{N}} &= -\epsilon_{\mathrm{H_2}}NN_{\mathrm{B}}^{\mathrm{T}} - NN_{\mathrm{B}}^{\mathrm{T}}k_{\mathrm{B}}T\ln\left(\frac{N_{\mathrm{H_2}}^{\mathrm{T}} - \sum_{\mathrm{i}}^{\mathrm{N_B^T}}\sum_{\mathrm{j}}^{\mathrm{N}}N_{\mathrm{H_2,i,j}}}{N_0}\right) \\
&- k_{\mathrm{B}}T\left(N_{\mathrm{H_2}}^{\mathrm{T}} - \sum_{\mathrm{i}}^{\mathrm{N_B^T}}\sum_{\mathrm{j}}^{\mathrm{N}}N_{\mathrm{H_2,i,j}}\right)\frac{N_0}{N_{\mathrm{H_2}}^{\mathrm{T}} - \sum_{\mathrm{i}}^{\mathrm{N_B^T}}\sum_{\mathrm{j}}^{\mathrm{N}}N_{\mathrm{H_2,i,j}}}\frac{NN_{\mathrm{B}}^{\mathrm{T}}}{N_0} \\
&= -NN_{\mathrm{B}}^{\mathrm{T}}\left\{\epsilon_{\mathrm{H_2}} + k_{\mathrm{B}}T\left[1 + \ln\left(\frac{N_{\mathrm{H_2}}^{\mathrm{T}} - \sum_{\mathrm{i}}^{\mathrm{N_B^T}}\sum_{\mathrm{j}}^{\mathrm{N}}N_{\mathrm{H_2,i,j}}}{N_0}\right)\right]\right\}.
\end{aligned} \tag{D.12}$$

The derivative of the Helmholtz free energy of the H atoms (Eqs. D.5 and D.6) located at certain positions in the metal lattice is (the procedure is the same as with Eq. D.12):

$$\left.\frac{\partial F_{\mathrm{H}}}{\partial N_{\mathrm{H_2,i,j}}}\right|_{\mathrm{N}} = -2NN_{\mathrm{B}}^{\mathrm{T}}\left[\epsilon_{\mathrm{H}} + k_{\mathrm{B}}T\left(1 + \ln\frac{N_{\mathrm{H}}^{\mathrm{T}} - 2N_{\mathrm{H_2}}^{\mathrm{T}}}{N_0}\right)\right]. \tag{D.13}$$

Acknowledgments

This thesis could no have been written without Professor Ulrich Geppert, who is my research mentor. He is always there, serving advices, and long discussions.

Table of Symbols

Symbol	Description
a	constant parameter
A	scattering amplitude
A_s	area of a sample
α_c	fine structure constant
α_m	constant parameter
α_s	solar absorption coefficient
BS	backscattering coefficient
c	speed of light
C	constant parameter
C_0	wavenumber
d_PR	projected range
δ	scattering angle
$\delta(x)$	Dirac delta
E	total energy
E'	energy of an electron in the conduction band
E''	energy of an Auger electron in the conduction band
E_Bohr	Bohr energy
E_F	Fermi energy
E_h	Hartree energy
E_ion	total energy of an incident ion
E_K	kinetic energy
E_K^e	kinetic energy of an Auger electron
$E_\mathrm{pot}^\mathrm{ion}$	potential energy of an incident ion
$\mathbf{E}^\mathrm{ind}$	induced electric field
E_Y	Young module
ϵ	permittivity
ϵ_0	vacuum permittivity
ϵ_H	migration energy of H atom in the metal lattice
ϵ_{H_2}	binding energy of H_2 molecule to a vacancy
ϵ_m	constant parameter
ϵ_t	thermal emission coefficient
η	relation between the number of H_2 molecules and H atoms in the sample
$f_\mathrm{lab}^{\mathrm{p}^+}$	flux of protons used in the experiment
$f_\mathrm{S}^{\mathrm{p}^+}$	flux of solar protons
F_C	Coulomb force
F_config	Helmholtz free energy of a sample covered by bubbles
$F_\mathrm{gas,i}$	Helmholtz free energy of gas filled i^th bubble
F_H	Helmholtz free energy of H atoms placed outside the bubbles within the metal lattice
F_{H_2}	Helmholtz free energy of H_2 molecules placed outside the bubbles within the metal lattice

$F_{\mathrm{md,i}}$	Helmholtz free energy of metal deformation caused by the i$^{\mathrm{th}}$ molecular Hydrogen bubble
$F_{\mathrm{surf,i}}$	Helmholtz free energy of a surface of the i$^{\mathrm{th}}$ molecular Hydrogen bubble
$F(x, E, \kappa)$	amount of energy per unit length
$\mathbf{G}$	reciprocal vector of the lattice
γ	Lorentz factor
γ_{p}	Poisson coefficient
$\Gamma^{\mathrm{C,L}}$	probability per unit time of electron capture (C) or loss (L)
H	Hamiltonian
H_0	Hamiltonian of an electron gas
H_{i}	partial derivative sum
H_{I}	Hamiltonian of ion - active electron composite
$\hbar$	Planck constant
$\|i\rangle$	eigenfunction
I	flux of particles
I_{p}	ionization potential
I_{K}	experimental ionization potential of K shell
$I_{\mathrm{particles}}$	intensity of particles
$\bar{I}_{\mathrm{p}}$	mean ionization potential
k_{B}	Boltzmann constant
κ	direction cosine
$\|\mathbf{k}_{\mathrm{OPW}}\rangle$	Orthogonal Plane Wave
$\mathbf{k}_0$	total momentum of ion - active electron composite
l	orbital quantum number
$\bar{l}$	mean free path
L	angular momentum
L_{s}	thickness of a solar sail foil
L_{n+1}^{2l+1}	Laguerre polynomial
m	mass of an incident particle
M	mass of metallic foil ion
M_{u}	molar mass of an element
m_{e}	mass of an electron
m_{p}	mass of a proton
μ	attenuation coefficient
n	number of shell in atom
n_0	number density of lattice ions
n_{e}	number density of incident electrons
n_{i}	integer number
N	number of iterations
$N_{\mathrm{particles}}$	number of incident particles
N_0	number of lattice sites
N_{A}	Avogadro constant
N_{B}	number of molecular Hydrogen bubbles per unit area
$N_{\mathrm{B}}^{\mathrm{T}}$	total number of molecular Hydrogen bubbles on irradiated sample
N_{cells}	number of cells
N_{D}	number of dislocations in the metal lattice
$N_{\mathrm{H_2,i,j}}$	number of H_2 molecules merged to the i$^{\mathrm{th}}$ bubble
$N_{\mathrm{H_2}}^{\mathrm{T}}$	total number of H_2 molecules in the sample
$N_{\mathrm{H,j}}$	number of recombined H atoms in the j$^{\mathrm{th}}$ time step
$N_{\mathrm{diff,j}}$	number of H atoms which diffuse from the sample out in the j$^{\mathrm{th}}$ time step

Ω	number of ways in which H_2 molecules can be arranged on lattice sites
p	constant parameter
p_{i}	pressure inside the i^{th} bubble
P	probability
Π	probability amplitude
$\psi(r,\theta,\phi)$	state function of Hydrogen atom
$\psi_{\mathrm{i,f}}$	wave function
$\phi(\mathbf{q},\omega)$	scalar potential
$\phi_{\mathrm{i,f}}$	wave function
q	momentum
Δq	momentum transfer
Q_{s}	total surface charge
r, R	distance
r_0	Bohr radius
$r_{\mathrm{e}}(n)$	radius of an electron on the n^{th} shell in an atom
r_{i}	radius of the i^{th} bubble
$dr_{\mathrm{i,j}}$	differential increase of the i^{th} bubble radius after the j^{th} time step
$r_{\mathrm{max,i}}$	maximum radius of the i^{th} bubble
R_{cell}	reflectivity of a single cell
R_{foil}	reflectivity of a foil
$R_{n,l}(r)$	radial part of state function of Hydrogen atom
ρ	density of material
$\boldsymbol{\rho}$	distance between ion - active electron
ϱ	resistivity
$\varrho_{\text{crystal imperfections}}$	contribution to resistivity from crystal imperfections
ϱ_{D}	contribution to resistivity from dislocations in metal lattice
$\varrho_{\text{impurities}}$	contribution to resistivity from impurities from dislocations in metal lattice
$\varrho_{\mathrm{c}}(\mathbf{r},t)$	charge density
S	entropy
SY	Sputtering Yield
σ	conductivity
σ_{S}	surface tension of a bubble
$d\Sigma$	differential cross section
Σ_{A}	cross section for Auger recombination process
Σ_{OBK}	cross section for OBK recombination process
Σ_{R}	cross section for resonant recombination process
Σ_{RR}	cross section of radiative recombination process
Σ_{total}	total cross section
t	time
Δt_{j}	time step
T	temperature
Θ	Debye temperature
$\Theta(x)$	step function
$\mathbf{u}_0$	plane wave
U_0	surface binding energy
v	velocity of incident particle
v_{e}	velocity of incident electrons
$v_{\mathrm{e}}(n)$	velocity of electron on the n^{th} shell in an atom

v_{F}	velocity of a reference frame
$V(\mathbf{G})$	Hartree potential
$V(r)$	potential energy
V_{i}	volume of the i$^{\mathrm{th}}$ bubble
$V_{max,i}$	maximum volume of the i$^{\mathrm{th}}$ molecular Hydrogen bubble
V_{min}	minimum volume of molecular Hydrogen bubble
V_{S}	effective potential
ν	frequency of the electromagnetic radiation
W	work function
$d\Omega$	solid angle
ω	binding energy
ω_0	angular velocity of an electron in an ion
x_{imp}	mole fraction of impurities
dx	penetration length
ξ	impact parameter
$\xi_{\mathrm{H_2}}$	relation between the number of H_2 molecules inside and outside the molecular Hydrogen bubble
ξ_{max}	maximum value of the impact parameter
ξ_{min}	minimum value of the impact parameter
$Y_{l,m}(\theta,\phi)$	spherical harmonics
ze, Ze	charge

Table of Physical Constants

Table D.1: Physical constants

Physical constant	value	description
c	2.997925×10^{8} ms^{-1}	speed of light
$\hbar$	1.054×10^{-34} Js	Planck constant
e	1.6022×10^{-19} C	elementary charge
m_{e}	9.109×10^{-31} kg	electron mass
m_{p}	1.6726×10^{-27} kg	proton mass
ϵ_0	8.8542×10^{-12} C^{2}m^{-2}N^{-1}	permittivity of free space
N_{A}	6.02214×10^{23} mol^{-1}	Avogadro constant

Table D.2: Young and Poisson values for common materials.

Material	Young modulus $\times 10^9$ [Nm^{-2}]	Poisson coefficient
Aluminum	69	0.33
Copper	117.0	0.36
Platinum	146.86	0.39
Polyimide	2.5	-
Titanium	110.32	0.30

List of Figures

List of Tables

Bibliography

[1] "Astm e512-94, standars particle for combined, simulated space environment testing of thermal control materials with electromagnetic and particulate radiation," 2010.

[2] ECSS-Q-ST-70-06C, "Ecss-q-st-70-06c, particle and uv radiation testing for space materials," 2008.

[3] D. Agnolan, "Study overview of solar sail demonstrator: Geosail," vol. 1 of *SCI-PA*, pp. 1–54, 2007.

[4] S. Heltzel, C. Semprimoschnig, and M. V. Eesbeek, "Environmental testing of thermal control materials at elevated temperature and intense ultraviolet radiation," *Journal of Spacecraft and Rockets*, vol. 46, pp. 248–254, 2009.

[5] F. Lura, T. Verhovtsva, V. I. Yaremennko, *et al.*, "Gas-jet simulator of solar vuv and soft x-ray radiation and irradiation effect on some materials," Proceedings of the 7$^{\text{th}}$ International Symposium on Materials in Space Environment, Toulouse, France, 1997.

[6] A. K. Sharma and N. Sridhara, "Degradation of thermal control materials under a simulated radiative space environment," *Advances in Space Research*, vol. 50, pp. 1411–1424, 2012.

[7] B. Dachwald, V. Baturkin, V. Coverstone, *et al.*, "potential effects of optical solar sail degradation on interplanetary trajectory design," pp. 2569–2592, 2006.

[8] ECSS-Q-ST-70-09C, "Ecss-q-st-70-09c, mesurements of thermo-optical properties of thermal control materials," 2008.

[9] M. Macdonald and C. McInnes, "Solar sail science mission applications and advancement," *Advances in Space Research*, vol. 48, pp. 1702–1716, 2011.

[10] R. L. Garwin *Jet Propulsion*, vol. 28, pp. 188–190, 1958.

[11] U. Geppert, B. Biering, F. Lura, *et al.*, "The 3-step dlr-esa gossamer road to solar sailing," *Advances in Space Research*, vol. 48, pp. 1695–1701, 2011.

[12] R. Kezerashvili and G. L. Matloff, "Microscopic approach to analyze solar-sail space-environment effects," *Advances in Space Research*, vol. 44, pp. 859–869, 2009.

[13] T. Renger, M. Sznajder, A. Witzke, and U. Geppert, "The complex irradiation facility at dlr-bremen," *Journal of Materials Science and Engineering A*, vol. 4, p. 1, 2014.

[14] Y. Ralchenko, A. E. Kramida, J. Reader, and N. A. T. (2011), 2012. NIST Atomic Spectra Database (v. 4.1.9), [Online]. Available: http://physics.nist.gov/asd [2012, May 29]. National Institute of Standards and Technology, Gaithersburg, MD.

[15] W. Curdt, E. Landi, and U. Feldman, "The sumer spectral atlas of solar coronal features," *Astronomy and Astrophysics*, vol. 427, pp. 1045–1054, 2004.

[16] M. Sznajder, T. Renger, A. Witzke, U. Geppert, and R. Thornagel, "Design and performance of a vacuum-uv simulator for material testing under space conditions," *Advances in Space Research*, vol. 52, pp. 1993–2005, 2013.

[17] M. Sznajder, U. Geppert, and M. Dudek, "Degradation of metallic surfaces under space conditions, with particular emphasis on hydrogen recombination processes," *Advances in Space Research*, vol. 56, pp. 71–84, 2015.

[18] M. S. Longair, *High Energy Astrophysics Vol 1: Particles, Photons and their Detection*. Cambridge University Press, 1992.

[19] J. Araminowicz, K. Maluszynska, and M. Przytula, *Laboratorium Fizyki Jadrowej*. Państwowe Wydawnictwo Naukowe, PWN, 1978.

[20] G. E. Pustowalow, *Fizyka Atomowa i Jadrowa*. Panstwowe Wydawnictwo Naukowe, 1972.

[21] A. Das and A. C. Melissions, *Quantum Mechanics: A Modern Introduction*. Gordon and Breach Science Publisher, 1990.

[22] R. Kezerashvili and G. L. Matloff, "Solar radiation and the beryllium hollow-body sail: 2. diffusion, recombination and erosion processes," *Journal of British Interplanetary Society*, vol. 61, pp. 169–179, 2008.

[23] K. R. Lang, *Astronomical Formulae: A Compedium for the Physicist and Astrophysicist*. Spinger-Verlag, 1980.

[24] E. B. Podgorsak, *Radiation Physics for Medical Physicists*. Springer - Verlag, 2010.

[25] M. J. Berger, J. S. Coursey, M. A. Zucker, and J. Chan, "Stopping-power and range tables for electrons, protons, and helium ions," 2005. NIST, Physical Measurment Laboratory.

[26] J. F. Ziegler, "Stopping of energetic light ions in elemental matter," *Journal of Applied Physics*, vol. 85, pp. 1249–1273, 1999.

[27] R. Zimny, Z. L. Miskovic, N. N. Nedeljkovic, *et al.*, "Interplay of resonant and auger processes in proton neutralization after grazing surface scattering," *Surface Science*, vol. 255, pp. 135–156, 1991.

[28] H. D. Hagstrum, "Theory of auger ejection of electrons from metals by ions," *Physical Review*, vol. 96, pp. 336–365, 1954.

[29] E. Taute, "Auger neutralization of fast ions at surfaces," *Physica Status Solidi (b)*, vol. 142, pp. 437–443, 1987.

[30] F. Sols and F. Flores, "Charge transfer processes for light ions moving in metals," *Physical Review B*, vol. 30, pp. 4878–4880, 1984.

[31] G. Raisbeck and F. Yiou, "Electron capture by 40-, 155-, and 600-mev protons in thin foils of mylar, al, ni, and ta," *Physical Review A*, vol. 4, pp. 1858–1868, 1971.

[32] M. Penalba, A. Arnau, and P. M. Echenique, "Target dependence of electron-capture and -loss cross sections of protons in solids," *Nuclear Instruments and Methods in Physics Research B: Beam Interactions with Materials and Atoms*, vol. 48, pp. 138–141, 1990.

[33] L. I. Schiff, *Quantum Mechanics*. McGraw-Hill Book Company, Inc., 1955.

[34] S. Szpikowski, *Podstawy Mechaniki Kwantowej*. Wydawnictwo Universytetu Marii Curie - Sklodowskiej, 2006.

[35] L. D. Landau and J. M. Lifshitz, *Quantum Mechanics, Non-Relativistic Theory*. PWN, 2003.

[36] R. Grigorovici, A. Devenyi, and T. Botila, "The number of free electrons in aluminium," *Journal of Physics and Chemistry of Solids*, vol. 23, pp. 428–429, 1962.

[37] J. M. Ziman, *Electrons and Phonons*. Oxford at the Clarendon Press, 1960.

[38] A. Bid, A. Bora, and A. K. Raychaudhuri, "Temperature dependance of the resistance of metallic nanowires of diameter ge 15 nm: Applicability of bloch-grueneisen theorem," *Physical Review B*, vol. 74, pp. 035426–035434, 1964.

[39] P. M. Echenique and F. Flores, "Inelastic proton-solid collisions," *Physical Review B*, vol. 35, pp. 8249–8251, 1987.

[40] F. Guinea, F. Flores, and P. M. Echenique, "Charge states for h and he moving in an electron gas," *Physical Review B*, vol. 25, pp. 6109–6125, 1982.

[41] N. Pauly, A. Dubus, and M. Roesler, "Electron capture and loss processes for protons in aluminium: Comparison between conduction band electron–hole assisted and plasmon assisted auger processes," *Nuclear Instruments and Methods in Physics Research B: Beam Interactions with Materials and Atoms*, vol. 193, pp. 414–418, 2002.

[42] M. Roesler and F. J. G. de Abejo, "Contribution of charge-transfer processes to ion-induced electron emission," *Physical Review B*, vol. 54, pp. 17158–17165, 1996.

[43] F. Sols and F. Flores, "Inelastic cross sections and charge states for b, c, n, and o ions moving in metals," *Physical Review A*, vol. 37, pp. 1469–1475, 1988.

[44] P. M. Echenique, F. Flores, and R. H. Ritchie, "Dynamic screening of ions in condensed matter," *Solid State Physics*, vol. 43, pp. 229–308, 1990.

[45] J. D. Jackson, *Classical Electrodynamics*. John Wiley & Sons, Inc., 1999.

[46] H. Bruus and K. Flensberg, *Many-Body Quantum Theory in Condensed Matter Physics: An Introduction*. Oxford University Press, 2013.

[47] G. S. University, 2014. The HyperPhysics, http://hyperphysics.phy.gsu.edu/hbase/quantum/fermi.html.

[48] I. V. Abarenkov, "On the orthogonalized plane wave method," *Physica Status Solidi B*, vol. 50, pp. 465–470, 1972.

[49] J. Callaway, "Orthogonalized plane wave method," *Physical Review*, vol. 97, pp. 933–936, 1955.

[50] C. Herring, "A new method for calculating wave functions in crystals," *Physical Review*, vol. 57, pp. 1169–1177, 1940.

[51] E. Wigner and F. Seitz, "On the constitution of metallic sodium," *Physical Review*, vol. 43, pp. 804–810, 1933.

[52] P. M. Chaikin and T. C. Lubensky, *Principles of Condensed Matter Physics*. Cambridge University Press, 2000.

[53] S. Alston, "Theory of electron capture from a hydrogenlike ion by a bare ion: Intermediate-state contributions to the amplitude," *Physical Review A*, vol. 27, pp. 2342–2357, 1983.

[54] D. Belkic, R. Gayet, and A. Salin *Physics Reports*, vol. 56, pp. 279–369, 1979.

[55] B. H. Bransden and I. M. Cheshire, eds., *Electron Capture from Helium by Fast Protons*, vol. 81 of *Proceedings of the Physical Society*, 1963.

[56] G. F. Chew, "The inelastic scattering of high energy neutrons by deuterons according to the impulse approximation," *Physical Review*, vol. 80, pp. 196–202, 1950.

[57] S. K. Datta, D. S. F. Crothers, and R. McCarroll, "The relation between the coulomb-born and the boundary-corrected first-order born approximations for electron capture," *Journal of Physics B: Atomic, Molecular and Optical Physics*, vol. 23, pp. 479–495, 1990.

[58] F. Decker and J. Eichler, "Consistent treatment of electron screening in charge transfer," *Physical Review A*, vol. 39, pp. 1530–1533, 1989.

[59] A. L. Ford, J. F. Reading, and R. L. Becker, "Inner-shell capture and ionization in collisions of h+, he2+, and li3+ projectiles with neon and carbon," *Physical Review A*, vol. 23, pp. 510–518, 1981.

[60] M. Ghosh, C. R. Mandal, and S. C. Mukherjee, "Charge-transfer cross sections for asymmetric collisions of protons with carbon, nitrogen, oxygen, neon, and argon," *Physical Review A*, vol. 35, pp. 2815–2820, 1987.

[61] M. S. Gravielle and J. E. Miraglia, "Electron capture in asymmetric collisions," *Physical review A*, vol. 38, pp. 5034–5037, 1988.

[62] G. Lapicki and W. Losonsky, "Electron capture from inner shells by fully stripped ions," *Physical Review A*, vol. 15, pp. 896–905, 1977.

[63] C. D. Lin, S. C. Soong, and L. N. Tunnell, "Two-state atomic expansion methods for electron capture from multielectron atoms by fast protons," *Physical review A*, vol. 17, p. 1646, 1978.

[64] J. E. Miraglia, "Electron capture in asymmetric collisions," *Physical Review A*, vol. 30, pp. 1721–1726, 1984.

[65] Y. R. Kuang, "Model-potential oppenheimer-brinkman-kramers approximation for k-shell electron capture in asymmetric collisions," *Physical Review A*, vol. 44, pp. 1613–1619, 1991.

[66] Y. R. Kuang, "Electron capture in collisions between protons and the ions he+ and li+,2+ calculated using a new united-atom model," *Journal of Physics B: Atomic, Molecular and Optical Physics*, vol. 24, pp. 1645–1655, 1991.

[67] K. E. Banyard and B. J. Szuster, "Continuum-distorted-wave calculations for rearrangement cross sections and their sensitivity to improvements in the target wave function: Proton-helium collisions," *Physical Review A*, vol. 16, pp. 129–132, 1977.

[68] T. G. Winter and C. C. Lin, "Electron capture by protons in helium and hydrogen atoms at intermediate energies," *Physical Review A*, vol. 10, pp. 2141–2155, 1974.

[69] J. C. Slater, "One-electron energies of atoms, molecules, and solids," *Physical Review*, vol. 98, pp. 1039–1045, 1955.

[70] J. C. Slater, *Quantum theory of atomic structure*. McGraw-Hill, 1960.

[71] B. Dachwald, M. Macdonald, C. R. McInnes, *et al.*, "Impact of optical degradation on solar sail mission performance," *Journal of Spacecraft and Rockets*, vol. 44, pp. 740–749, 2007.

[72] ASTM-E490, "Standard solar constant and zero air mass solar spectral irradiance tables," 2014.

[73] C. A. Gueymard, "The sun's total and spectral irradiance for solar energy applications and solar radiation models," *Solar Energy*, vol. 76, pp. 423–453, 2004.

[74] N. Melnik, U. Geppert, B. Biering, *et al.*, "Light pressure measurement at dlr-bremen," Advances in Solar Sailing, Springer Praxis Books, 2014.

[75] J. Marco and S. Remaury, "Evaluation of thermal control coatings degradation in simulated geo-space environment," *High Performance Polymers*, vol. 16, pp. 177–196, 2004.

[76] A. Polsak, M. Eesbeek, and C. O. A. Semprimoschnig, "In-situ testing at estes's sorasi facility," in *Proceedings of Proceedings of the 9th International Symposium on Materials in a Space Environment*, 2003.

[77] E. T. Verkhovtseva, V. I. Yaremenko, Telepnev, *et al.*, "Gas-jet simulator of solar vuv and soft x-ray radiation and irradiation effect on some material," in *Proceedings of the 7th International Symposium on Materials in Space Environment*, 1997.

[78] M. Richter, J. Hollandt, U. Kroth, *et al.*, "The two normal-incidence monochromator beam lines of ptb at bessy ii," *Nuclear Instruments and Methods in Physics Research A*, vol. 467-468, pp. 605–608, 2001.

[79] M. Richter and G. Ulm, "Radiometry using synchrotron radiation at ptb," *Journal of Electron Spectroscopy and Related Phenomenena*, vol. 101-103, pp. 1013–1018, 1999.

[80] P. A. Redhead, "Hydrogen in vacuum systems: An overview," in *Hydrogen in Materials & Vacuum Systems*, p. 243, 2002.

[81] A. Gottwald, R. Klein, R. Mueller, *et al.*, "Current capabilities at the metrology light source," *Metrologia*, vol. 49, pp. 146–151, 2012.

[82] R. Behrish *Ergebn. Exakt. Naturw.*, vol. 35, p. 295, 1964.

[83] G. Carter, J. S. Colligon, and M. J. Nobes, "The equilibrium topography of sputtered amorphous solids ii," *Journal of Material Science*, vol. 6, pp. 115–117, 1971.

[84] M. Kaminsky and S. K. Das, "Effect of channeling and irradiation temperature on the morphology of blisters in niobium," *Applied Physics Letters*, vol. 21, pp. 443–445, 1972.

[85] R. J. MacDonald, "The ejection of atomic particles from ion bombarded solids," *Advances in Physics*, vol. 19, pp. 457–524, 1970.

[86] G. M. McCracken, "The behaviour of surfaces under ion bombardment," *Reports on Progress in Physics*, vol. 38, pp. 241–327, 1975.

[87] P. Sigmund, "Theory of sputtering. i. sputtering yield of amorphous and polycrystalline targets," *Physical Review*, vol. 184, pp. 383–416, 1969.

[88] H. E. Farnworth, R. E. Schlier, T. H. George, *et al.*, "Application of the ion bombardment cleaning method to titanium, germanium, silicon, and nickel as determined by low energy electron diffraction," *Journal of Applied Physics*, vol. 29, pp. 1150–1162, 1985.

[89] H. J. Liebl and R. F. K. Herzog, "Sputtering ion source for solids," *Journal of Applied Physics*, vol. 34, pp. 2893–2897, 1963.

[90] R. Castaing and G. Slodzian, "Micro-analyse per emission ionique secondaire," *Comptes Rendus de l'Academie des Sciences*, vol. 255, pp. 1893–1897, 1962.

[91] M. K. Abdullayeva, A. K. Ayukhanov, and U. B. Shamsiyev, "Determination of the negative ion yield of cooper sputtered by cesium ions," *Radiation Effects and Defects in Solids*, vol. 19, pp. 225–229, 1973.

[92] B. K. Winterbon, P. Sigmund, J. B. Sanders, *et al. Math. -Fys. Meddr*, vol. 37, 1970.

[93] S. Linderoth *Philosophical Magazine Letters*, vol. 57, p. 229, 1988.

[94] P. Karmakar and D. Ghose, "Ion beam sputtering induced ripple formation in thin metal films," *Surface Science*, vol. 554, pp. L101–L106, 2004.

[95] J. F. Ziegler, 2013. SRIM Software, www.srim.org.

[96] B. A. Banks, "Atomic oxygen effects on spacecraft materials," *NASA/TM-2003-212484*, 2003.

[97] L. H. Milacek, R. D. Daniels, and J. A. Cooley, "Proton radiation induced blistering of aluminum," *Journal of Applied Physics*, vol. 39, pp. 2803–2816, 1968.

[98] O. Montenbruck and E. Gil, *Satellite Orbits: Models, Methods, Applications*. Springer-Verlag, 2005.

[99] A. Rooij, *Corrosion in Space - Encyclopedia of Aerospace Engineering*. John Wiley & Sons Ltd., 2010.

[100] G. Bitetti, M. Marchetti, S. Mileti, *et al.*, "Degradation of the surfaces exposed to the space environment," *Acta Astronautica*, vol. 60, pp. 166–174, 2007.

[101] E. Grossman, Y. Lifshitz, J. T. Wolan, *et al.*, "In situ erosion study of kapton-laquo; using novel hyperthermal oxygen atom source," *Journal of Spacecraft and Rockets*, vol. 36, pp. 75–78, 1999.

[102] X. H. Zhao, Z. G. Shen, Y. S. Xing, *et al.*, "A study of the reaction characteristics and mechanism of kapton in a plasma-type ground-based atomic oxygen effects simulation facility," *Journal of Physics D: Applied Physics*, vol. 34, pp. 2308–2315, 2001.

[103] E. Grossman and I. Gouzman, "Space environment effects on pomymers in low earth orbit," *Nuclear Instruments and Methods in Physics Research B*, vol. 208, pp. 48–57, 2003.

[104] T. K. Minton *et al.*, "Protecting polymers in space with atomic layer deposition coatings," *Applied Materials & Interfaces*, vol. 2, p. 2515, 2010.

[105] Y. Gudimenko, R. Ng, J. I. Kleinman, *et al.*, "Enhancement of surface durability of space materials and structures in leo environment," Proceedings of the 9th International Symposium on Materials in a Space Environment, 2003.

[106] B. A. Banks *et al.*, "Atomic oxygen erosion yield prediction for spacecraft polymers in low earth orbit," *NASA/TM-2009-215812*, 2009.

[107] M. Romero and D. Boscher, "Esa space environments and effects analysis section (esa tos-ema)," in *ESA Workshop on Space Weather*, 1998.

[108] J. Marco, S. Remaury, and C. Tonon, "Eight years geo ground testing of thermal control coatings," Proceedings of the 11$^{\text{th}}$ International Symposium on Materials in a Space Environment, 2009.

[109] V. T. Astrelin, A. V. Burdakov, P. V. Bykov, *et al.*, "Blistering of the selected materials irradiated by intense 200 kev proton beam," *Journal of Nuclear Materials*, vol. 396, pp. 43–48, 2010.

[110] G. Lu and E. Kaxiras, "Hydrogen embrittlement of aluminum: the crucial role of vacancies," *Physical Review Letters*, vol. 94, pp. 155501–155505, 2005.

[111] S. M. Myers, M. I. Baskes, H. K. Birnbaum, *et al.*, "Hydrogen interactions with defects in crystalline solids," *Review of Modern Physics*, vol. 64, pp. 559–617, 1992.

[112] R. D. Daniels, "Correlation of hydrogen evolution with surface blistering in proton-irradiated aluminum," *Journal of Applied Physics*, vol. 42, pp. 417–419, 1971.

[113] H. Metzger, J. Peisl, and J. Wanagel, "Huang diffuse scattering of x-rays from the displacement field of hydrogen in niobium," *Journal of Physics F: Metal Physics*, vol. 6, pp. 2195–2207, 1976.

[114] X. Ren, W. Chu, J. Li, *et al.*, "The effects of inclusions and second phase particles on hydrogen-induced blistering in iron," *Materials Chemistry and Physics*, vol. 107, pp. 231–235, 2008.

[115] G. J. Thomas and W. D. Drotning *Metallurgical Transactions A*, vol. 14, pp. 1545–1548, 1983.

[116] A. C. Damask and G. J. Dienes, *Point Defects in Metals.* Gordon and Breach Science Publishers, 1971.

[117] D. Milcius, L. L. Pranevicius, and C. Templier, "Hydrogen storage in the bubbles formed by high-flux ion implantation in thin al films," *Journal of Alloys and Compounds*, vol. 398, pp. 203–207, 2005.

[118] M. N. Polyanskiy, 2014. Refractive index database, http://refractiveindex.info.

[119] K. Kamada, A. Sagara, H. Kinoshita, *et al.*, "Microstructural change of al on h implantation," *Radiation Effects and Defects in Solids*, vol. 103, pp. 119–133, 1986.

[120] P. Rozenek, "Hemispherical bubbles growth on electrochemically charged aluminum with hydrogen," *International Journal of Hydrogen Energy*, vol. 32, pp. 2816–2823, 2007.

[121] N. V. Meyer, *Basics of the Solar Wind*. Cambridge University Press, 2007.

[122] L. T. Canham *et al.*, "Radiative recombination channels due to hydrogen in crystalline silicon," *Materials Science and Engineering: B*, vol. 4, pp. 41–45, 1989.

[123] F. H. Ree and C. F. Bender, "Repulsive intermolecular potential between two h2 molecules," *Journal of Chemical Physics*, vol. 71, pp. 5362–5376, 1979.

[124] B. Lautrup, *Electron capture from inner shells by fully stripped ions*. Taylor & Francis Group, 2011.

[125] L. D. Landau and J. M. Lifshitz, *Theory of Elasticity*. Pergamon Press, 1986.

[126] Y. V. Martynenko, "The theory of blister formation," *Radiation Effects and Defects in Solids*, vol. 45, pp. 93–101, 1979.

[127] G. Szenes, "Comparison of two thermal spike models for ion–solid interaction," *Nuclear Instruments and Methods in Physics Research B*, vol. 269, pp. 174–179, 2011.

[128] C. C. Smith, "Solutions of the radiation diffusion equation," *High Energy Density Physics*, vol. 6, pp. 48–56, 2010.

[129] R. Li, C. Li, S. He, *et al.*, "Radiation effect of kev protons on optical properties of aluminized kapton film," *Radiation Physics and Chemistry*, vol. 76, pp. 1200–1204, 2007.

[130] R. Li, C. Li, S. He, *et al.*, "Damage effect of kev proton irradiation on aluminized kapton film," *Radiation Physics and Chemistry*, vol. 77, pp. 482–489, 2008.

[131] A. Balakrishnan, V. Smith, and B. P. Stoicheff, "Dissociation energy of the hydrogen molecule," *Physical Review Letters*, vol. 68, pp. 2149–2152, 1992.

[132] B. Mason, "Quantum physics - lectures," 2013. Homer L. Dodge Department of Physics and Astronomy.